University of Turin

Master Thesis

Nuclear and Subnuclear Physics

Search for $h_b(2P) \to \chi_{bJ}(1P)\gamma$ at Belle

Author:
A. Boschetti

Supervisors:
Prof. S. Spataro
Dr. U. Tamponi

Contents

List of Figures

List of Tables

Abstract

This thesis reports the search for the hindered magnetic dipole (M1) transitions between the spin-singlet state $h_b(2P)$ and the spin-triplet states $\chi_{bJ}(1P)$. The data collected by the Belle experiment in e^+e^- collisions at the center of mass energy $\sqrt{s} = 10.860\ GeV$ has been exploited, with $\mathcal{L} = 121.4\ fb^{-1}$ integrated luminosity. The reconstructed decay chain is fully exclusive, and corresponds to the cascade $\Upsilon(10860) \rightarrow h_b(2P)\pi^+\pi^- \rightarrow \gamma\chi_{bJ}(1P)\pi^+\pi^- \rightarrow \gamma\gamma\Upsilon(1S)\pi^+\pi^- \rightarrow \gamma\gamma\mu^+\mu^-\pi^+\pi^-$. The selection procedure has been optimized on Monte Carlo (MC) simulations and validated on experimental data collected at the $\Upsilon(3S)$ resonance, by studying the control channel $\Upsilon(3S) \rightarrow \gamma\chi_{bJ}(2P) \rightarrow \gamma\gamma\Upsilon(2S) \rightarrow \gamma\gamma\pi^+\pi^-\Upsilon(1S) \rightarrow \gamma\gamma\pi^+\pi^-\mu^+\mu^-$. After counting on MC the mean number of background events surviving the selection, the upper limits for the branching fractions $\mathcal{B}[h_b(2P) \rightarrow \gamma\chi_{bJ}(1P)]$, $J = 0, 1, 2$, have been estimated thanks to the Feldman-Cousins statistical method.

The first chapter recalls the highlights of the phenomenological and theoretical description of $b\bar{b}$ states, as well as the recent experimental results that are most relevant to the subject, and gives the definition of the hindered M1 transitions. Chapter 2 gives an overview of the KEKB collider and the Belle detector, whose operations were fundamental for the collection of the data analyzed for the thesis. Chapter 3 provides a description of the software used for the Monte Carlo simulations, the event reconstruction and the data analysis. Chapter 4 develops the whole analysis and reports the final results. The latter include the identification of the main background processes, the estimation of the selection efficiency and of systematic uncertainties, and the expected upper limits for the branching fractions of the transitions under study, expressed as the experimental sensitivity. Finally, chapter 5 reports the concluding considerations concerning the work which was done.

Abstract

In questa tesi è riportata la ricerca delle transizioni "hindered" di dipolo magnetico (M1) tra il singoletto di spin $h_b(2P)$ e il tripletto $\chi_{bJ}(1P)$. Sono stati sfruttati i dati raccolti dall'esperimento Belle in collisioni e^+e^-, con luminosità integrata $\mathcal{L} = 121.4\, fb^{-1}$, all'energia nel centro di massa $\sqrt{s} = 10.860\, GeV$. La catena di decadimento ricostruita è completamente esclusiva, e corrisponde al decadimento a cascata $\Upsilon(10860) \rightarrow h_b(2P)\pi^+\pi^- \rightarrow \gamma\chi_{bJ}(1P)\pi^+\pi^- \rightarrow \gamma\gamma\Upsilon(1S)\pi^+\pi^- \rightarrow \gamma\gamma\mu^+\mu^-\pi^+\pi^-$. La procedura di selezione è stata ottimizzata su simulazioni Monte Carlo (MC) e validata su dati sperimentali raccolti alla risonanza $\Upsilon(3S)$, attraverso lo studio del canale di controllo $\Upsilon(3S) \rightarrow \gamma\chi_{bJ}(2P) \rightarrow \gamma\gamma\Upsilon(2S) \rightarrow \gamma\gamma\pi^+\pi^-\Upsilon(1S) \rightarrow \gamma\gamma\pi^+\pi^-\mu^+\mu^-$. In seguito al conteggio, su simulazioni MC, del numero medio di eventi di fondo che passano la selezione, sono stati stimati i rapporti di decadimento $\mathcal{B}[h_b(2P) \rightarrow \gamma\chi_{bJ}(1P)]$, $J = 0, 1, 2$ usando il metodo statistico proposto da Feldman e Cousins.

Il primo capitolo richiama la descrizione fenomenologica e teorica degli stati $b\bar{b}$ e i risultati sperimentali più rilevanti per il soggetto, e definisce le transizioni M1 hindered. Il capitolo 2 dà una panoramica del collisore KEKB e del rivelatore Belle, il cui funzionamento è stato fondamentale per la raccolta dei dati che sono analizzati nella tesi. Il capitolo 3 descrive i software utilizzati per le simulazioni Monte Carlo, per la ricostruzione degli eventi e per l'analisi dati. Il capitolo 4 sviluppa l'analisi e riporta i risultati finali. Questi includono l'identificazione dei più importanti processi di fondo, la stima dell'efficienza della selezione e degli errori sistematici, e i limiti superiori attesi per i rapporti di decadimento delle transizioni studiate, espressi come sensibilità dell'esperimento. Infine, il capitolo 5 riporta le considerazioni finali riguardo al lavoro svolto.

Chapter 1

Introduction

The study of the bottomonium spectroscopy and decays is an active research topic: here I introduce some of the methods and results that are most relevant with respect to the subject of the thesis. This chapter is organized as follows. In section 1.1 I give an overview of the present status of bottomonium spectroscopy. Section 1.2 presents an overview of the phenomenological and theoretical tools used for the description of heavy quarkonium dynamics and transitions. In section 1.3 I define the decay process under consideration and recall the topic of di-pion transitions between bottomonium states, being them the processes that lead to the observation of the $h_b(2P)$ state.

1.1 The bottomonium spectrum

Heavy quarkonia are bound states of a heavy quark Q with its corresponding anti-quark $\overline{Q}$. They are thus indicated with $Q\overline{Q}$ for brevity. Being quarks spin-1/2 fermions, the $Q\overline{Q}$ combination gives rise to a set of spin-singlet ($S = 0$) and spin-triplet ($S = 1$) configurations. Denoting with L the orbital angular momentum, it follows from Dirac's theory that a fermion-antifermion system can assume a set of J^{PC} quantum numbers, with $J = L+S$, $P = (-1)^{L+1}$ and $C = (-1)^J$, where J is the total angular momentum, P is the parity and C is the charge parity. Radial states are identified by the n quantum number. Using the spectroscopic notation, a particular state is unambiguously defined by the label $n^{2S+1}L_J$.

The only heavy quarks able to form bound states are the c (charm) and b (bottom) quarks, while the top quark has a too small lifetime due to its heavy mass. The states formed by the $c\bar{c}$ combinations are referred to as charmonia, while those formed by the $b\bar{b}$ combinations are called bottomonia.

Since the discovery of the $\Upsilon(1, 2S)$ resonances by the E288 experiment at Fermilab [1, 2], a lot of progress has been made in the field of $b\bar{b}$ spectroscopy. The $\Upsilon(nS)$ states are spin triplets with $L = 0$, thus they have $J^{PC} = 1^{--}$ quantum numbers. The fine splitting doesn't show up, contrarily to other triplet states, because the orbital angular momentum is zero and the relativistic corrections are small. The $\Upsilon(nS)$ can be directly produced in e^+e^- annihilations since they bring the same J^{PC} of the photon produced in the annihilation. The masses of the states can be predicted by using various phenomenological models, the simplest being the non-relativistic potential model described in section 1.2.2, or theoretically by performing lattice QCD calculations, introduced in section 1.2.6. One of the goals of spectroscopy is to verify the existence of predicted states and possibly to reveal the presence of other ones, which are not predicted or can't be explained in the framework of the existent models. Another essential goal is the measurement of their properties such as mass and width, and the observation of the various decay modes.

The major contributions to bottomonium spectroscopy come from the study of e^+e^- collisions by the ARGUS, CLEO, BaBar and Belle collaborations [3, 4, 5]. An important result is the determination of $\chi_{bJ}(1, 2P)$ masses via the observation of electric dipole (E1) transitions from $\Upsilon(3S)$ and $\Upsilon(2S)$ [6]. The E1 transitions are electromagnetic processes that result in the emission of a photon ($n\,^{2S+1}L_J \rightarrow n'\,^{2S'+1}L'_{J'} + \gamma$), in which $\Delta J = 0, \pm1$ (but $\Delta J = 0$ is forbidden if $J = 0$). The measurement of the masses of $\chi_{bJ}(1, 2P)$ is important because it allows for the determination of the fine structure splitting.

More recently, the BaBar and Belle experiments at asymmetric e^+e^- colliders collected an amount of data sufficient to observe new states and transitions, often with unexpected results. Among others, we can count the observation of $\Upsilon(4S) \rightarrow \pi^+\pi^-\Upsilon(1, 2S)$ transitions by BaBar [7] and of $\Upsilon(4S) \rightarrow \eta h_b(1P)$ by Belle [8]. The ground state $\eta_b(1S)$ has been found recently [9] by the BaBar collaboration studying the inclusive decays $\Upsilon(3S) \rightarrow \gamma X$.

Fig. 1.1 shows the current state of knowledge on the bottomonium spectrum, displaying both the established and the predicted but unobserved states. Note that the figure reports the $\Upsilon(5S)$ as the fourth radial excitation of $\Upsilon(1S)$. However, I will refer to this state as $\Upsilon(10860)$ as its interpretation is not fully understood. In fact, the latter denomination is the one followed by the Particle Data Group (PDG) [10].

The energy levels of the bottomonium system lie close to the sums of the masses of $B_{(s)}$ and $\overline{B}_{(s)}$ mesons, which are referred to as the open-bottom thresholds. The coupling of the $b\bar{b}$ system to the $(b\bar{q}, \bar{b}q)$ channels, being q a light quark, allows for the decay into $B_{(s)}\overline{B}_{(s)}$ pairs. Two classes of states can thus be defined in terms of the allowed decay modes. For states whose mass lies below the open-bottom threshold the decay into B meson pairs is kinematically forbidden. These resonances can thus decay only through OZI-suppressed hadronic decays and through electromagnetic processes [11], implying that they are narrow with respect to typical hadronic resonances. Indeed, the OZI rule states that a strong process is suppressed if the Feynman diagram describing it can be cut by a single line, in such a way that the initial state particles are all on one side and the final state particles on the other, while the cut passes through only gluon lines. This corresponds to the annihilation of quarks into virtual gluons, which carry all the energy of the process before the quark pair productions. The OZI rule is represented graphically in figure 1.2 for the suppressed $\phi \rightarrow \pi^+\pi^-\pi^0$ process. Also in the decays of quarkonium lying below the open-flavor threshold, three virtual gluons must mediate the interaction. The fact that at least three vertices are involved implies that the amplitude for such a process is proportional to $\alpha_s^{3/2}$ at leading order. In addition, the running coupling, introduced in section 1.2.1, yields a smaller value for α_s because the gluons carry a high energy.

On the contrary, states above threshold decay predominantly into $B\overline{B}$ pairs and their widths are much larger. As a comparison, the width of the $\Upsilon(3S)$ resonance is $\Gamma[\Upsilon(3S)] \approx 20\ keV$, while that of $\Upsilon(4S)$ is $\Gamma[\Upsilon(4S)] \approx 20\ MeV$,

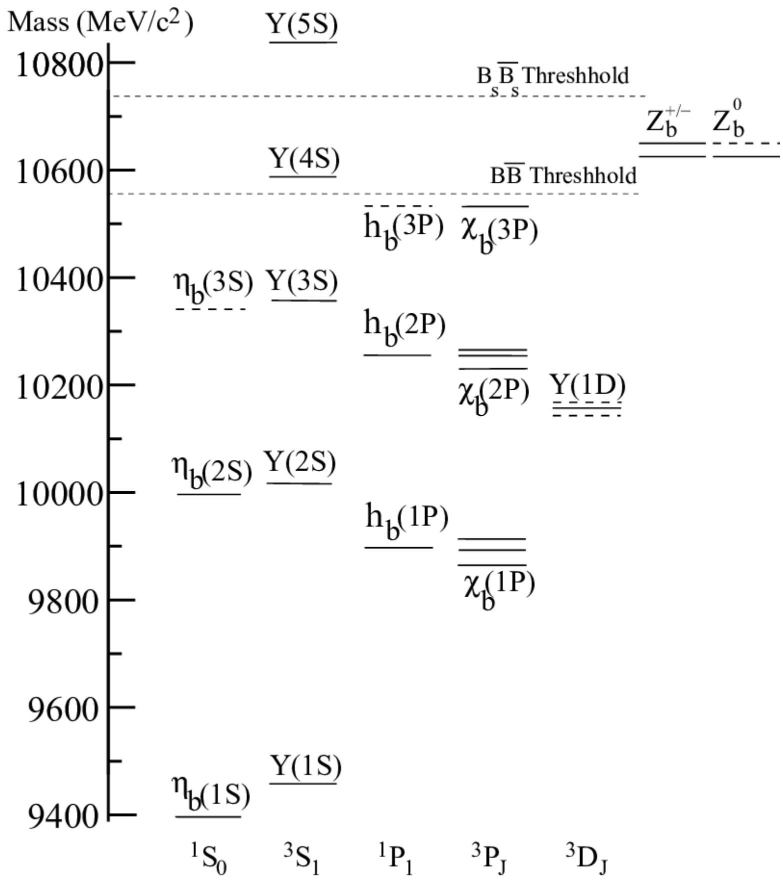

Figure 1.1: Current state of knowledge on the bottomonium energy levels. Solid lines represent experimentally established states, while dashed lines the predicted ones that are still unobserved.

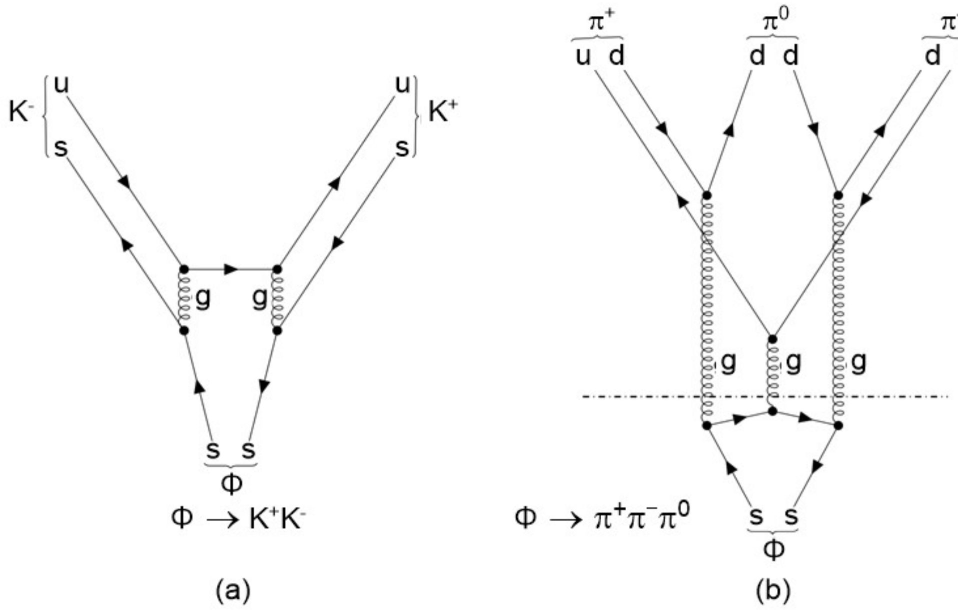

Figure 1.2: Illustration of the OZI rule for the favoured $\phi \to K^+K^-$ (a) and suppressed $\phi \to \pi^+\pi^-\pi^0$ (b) decays of the ϕ resonance.

three orders of magnitude larger.

Various models have been proposed to explain the nature of observed states, as well as to predict the others. The most relevant models are treated in the next section.

1.2 Phenomenological and theoretical models

The discovery of $Q\overline{Q}$ resonances inspired the development of new models for the description of hadrons containing heavy quarks: I give here an outline of these developments. The difference between a phenomenological and a theoretical approach can be stated as follows. In the former, the features of the strong interaction that are believed to be most relevant to heavy quarkonium are modeled in order to produce results which are then confirmed or rejected by experiments. In the latter approach the predictions come from calculations based on the established quantum field theory describing strong interactions (Quantum Chromo Dynamics or QCD).

The simplest approach in the phenomenological treatment of heavy quarkonia consists in the definition of a non-relativistic potential model inspired by QCD. This approach is described in section 1.2.2. Relativistic corrections are expected to be small in an approximately non-relativistic system. However they exist and can contribute to mass splittings and decay widths. The inclusion of relativistic corrections in the framework of potential models is discussed in sections 1.2.2 and 1.2.3.

At the present day, more modern phenomenological approaches relying on adaptations of QCD to specific energy scales are available as Effective Field Theories (EFTs). This subject is discussed in section 1.2.4.

A theoretical (and computational) approach, which studies the dynamics of quark and gluons on a lattice representing the discretized space-time, is attracting increasingly more interest in recent years, due to its predictability and the availability of higher computational power. This approach is referred to as Lattice QCD, which is introduced in section 1.2.6. In order to understand the various models, however, a brief recall on the most relevant features concerning strong interactions is necessary.

1.2.1 QCD and effective strong coupling

The gauge quantum field theory describing strong interactions between quarks and gluons is the Quantum Chromo Dinamics (QCD). The sources of the interaction are the charges carried from both quarks and gluons, that have an additional degree of freedom with respect to the electromagnetic charges. Since quarks come in three different configurations with respect to this intrinsic degree of freedom, the charge is referred to as color, taking inspiration from the RGB convention.

As the details of the theory are exhaustively described elsewhere [12, 13, 14], here I focus on its main properties, especially those that affect heavy quarkonia.

Besides the quark masses, the only free parameter appearing in the QCD Lagrangian is the strong coupling constant α_s, which is indicative of the strength of the interaction between two color charges. This parameter is defined in the context of perturbation theory, where the observable quantities are expressed in terms of powers of α_s. Like all quantum objects, the elementary fields have a ground state, that corresponds to the vacuum in the absence of particles. Because of the self energy, the interactive fields produce quark-antiquark pairs in the ground state, creating charges that polarize the vacuum. The vacuum polarization is the change in the quantum field ground state caused by the presence of a charge. As a consequence, α_s is not actually constant, but a function of the energy scale at which the interaction takes place. This property is referred to as running coupling. Consider two interacting color charges exchanging a four-momentum q: the energy scale at which the interaction takes place is q^2. The effective strong coupling as a function of the energy scale is calculated by using a renormalization technique [15]. In the case of minimal subtraction ($\overline{MS}$) scheme, the coupling is given by [10]

$$\alpha_s(q^2) = \frac{12\pi}{(33 - 2n_f) \times ln(q^2/\Lambda_{QCD}^2)} \tag{1.1}$$

where Λ_{QCD} is the scale at which the perturbatively-defined coupling would diverge, known as QCD scale, and n_f is the number of flavours of active quarks, i.e. quarks with masses much lower than q^2. The value of Λ_{QCD} has been estimated as $\Lambda_{QCD} \sim 200\ MeV$ [10]. The definition of light and heavy quarks may be given in terms of this parameter. Indeed, light quarks are those satisfying $m_q \ll \Lambda_{QCD}$, while heavy quarks are those satisfying $m_Q \gg \Lambda_{QCD}$.

The first implication of eq. (1.1) is that α_s decreases for increasing energy, and increases for decreasing energy. The latter effect reflects color confinement, that is the experimental evidence that colored particles are never observed as free. As we shall see later in the chapter, the running coupling has extremely important consequences in the treatment of heavy quarkonium dynamics. The decrease of α_s

for increasing energy is known as asymptotic freedom: at small distances, quarks tend to behave as if they were free from the strong interaction. This allows to use the perturbation theory for calculating transition probabilities in hard QCD processes.

These effects were discovered as general properties of gauge theories based on non-Abelian groups [16]. The running coupling is shown in figure 1.3 as a function of the exchanged momentum Q as a result of the measurement of different processes.

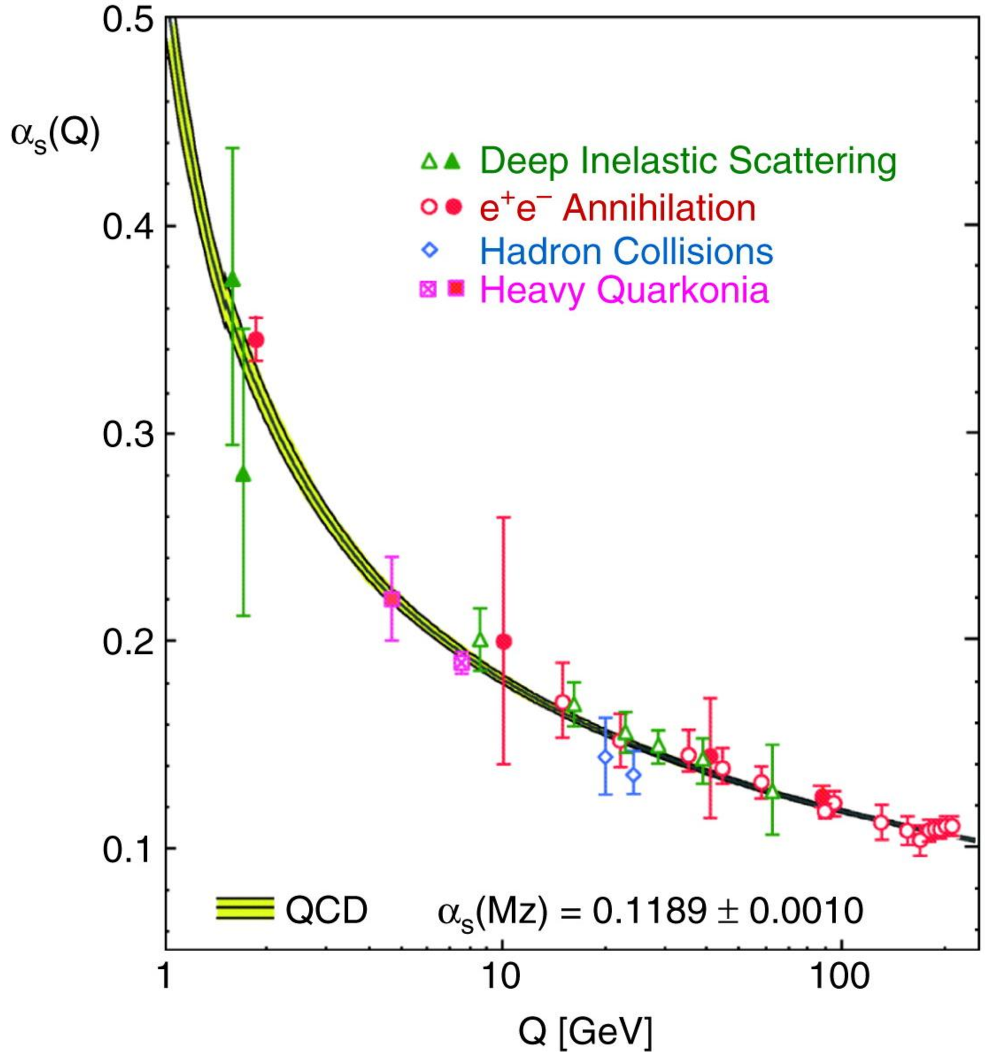

Figure 1.3: QCD running coupling from different measurements.

1.2.2 Non-relativistic potential model

The simplest approach for predicting the bottomonium energy levels is the non-relativistic potential model [17, 18, 19], where the system is treated with quantum mechanics. The development of such a model was encouraged by the large mass of the observed $c\bar{c}$ and $b\bar{b}$ states, leading to the hypothesis that the constituent quarks are heavy and non-relativistic.

In this framework, the short distance interaction is commonly assumed to be dominated by one-gluon exchange. The corresponding potential is Coulomb-like, i.e. $V(r) \propto 1/r$ for $r \ll 1/m$, being m the heavy quark mass. At large distances the potential has to comply with color confinement. The most popular choice is the Cornell potential [20]:

$$V_C(r) = -\frac{4}{3}\frac{\alpha_s}{r} + kr + const. \tag{1.2}$$

where the dependence of α_s on the radius r is neglected. This potential alone does not take into account the spin degrees of freedom, that contribute to the fine and hyperfine splittings in the spectrum. The spin dependence of the interaction can be taken into account by adding the corresponding ad hoc terms to eq. (1.2). This is explicitly given by the Fermi-Breit potential [21]

$$V_{sd} = V_{SS} + V_{LS} + V_T \tag{1.3}$$

where V_{SS} represents the hyperfine interaction, V_{LS} the spin-orbit coupling, and V_T the tensor forces.

The wavefunctions are derived by finding the eigenstates of the Hamiltonian, that is by solving the Schrödinger equation. Consequently, in such a model the spatial and spin degrees of freedom of the eigenstates are decoupled. The model parameters (α_s and k) are fit to experimental data in order to get the best agreement. Hence, this model is a tuned phenomenology rather than a satisfying theory, but it is by far the simplest possible description for heavy quarkonia and has been widely successful in describing the spectrum.

1.2.3 Relativistic Quark Model

The Relativistic Quark Model (RQM) [22] was originally built in order to extend the model described in the previous section to the dynamics of light mesons. In this approach, the Hamiltonian is modified in order to take into account relativistic effects starting from the quark kinematics. In the rest frame of a $q\bar{q}$ system, the Hamiltonian can be written as

$$\mathcal{H} = (p^2 + m_{\bar{q}})^{1/2} + (p^2 + m_q)^{1/2} + V(\vec{p}, \vec{r}) \tag{1.4}$$

where the $V(\vec{p}, \vec{r})$ potential is explicitly momentum-dependent. Such potential is defined, in analogy with the NR potential model, by the sum of a short-range Coulomb-like potential and a long range confining potential, plus spin-dependent terms. The key differences with respect to NR potential models are that here the short range potential takes into account the running of α_s by making explicit its dependence on r, while the confining potential is inspired by Lattice QCD calculations.

The wavefunction $|\psi\rangle$ corresponding to a particular state is found as the eigenstate of the Schrödinger-like equation $\mathcal{H}\,|\psi\rangle = E\,|\psi\rangle$, and the amplitude related to a specific transition is found as the matrix element of the corresponding interaction Hamiltonian. This formulation of relativistic effects implies that the spin-dependent interactions have an influence also on the spatial part of the wavefunction, contrarily to the NR potential model. The RQM finds an application in Ref. [23], where the widths of hadronic, electromagnetic and annihilation decays are predicted, including that of the transitions under study. These are given in section 1.3.1, where the topic of hindered M1 is covered.

1.2.4 Non-relativistic effective field theories

The running coupling phenomenon, introduced in section 1.2.1, has important consequences for the description of the $Q\overline{Q}$ system. Denoting with v the heavy quark velocity in the center of mass reference frame, for a non-relativistic system we have $v \ll 1$. In the case of $b\bar{b}$ bound states $v \sim 0.1$ [24]. Denoting with m the heavy quark mass, it can be seen that $Q\overline{Q}$ states are characterized by three scales:

- The hard scale, determined by the heavy mass m.
- The soft scale, due to the low relative momentum between the valence quarks $p \approx mv$. This is the scale of the momentum transfer inside the bound state.
- The ultra-soft scale, which characterizes the kinetic energy of the quarks in the center-of-mass frame $E \sim mv^2$.

Due to the fact that $v \ll 1$, these scales are hierarchically ordered and widely separated, i.e. $m \gg mv \gg mv^2$. The presence of this hierarchy introduces difficulties in the theoretical description of the system. Indeed, the different scales usually mix in Feynman diagrams necessary to calculate transition probabilities [25]. At high energy the observables can be expressed as powers of α_s, while at low energy nonperturbative effects dominate. Hence the heavy quarkonium system is the ideal environment for testing both the perturbative and nonperturbative QCD.

A modern approach to the description of NR bound states is the definition of a non-relativistic Effective Field Theory (NREFT). This approach takes advantage of the hierarchy of scales in order to factorize them at the Lagrangian level. The factorization is implemented via matching coefficients, called Wilson coefficients, that ensure the equivalence between QCD and NREFT at any given order of v. I give here a simple and brief overview of the possible variants of such approaches. For an extensive review on the subject see refs. [24, 25].

Non-relativistic QCD

The non-relativistic QCD (NRQCD) is obtained by integrating the hard scale m out of the Lagrangian operators, which will only contain the dynamical degrees of freedom associated to processes that occur at the soft and ultra-soft scale. Therefore, NRQCD describes the dynamics of heavy quark-antiquark pairs at energy scales much lower than their masses.

After the scale m is taken out of the Lagrangian operators, their matrix elements contain only the mv and mv^2 degrees of freedom, so that they can be expressed in powers of v. This is made explicit by constructing the NRQCD effective Lagrangian

$$\mathcal{L}_{NRQCD} = \sum_n \frac{c_n(\alpha_s(m), \mu)}{m^n} \times O_n(\mu, mv, mv^2, ...) \tag{1.5}$$

where O_n are the QCD operators that express the low energy dynamics, μ is the energy factorization scale, and c_n are the matching coefficients. The matrix elements of the operators can be obtained by non-perturbative methods such as lattice simulations.

Since processes such as quarkonium production and annihilation take place at the hard scale [25], they have been described using NRQCD in ref. [26]. Another application is the study of the bottomonium spectrum on the lattice [27, 28].

Potential non-relativistic QCD

In NRQCD, only the fact that $m \gg mv$ has been exploited, while no use is made of the hierarchy $mv \gg mv^2$. Another EFT called potential NRQCD (pNRQCD) can be built where also the soft scale is integrated out, and only the ultra-soft degrees of freedom are dynamical. This is done in such a way that pNRQCD is equivalent to NRQCD at any order of v and $\alpha_s(\mu)$ by employing matching coefficients. The relative coordinate r, whose typical size is the inverse of the soft scale, is explicit and can be considered as small with respect to the remaining dynamical lengths in the system. Therefore the pNRQCD Lagrangian is constructed not only order by order in 1/m, but also order by order in r. The matching coefficients depending on the spatial coordinate correspond to the $Q\overline{Q}$ potentials. There is more than one potential because separate matching coefficients are considered for color octet and singlet quark fields [29].

After this factorization, two complemtet and singlet entary situations can arise: $mv \gg \Lambda_{QCD}$ and $mv \sim \Lambda_{QCD}$. In the former, the matching from NRQCD to pNRQCD can be performed expanding in terms of α_s, that is perturbatively. In the latter case, the matching has to be non-perturbative [25]. These dynamical configurations are referred to as weak and strong coupling regimes, respectively. Weakly coupled pNRQCD has been used to predict M1 radiative transitions between S states [30].

The pNRQCD model bridges the gap between QCD and potential models, allowing to predict the leading relativistic corrections to the static potential with good precision [31].

1.2.5 Coupled-channel effects

Only the heavy valence quarks have been considered so far in the description of the $Q\overline{Q}$ system. However, the heavy quarks can couple to other (light) quarks. Indeed, the process $(b\bar{b}) \to (b\overline{q})(\bar{b}q)$ is responsible for the $B\overline{B}$ production from the decay of bottomonia lying above threshold. The same process could also induce the formation of hadronic loops via the production of virtual bottom mesons [32] as shown in Fig. 1.4. The mesons produced in the loop are denoted by their valence quarks $b\overline{q}$ or $\bar{b}q$, which are coupled by the strong interaction and thus confined in a bound state. For this reason, these processes are referred to as coupled-channel effects.

Since the coupling of above-threshold bottomonia to the $B\overline{B}$ final state is large, these effects should be important [32]. They can be added to potential models and influence the description of both the bound states and of particular decay modes. This is true even for states below threshold because of its proximity to the masses of $b\bar{b}$ states, and because the virtual B mesons can be off-shell.

Coupled channel effects can be described in the simplest way by coupling the bare $b\bar{b}$ states, which have a discrete spectrum, to the $B\overline{B}$ continuum. This is done by defining the proper interaction Hamiltonian $\mathcal{H}_I$, which is responsible for the mixing. The interactions between the constituents of the B and $\overline{B}$ mesons can be treated separately and are represented by the Hamiltonian $\mathcal{H}_{B\overline{B}}$. Denoting with $|\psi\rangle$ the state determined by the $b\bar{b}$ valence quarks and with $|\phi_B\phi_{\overline{B}}\rangle$ the continuum states, one has

$$\mathcal{H}_0 |\psi\rangle = M_{b\bar{b}} |\psi\rangle \tag{1.6}$$

where $\mathcal{H}_0$ is the NR Hamiltonian describing the $b\bar{b}$ state with bare mass $M_{b\bar{b}}$, and

$$\mathcal{H}_{B\overline{B}} |\phi_B\phi_{\overline{B}}\rangle = (E_B + E_{\overline{B}}) |\phi_B\phi_{\overline{B}}\rangle \simeq (m_B + m_{\overline{B}} + \vec{p}/\mu_{B\overline{B}}) |\phi_B\phi_{\overline{B}}\rangle \tag{1.7}$$

where $\vec{p}$ is the relative momentum between the B mesons, m_B and $m_{\overline{B}}$ are their masses and $\mu_{B\overline{B}}$ is the reduced mass. The full hadronic state, that takes the continuum states into account, can be represented in the rest frame by the $|\Psi\rangle$ state obeying

$$\mathcal{H} |\Psi\rangle = M |\Psi\rangle \, , \; \mathcal{H} = \begin{pmatrix} \mathcal{H}_0 & \mathcal{H}_I \\ \mathcal{H}_I & \mathcal{H}_{B\overline{B}} \end{pmatrix} . \tag{1.8}$$

where M is the difference between $M_{b\bar{b}}$ and the self-energy of the hadronic loop. The interaction Hamiltonian $\mathcal{H}_I$ clearly has to describe the creation or destruction of $q\bar{q}$ pairs, and is defined as [33]

$$\mathcal{H}_I = g \sum_q \int d^3\vec{x} \; \overline{\psi_q}(x)\psi_q(x) \tag{1.9}$$

where g is the coupling constant and $\psi(x)$ is the Dirac quark field.

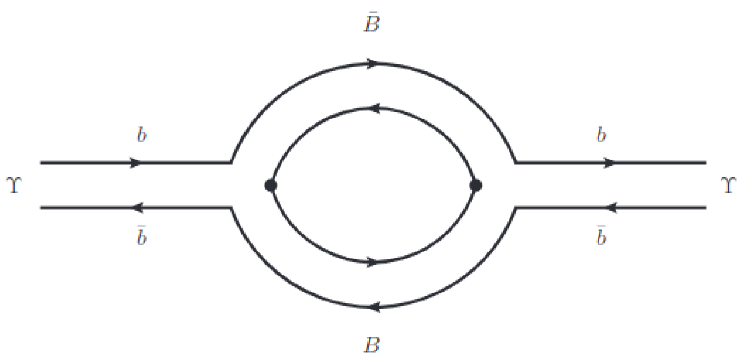

Figure 1.4: Diagram illustrating the coupling of the Υ meson with $B\overline{B}$ loops.

1.2.6 Lattice QCD

Lattice QCD is a numerical approach to solve problems related to non-perturbative QCD that exploits the Feynman path integral quantization. The path integral framework used in quantum mechanics allows to express transition amplitudes as the sum of amplitudes computed on every possible path connecting the initial and final states. Each path is weighted by the phase e^{iS}, where S is the action

$$S = \int \mathcal{L}\, dt \tag{1.10}$$

In a QFT the integrals are generalized to all fields configurations. In case of QCD, the action depends on quark $(\psi, \overline{\psi})$ and gluon $(\mathcal{A}_\mu)$ fields and their derivatives. A fundamental element is the partition function $\mathcal{Z}$, whose functional derivatives at specific points generate the correlation (Green) functions giving the evolution of the system. In addition, the Minkowski metrics is transformed to Euclidean metrics by means of a Wick rotation, so that the weight is e^{-S}. This avoid oscillation in the path integrals, starting from the partition function [34]

$$\mathcal{Z} = \int [\mathcal{D}\psi][\mathcal{D}\overline{\psi}][\mathcal{D}\mathcal{A}]\, e^{-S} \tag{1.11}$$

To predict physics observables such as the mass of a hadron or a transition width, the corresponding operators have to be defined into the theory. Their expectation values correspond to time ordered correlation functions of quark and gluon fields.

The numerical implementation of path integrals requires the discretization of space-time. The fields are transcripted on the lattice while preserving all the key properties of QCD, first of all gauge invariance. The possible field configurations are in principle infinite, thus they are generated numerically by means of Monte Carlo methods such as importance sampling [35]. Moreover, the Euclidean path integral is computed with Monte Carlo integration. Hence the measurements have statistical error in addition to the systematic errors, which are caused by the space-time discretization.

1.3 Transitions

In the previous sections, we have dealt with the basics of phenomenological and theoretical treatments which have been developed in the past years in order to describe the dynamics of the quarkonium states. However, we are interested in studying the transitions, and in particular the hindered M1 transitions $h_b(2P) \to \chi_{bJ}(1P)\gamma$. I thus give the definition of hindered M1 transitions in section 1.3.1, as well as the partial widths predictions for the considered channels.

Moreover, in section 1.3.2 I describe the mechanism responsible for the unexpectedly abundant production of the $h_b(2P)$ state, as observed by the Belle experiment in 2011.

1.3.1 M1 radiative transitions

The rates for hadronic and electromagnetic transitions are comparable for $Q\overline{Q}$ states lying below the open flavor threshold because of the OZI suppression [11]. For P-wave states, the widths of radiative transitions are larger than those of the hadronic ones [10]. Indeed, for what concerns the $h_b(2P)$ state, the only decays to lower bottomonia observed so far are the electric dipole transitions $h_b(2P) \to \eta_b(1,2S)\gamma$ [36].

Radiative transitions are in general useful to spectroscopy because they allow to produce states with different J through S-wave transitions, due to angular momentum conservation. In addition, measuring the widths of such transitions allows to test the theoretical models used to describe the internal dynamics of heavy quarkonia and their coupling to electromagnetism [37]. The emitted photons are monochromatic in the mother's rest frame and their energy is proportional to the splitting between the energy levels ($E_\gamma \sim 100\ MeV$), offering a clean signature for the observation of such processes.

Theoretically, the interaction is defined by coupling the bound system to an external EM field [38]. The Hamiltonian will contain an inter-quark potential describing the internal dynamics and operators representing the external interaction. The allowed decays are classified as electric and magnetic multipole transitions as for atoms and nuclei.

According to Brambilla and collaborators [25], the rates of M1 transitions ($n\,^{2S+1}L_J \to n'\,^{2S'+1}L_{J'} + \gamma$) are given by:

$$\Gamma_{M1} = \frac{16}{3}\alpha e_Q^2 \frac{E_\gamma^2}{m_i^2}(2J'+1)S_{fi}^M|\mathcal{M}_{fi}|^2, \tag{1.12}$$

where m_i is the mass of the initial state, S_{fi}^M is the statistical factor, and $\mathcal{M}_{fi}$ is the transition amplitude. The latter is given by the overlap integral

$$\mathcal{M}_{fi} = \int dr\ u'_{n'L}(r)u_{nL}(r)j_0(E_\gamma r/2), \tag{1.13}$$

where $u_{nL}(r)$ is the solution of the radial Schrödinger equation with n and L quantum numbers, and j_0 the zeroth-order spherical Bessel function. Note that the amplitude (1.12) is suppressed by the factor m_i^2 coming from the coupling of the $Q\overline{Q}$ magnetic moment to the EM field.

Considering that the mean radius of a $b\bar{b}$ state is $a \sim 0.1\ fm$ [12], we have that $E_\gamma a \ll 1$, so the integrand in (1.13) can be expanded in orders of $E_\gamma r$ and at first order $j_0(E_\gamma r/2) \approx 1$. The amplitudes then depend on how the wave-functions are derived. In non-relativistic potential models the spatial and spin degrees of freedom are decoupled and the radial wave-functions are orthogonal, so that $\mathcal{M}_{fi} = \delta_{nn'}$. Consequently, allowed M1 transitions are those with $n = n'$. The $n \neq n'$ transitions are forbidden at first order and are thus called hindered transitions.

The RQM includes relativistic corrections in such a way that the spin and spatial degrees of freedom are no more decoupled, as explained in section 1.2.3. As a result, the radial wave-functions change shape and the overlap integral (1.13) becomes finite for hindered transitions, leading to small widths. The partial widths

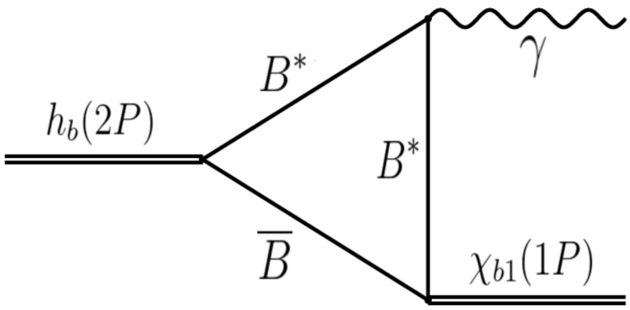

Figure 1.5: Example of a triangular loop due to coupled channel effects, leading to the $h_b(2P) \to \chi_{b1}(1P)\gamma$ transition.

Table 1.1: Partial width predictions for the decay channels under consideration from the RQM [23] and the coupled-channel model [39].

Process	$\mathbf{\Gamma_{part.}}$ **(RQM) (keV)**	$\mathbf{\Gamma_{part.}}$ **(c.c.) (keV)**
$h_b(2P) \to \chi_{b2}(1P)\gamma$	2.2×10^{-3}	25
$h_b(2P) \to \chi_{b1}(1P)\gamma$	1.1×10^{-3}	20
$h_b(2P) \to \chi_{b0}(1P)\gamma$	3.2×10^{-4}	7

predicted by this model are reported in ref. [23]. However, predictions for M1 transitions are affected by large uncertainties because the relativistic corrections depend on the defined Lorentz structure of the potential [24]. In addition, the $Q\overline{Q}$ system may carry an anomalous magnetic moment [25].

More recent results take into account coupled-channel effects. Indeed, a coupled-channel theory has been proposed for the description of hindered M1 transitions between P-wave bottomonia [39], where hadronic loops include the exchange of an additional B meson between the first produced $B\overline{B}$ pair, resulting in triangular loops like the one shown in Fig. 1.5.

In this context, radiative decays come from the coupling of the B^* meson to the EM field. However, a precise prediction for the decay widths is not possible as the coupling constants of the model are unknown. By taking the same estimates made for the charmonium case [40], the predicted widths for the considered channels are 3 – 4 orders of magnitude larger with respect to those predicted by RQM. The predictions from the two models are reported in table 1.1. The total width of the $h_b(2P)$ resonance can be assumed to be $\Gamma_{h_b(2P)} \approx 100\ keV$, so the predicted BFs are of order $10^{-6} - 10^{-5}$ in RQM and of order $10^{-2} - 10^{-1}$ in the coupled-channel model.

1.3.2 Di-pion bottomonium transitions

The Belle experiment took a large data sample of e^+e^- collisions at $\sqrt{s} \approx 10.860\ GeV$, corresponding to the state previously called $\Upsilon(5S)$. The integrated luminosity amounts to $L = 121.4\ fb^{-1}$. The analysis of such a sample resulted, among others, in the observation of $\Upsilon(10860) \to \Upsilon(nS)\pi^+\pi^-$, $n = 1, 2, 3$, and $\Upsilon(10860) \to h_b(mP)\pi^+\pi^-$, $m = 1, 2$, transitions with rates much higher than expected [41, 42]. The expectations were based on the measured widths of $\Upsilon(mS) \to \Upsilon(nS)\pi^+\pi^-$, with $m = 2, 3, 4$ [43, 44, 45]. These agree with the results of the standard theoretical treatment for hadronic transitions between heavy quarkonia, which uses the QCD multipole expansion (QCDME) model [46].

In QCDME, hadronic transitions are mediated by the emission of a soft gluon, which then undergoes hadronization producing light hadrons. Since the gluon has low momentum, the chromoelectric and chromomagnetic fields can be expanded in multipoles around the center of mass of the $Q\overline{Q}$ system in analogy with the EM case. The partial widths predicted by the model for di-pion transitions are of order $10^{-1} - 10\ keV$. The widths of $\Upsilon(10860) \to \Upsilon(nS)\pi^+\pi^-$, $n = 1, 2, 3$, are instead observed to be from two to three orders of magnitude larger. The widths are reported in table 1.2 where they are compared to the much lower $\Gamma[\Upsilon(3S) \to \Upsilon(1S)\pi^+\pi^-]$.

Table 1.2: Comparison of partial widths for di-pion transitions between Υ levels

Process	**Partial width**
$\Upsilon(10860) \to \Upsilon(3S)\pi^+\pi^-$	$(0.59 \pm 0.04 \pm 0.09)\ MeV$ [41]
$\Upsilon(10860) \to \Upsilon(2S)\pi^+\pi^-$	$(0.85 \pm 0.07 \pm 0.09)\ MeV$ [41]
$\Upsilon(10860) \to \Upsilon(1S)\pi^+\pi^-$	$(0.52^{+0.20}_{-0.17} \pm 0.10)\ MeV$ [41]
$\Upsilon(3S) \to \Upsilon(1S)\pi^+\pi^-$	$(8.9 \pm 0.8) \times 10^{-4}\ MeV$ [10]

In addition, those of $\Upsilon(10860) \to h_b(1,2P)\pi^+\pi^-$ transitions are of the same order, giving Belle a unique and large sample with $h_b(2P)$ production. This is another unexpected result since spin-flipping transitions between $b\bar{b}$ states are expected to be suppressed by a factor v in QCDME [38].

The amplitude analysis of di-pion transitions at the $\Upsilon(10860)$ reveals peaking structures in the invariant mass spectra of $\Upsilon(nS)\pi^\pm$ and in the $\pi^\pm$ recoil mass distribution, which are associated to the production of the bottomonium-like $Z_b^\pm(10610)$ and $Z_b^\pm(10650)$ charged states [47, 48]. The structures are shown in figure 1.6. Being the Z_b states charged, their minimum quark content is $qq\overline{qq}$. They have been thus proposed as tetraquark candidates [49]. Another possible interpretation explains the Z_b states as heavy meson molecules [50].

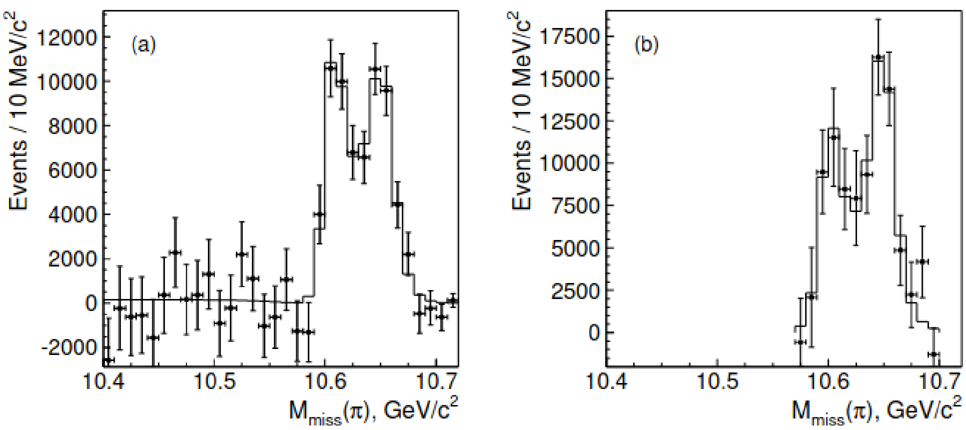

Figure 1.6: Yields of (a) $h_b(1P)$ and (b) $h_b(2P)$ as a function of the pion missing mass in the inclusive reconstruction of $\Upsilon(10860) \to h_b(1,2P)\pi^+\pi^-$ [47].

The non-resonant contribution for the $h_b(2P)\pi^+\pi^-$ final state is found to be consistent with zero, thus the $\Upsilon(10860) \to Z_b^{(\prime)\pm}\pi^\mp \to h_b(2P)\pi^+\pi^-$ transitions can be regarded as the only contributions in $h_b(2P)$ production. This aspect is important in setting the analysis for the search, as explained in section 4.1. The Z_b's dominantly decay into pairs of bottom mesons [51]. Based on this result, the decays to hidden bottom states via B meson loops have been investigated in [52], well reproducing the experimental data. This is another example of the application of a coupled-channel theory.

Summarizing, the $h_b(2P)$ discovery has been recalled to stress the fact that the Belle's data at $\Upsilon(10860)$ may be large enough to observe the transitions under study. These are predicted to be suppressed by potential models. However, examples have been given to show that the theoretical description of $Q\overline{Q}$ states and transitions is an open research topic. Experimental observations often result in puzzling behaviours that are inspiring the birth of new models. The study of coupled-channel effects giving rise to heavy meson loop diagrams is of recent interest in the modeling of both the bound states and transitions.

Chapter 2

The Belle experiment

In this chapter I focus on the description of the experimental apparatus used by the Belle experiment throughout its activity. The analysed data is produced in e^+e^- collisions at the KEKB collider, located in Tsukuba, Japan. A schematic view of the facility is shown in Fig. 2.1. The main features of KEKB are briefly described in section 2.1.

The event reconstruction and the study of physics processes are possible thanks to the information given by the complex, general purpose Belle detector. Section 2.2 presents an overview of the detector and its subsystems.

2.1 The KEKB B-factory

The main goal of the Belle experiment is to study the time-dependent CP violation in the B sector. In order to achieve this goal the KEKB collider had to satisfy a set of conditions, that guided its design specifications. The most promising way to detect time-dependent CP violation is to measure the relative phase between the amplitudes of the $B^0 \to J/\psi K_s^0$ and $\overline{B}^0 \to J/\psi K_s^0$ decays [53]. The two channels have really low ($\sim 10^{-4}$) branching ratios, thus a fundamental requirement for the collider is that of a high luminosity. The KEKB collider reached a peak instantaneous luminosity of order $\mathcal{L} \sim 10^{34}\ cm^{-2}\ s^{-1}$, setting a world record in the field. The collider operated for over ten years, starting the data taking in 1999 and finishing in June, 2010.

Another important requirement is related to kinematics. Indeed, $B^0\overline{B}^0$ pairs are copiously produced in $\Upsilon(4S) \to B^0\overline{B}^0$ transitions, hence the default beam energy of KEKB is tuned on the mass of the $\Upsilon(4S)$ resonance. The $\Upsilon(4S)$ mass lies just 20 MeV above the $B\overline{B}$ threshold, thus in the parent's rest frame the two mesons are produced nearly at rest. This would imply a major difficulty for the main purposes of the experiment. Indeed, the measurement of the time-dependent CP violation requires the determination of the time interval between the decays of the two B mesons. Since they have a short mean lifetime ($\tau \approx 1.5\ ps$), their decay lenght in the laboratory is rather small if they are produced with a low kinetic energy. In order to increase the decay lenght, another requirement for the collider is the use of asymmetric beam energies to boost the produced $B\overline{B}$ pairs with respect to the laboratory frame.

Asymmetric energies imply the adoption of a dedicated storage ring for each beam. At the KEKB facility, electrons were accumulated in the High Energy Ring (HER) at the energy $E_{HER} = 8.0\ GeV$, while positrons in the Low Energy Ring

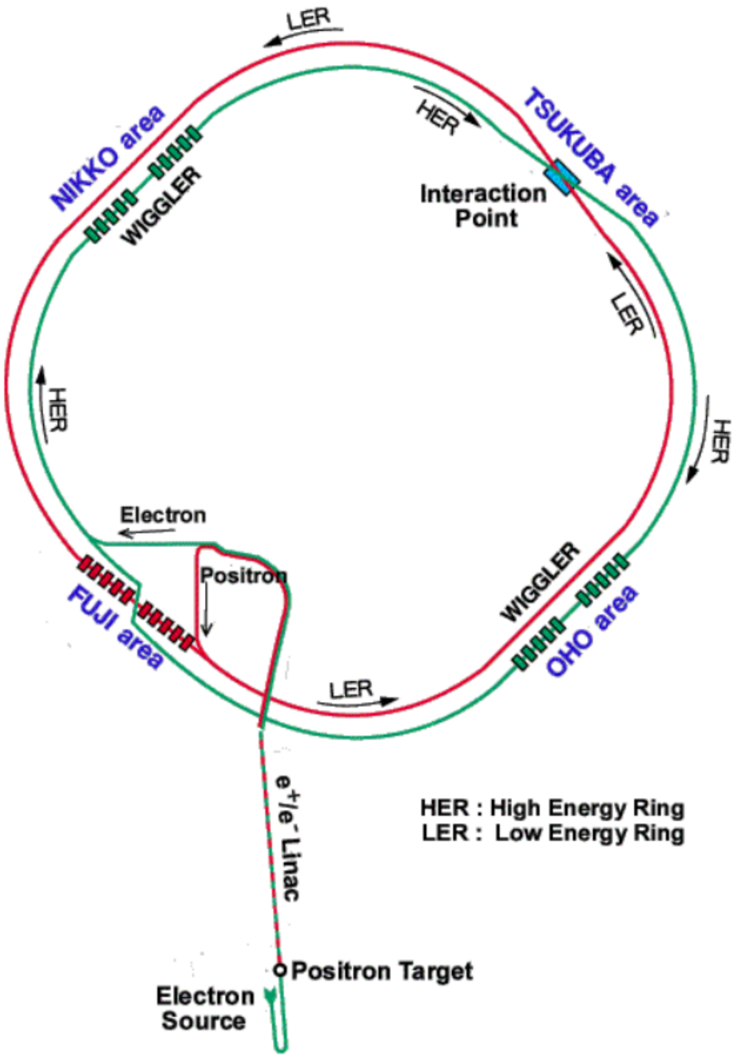

Figure 2.1: Schematic view of the KEKB collider facility.

Table 2.1: Summary of the luminosity integrated by Belle.

Resonance	**On-peak luminosity** (fb^{-1})	**Off-peak luminosity** (fb^{-1})
$\Upsilon(1S)$	5.7	1.8
$\Upsilon(2S)$	24.9	1.7
$\Upsilon(3S)$	2.9	0.3
$\Upsilon(4S)$	711	89.4
$\Upsilon(10860)$	121.4	1.7
Scan		27.6

(LER), with $E_{LER} = 3.5\ GeV$. The energy of the collision in the center of mass reference frame is usually denoted as $\sqrt{s}$, being $s = (p^{\mu}_{e^+} + p^{\mu}_{e^-})^2$, where p^{μ} is the four-momentum.

In order to optimize the luminosity, the facility had only one Interaction Point (IP), which was surrounded by the Belle detector.

Due to the high branching fraction of the $\Upsilon(4S) \rightarrow B\overline{B}$ processes ($\approx 96\%$), an e^+e^- collider working at this energy is called a B-factory. Another example of a B-factory has been the PEP-II collider, which was located at SLAC, Stanford, where the Babar detector operated during the data taking.

Besides the study of CP-violation parameters, the B-factories turned to be extremely useful in other sectors of particle physics, such as the quarkonium sector. Indeed, all quarkonium states with $J^{PC} = 1^{--}$ can be produced in e^+e^- annihilations, by tuning the beam energy or by exploiting the emission of Initial State Radiation (ISR). In the latter case, one of the two colliding particles emits a hard photon γ_{ISR} in the initial state. This is a consequence of radiative corrections to QED theory. The result is a decrease of $\sqrt{s}$, which transforms into $\sqrt{s'} = \sqrt{s} - E_{\gamma_{ISR}}$. This allows to directly produce 1^{--} bottomonia and charmonia in e^+e^- annihilations.

Figure 2.2 shows the integrated luminosity of the Belle and Babar experiments as a function of time. It can be seen that the total Belle's integrated luminosity exceeds 1 ab^{-1}. More than 100 fb^{-1} were integrated at the $\Upsilon(10860)$ resonance, allowing to perform interesting measurements above the better known $\Upsilon(4S)$. This made Belle the only experiment in the world able to observe the anomalous width of di-pion transitions at the $\Upsilon(10860)$, and the associated production of the Z_b exotics. Table 2.1 reports a summary of the integrated luminosity for the Belle experiment, ordered by increasing center of mass energy.

2.2 The Belle detector

The Belle detector is a magnetic spectrometer covering a wide portion (91%) of the full solid angle. A magnetic field of magnitude $B = 1.5\ T$ is provided by a superconducting solenoid, in a cylindrical region with length 4.4 m and diameter 3.4 m. An iron structure surrounds the whole detector, serving as the return path for the magnetic field flux.

The beam pipe placed around the IP is made of beryllium in order to minimize the material budget, because of its short radiation length x_0. This choice

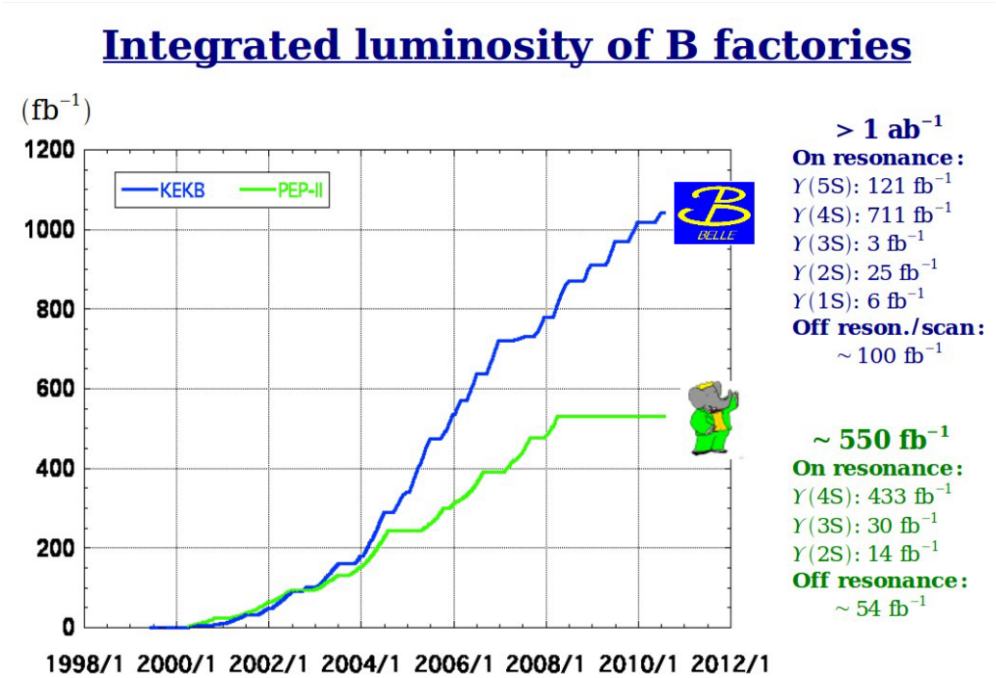

Figure 2.2: Integrated luminosities of the Belle and Babar collaborations versus time.

helps reducing the occurrence of multiple scattering and energy loss of final state particles inside the walls of the pipe.

The Belle detector is composed of various sub-detectors, which are shown in Fig. 2.3. The sub-detectors are listed here from inner to outer:

- Silicon Vertex Detector (SVD), composed by four layers of silicon strip detectors in the latest upgrade. While the main goal of this system is to measure the decay vertices, it also contributes to tracking.
- Central Drift Chamber (CDC), a chamber filled with low-Z gas used for the tracking of charged particles, as well as dE/dx measurements.
- Time-of-flight (TOF) detector, a system made of plastic scintillator counters used for particle identification (PID) and triggering.
- Aerogel Cherenkov Counter (ACC), an array of threshold Cherenkov detectors used as part of the PID system.
- Electromagnetic calorimeter (ECL), an array of CsI(Tl) crystals mainly used to detect photons and measure their energy.
- K_L and muon detector (KLM). This system identifies muons and K_L's over a wide momentum range for $p > 600\ MeV$.

The detailed description of each sub-detector is given below in the corresponding section. The main reference used throughout this section is the KEK report [54].

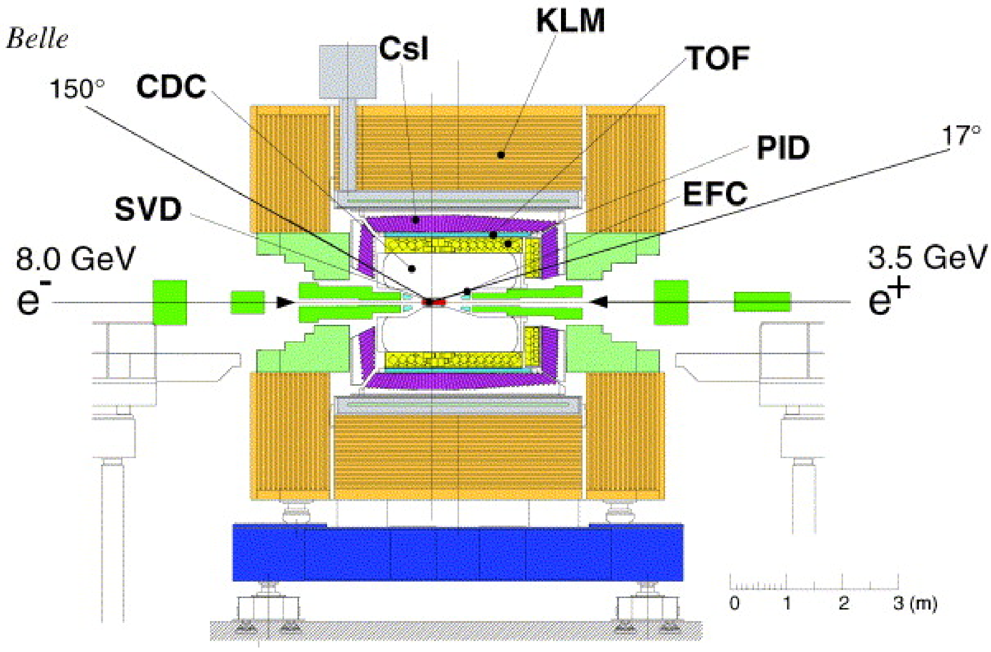

Figure 2.3: Side view of the Belle detector.

2.2.1 Silicon Vertex Detector

In order to measure the decay vertex position with a good resolution, the silicon vertex detector is placed right outside the beam pipe.

Three versions of the SVD operated over the duration of the experiment. The first version (SVD1) consisted of three layers of double-sided silicon strip detectors (DSSD). A DSSD is a p-n diode enclosed between two sets of segmented electrodes, each of which is connected to an independent readout circuit. Electrons and holes created by the passage of ionizing particles travel along the electric field lines to the corresponding electrode, allowing for the measurement of the position of the interaction between the incident radiation and the detector. In double-sided detectors, strips belonging to one side are arranged orthogonally to those of the other side, such that both the r and ϕ coordinates can be measured by a single layer.

Due to the low distance ($\sim cm$) from the IP and their solid-state nature, this sub-detector and its readout system suffered the highest radiation damage. One of the main limitations of the SVD1 is the poor radiation tolerance of readout electronics [55]. In addition, the SVD1 covered the polar range $23° < \theta < 139°$, smaller than the CDC angular acceptance. The first upgrade was called SVD1.5 and consisted in the update of the readout system.

During the Belle shutdown in 2003 the SVD2 upgrade has been installed. This new version had four layers and extended the polar acceptance to that of the CDC. In addition, the distance of the first layer with respect to the IP was reduced in order to improve the vertex resolution.

The impact parameter resolution is a function of the pseudo-momentum of the incident particle. The pseudo-momentum absorbs the momentum and angular dependence into a single variable, and is defined as $\tilde{p} = p\beta sin^{3/2}\theta$. The measured resolution for the $r-\phi$ and z coordinates is shown in Fig. 2.4 for both SVD1 and

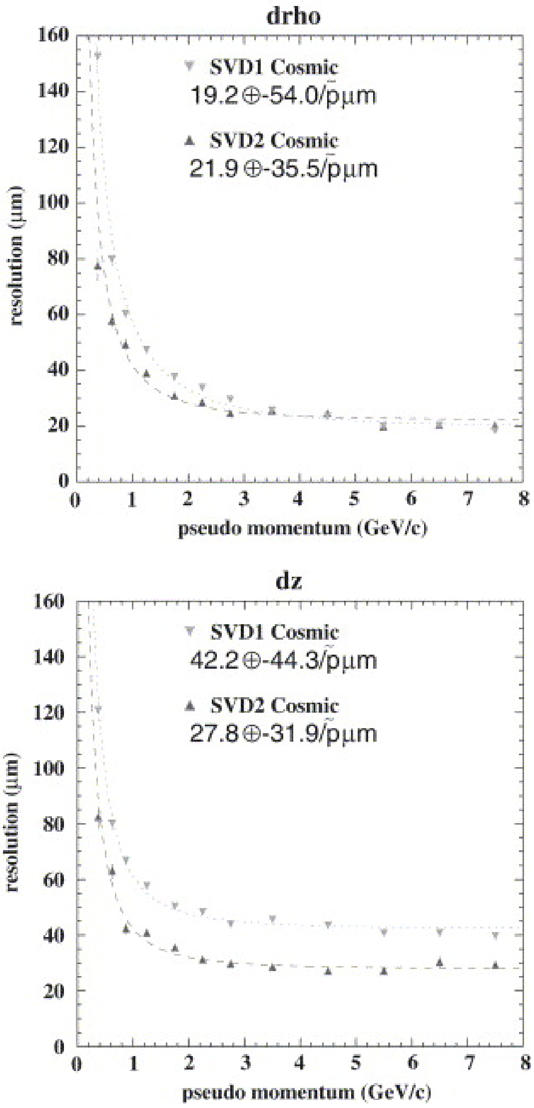

Figure 2.4: Impact parameter resolution for the $r-\phi$ and the z coordinates versus track pseudo-momentum.

SVD2. The SVD2 upgrade shows a significant improvement for low-momentum tracks with respect to the SVD1.

All the data analyzed throughout this thesis were taken with the SVD2 configuration. The layout of the SVD2 is shown in Fig. 2.5.

2.2.2 Central Drift Chamber

The essential ingredient used for the tracking of charged particles is the Central Drift Chamber. The basic working principle of a drift chamber is the collection of charge carriers that are freed by the ionization of gas molecules. Charged thin wires placed inside the chamber provide a radial electric field. The anode wires, used for the collection of electrons, are alternated to cathode wires which shape the field lines. The high intensity of the electric field close to the anode wires accelerates the electrons, allowing for secondary ionization and thus for the multiplication of the charge, which amplifies the signal. Away from the wires,

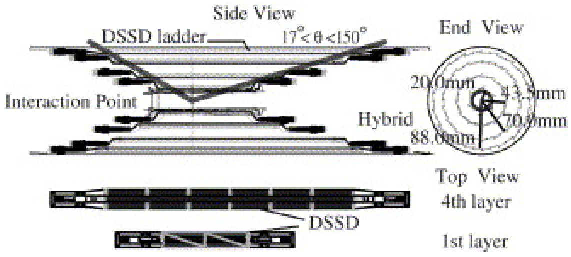

Figure 2.5: The design of the SVD2 detector.

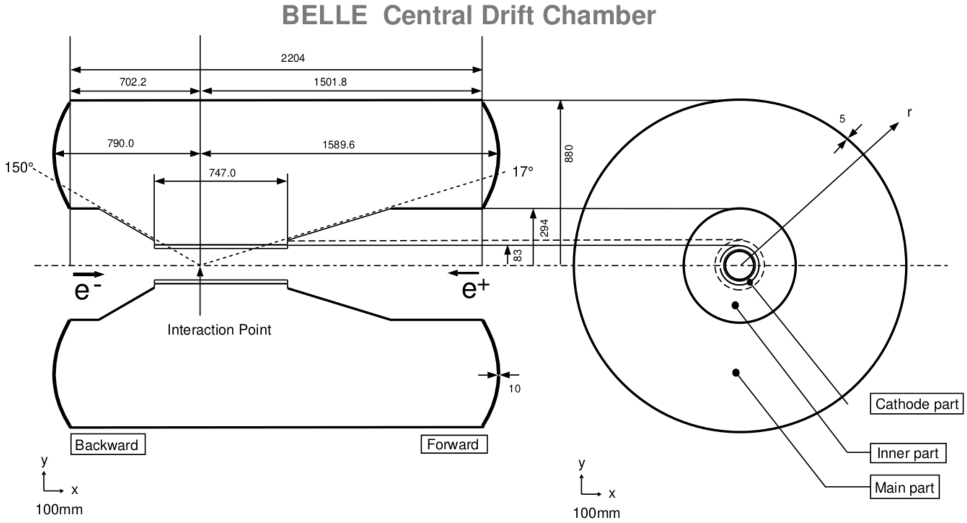

Figure 2.6: Structure of Belle's CDC.

the velocity of an electron moving in the chamber saturates at a certain value called drift velocity. As a consequence, the position of the ionization can be easily estimated by measuring the time interval between a reference instant and that of the charge collection.

The structure of the Belle drift chamber is shown in Fig. 2.6. The CDC is asymmetric over the z axis in order to maximize the acceptance. The innermost part of detector is designed and constructed with a conical shape to keep it as close as possible to the IP. This allowed to successfully track charged particles with $p_T > 50\ MeV$. The angular coverage corresponds to $17° < \theta < 150°$.

The main requirement for this sub-detector is the minimization of multiple scattering in order to achieve a good momentum resolution, while retaining a good dE/dx resolution useful for PID information. This can be done by employing a low-Z gas mixture, but a too low Z affects the dE/dx resolution because ionization processes are less frequent. A 50% He - 50% C_2H_6 mixture has been eventually chosen as a trade-off between these requirements.

2.2.3 Time Of Flight detector

A straightforward way to identify a particle is to measure its mass. Having measured the momentum p, one needs to measure another kinematical variable to determine the mass, because of the relation

$$p = \beta\gamma mc. \tag{2.1}$$

The working principle of TOF detectors is to measure the particle velocity β, hence the γ Lorentz factor, by measuring the time taken by the particle to travel a distance L. Due to relativistic kinematics, for a given momentum p the time of flight Δt is easily mapped to the mass m:

$$\frac{\Delta t}{L} = \frac{1}{c}\sqrt{1+\frac{m^2c^2}{p^2}} \approx \frac{1}{c}\left(1+\frac{m^2c^2}{2p^2}\right). \tag{2.2}$$

Besides ionization, the passage of charged particles through matter can lead to the excitation of the molecules composing such matter. If the de-excitation occurs via the emission of photons in the visible range, the material is called scintillator. If the scintillator is coupled to a photon detector such as a photomultiplier (PMT), the system is called a scintillation counter.

The Belle TOF sub-detector used plastic scintillator counters. Plastic scintillators are made of organic material and exhibit a fast response to the energy deposition ($\sim$ 100 ps). The rapidity of the response is exploited by including the detector in the trigger system, described in section 2.2.7.

A single module consists of two trapezoidally shaped TOF counters and a more coarsely segmented Thick Scintillator Counter (TSC). With a total of 64 modules located at radius 1.2 m from the IP, the sub-detector covered the polar region 34° $< \theta <$ 120°.

2.2.4 Aerogel Cherenkov Counter

Another way to identify a moving particle is the detection of the Cherenkov radiation through a medium, which gives information on the velocity. Denoting with n the refractive index of the material, a particle traveling at $\beta \geq 1/n$, i.e. faster than the speed of light in the medium, radiates at a fixed angle $\theta = \arccos\frac{1}{\beta n}$ with respect to its direction. $\beta_t = 1/n$ is referred as the threshold velocity. At a fixed momentum, by properly choosing n, only particles with mass less than a given value give rise to a signal in the counter. The Aerogel Cherenkov Counter (ACC) system is optimized for π/K separation in a momentum range not covered by the dE/dx information and TOF measurements. It consists in 960 modules of aerogel counters with a refraction index between 1.01 and 1.03 depending on the polar angle region.

The modules are arranged in a barrel and a forward endcap region as shown in Fig. 2.7.

2.2.5 Electromagnetic Calorimeter

The main goal of the ECL is to measure the energy of detected photons. The electromagnetic calorimeter consisted of 8736 CsI(Tl) crystals arranged in a barrel region and two annular endcap regions, as shown in Fig. 2.8. It covered 91% of the solid angle, with a 3% loss of acceptance due to the gaps between the regions that hosted cables and supports for the inner detectors. Each crystal is positioned

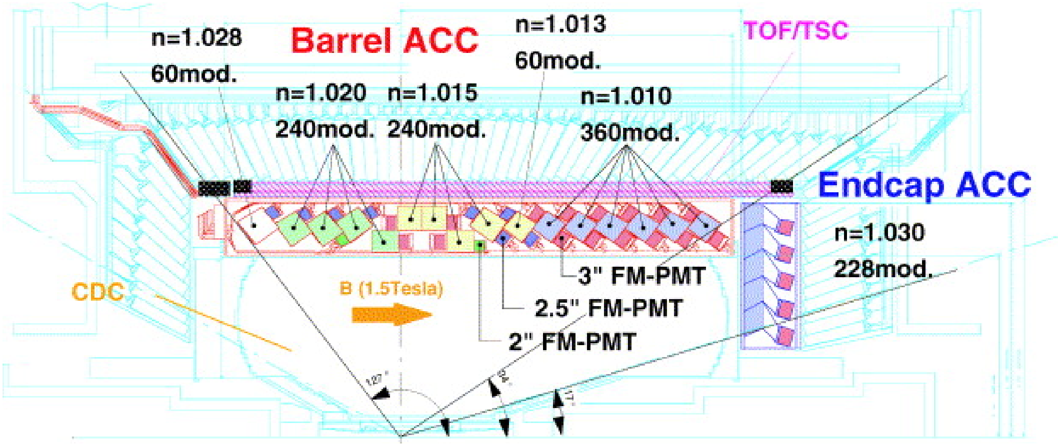

Figure 2.7: Belle's ACC detector.

such that it pointed approximately to the IP. To further extend the ECL polar angle coverage, and, the Extreme Forward Calorimeter (EFC) was designed.

CsI(Tl) is an inorganic scintillator. The scintillation mechanism follows from its crystalline structure, where the allowed energy states for an electron in the medium lie in the continuum valence and conduction bands, that are separated by a forbidden energy gap.

For a pure CsI crystal, the absorption of energy from the incoming radiation can result in the excitation of an electron into the conduction band. The subsequent return of the excited electron to the valence band with the emission of a photon is allowed, but highly inefficient. In addition, the energy gap for the pure crystal is such that the wavelength of peak emission is outside the visible range ($\lambda \sim 300\ nm$). This poses a difficulty for the conversion of the emitted photons into an electric signal.

The addition of Tl impurities introduces energy levels inside the forbidden energy gap, allowing for the emission of a visible photon. Moreover, the Tl activator enhances the light yield from $\sim 2000\ photons/MeV$ for pure CsI to $\sim 65000\ photons/MeV$ [56].

At high energies ($\gtrsim 100\ MeV$) photons interacting with the calorimeter lose their energy via pair production. Electrons and positrons produced in this way lose energy by emitting bremsstrahlung radiation and occasionally by producing δ rays inside the crystal. These phenomena originate the development of electromagnetic showers. A simple model for this process is given in [57].

One of the conclusions of the model is that at least 10-15 radiation lengths are needed in order to contain a fraction larger than 95% of the incident photon's energy. The depth of the ECL crystals is chosen to be 30 cm, corresponding to $16.2x_0$.

As a consequence of multiple scattering of electrons and positrons, the shower spreads laterally. The transverse dimension of the crystals varied with respect to θ. However, the typical dimensions were $6 \times 6\ cm^2$. This size is chosen such that approximately 80% of the energy released by a photon injected at the center of a crystal is contained in that crystal, while spreading the remaining fraction into the neighbours in order to form a cluster of fired crystals.

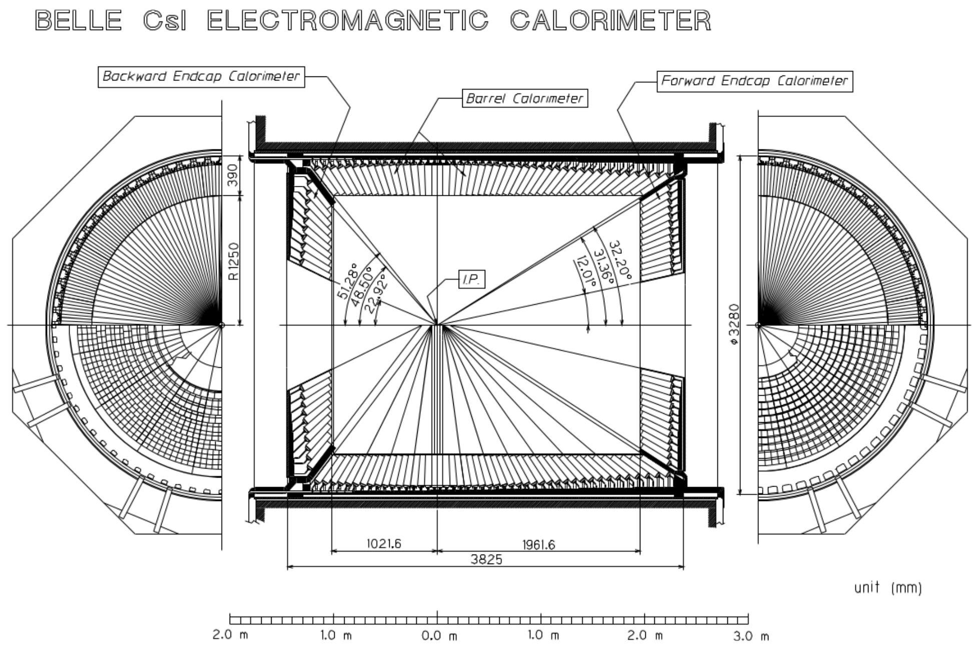

Figure 2.8: The Belle electromagnetic calorimeter.

The light output of each counter is read out by two independent silicon PIN photodiodes. Those were connected to charge-sensitive pre-amplifiers, whose output is transferred to a shaping circuit used to sum the two signals. The summed signal is split into two streams: one for the data acquisition and the other for the trigger circuit.

For the sake of spectroscopy, a high precision is required in the measurement of the energy of the incident radiation. Since the emission of light from the scintillator is related to stochastic processes, the light output fluctuates even for a perfectly monochromatic incident beam. In addition to statistic fluctuations, other sources such as electronic noise contribute. The spread of the detector's response under a monochromatic incident radiation defines the energy resolution. The lower this spread, the better the resolution.

The energy resolution is determined by irradiating the ECL with electron, pion and photon beams. It is measured by summing the energy deposit in 3x3 and 5x5 crystal blocks. Its expression is a quadratic sum of three terms:

$$\frac{\sigma_E}{E} = \frac{0.0066\%}{E} \oplus \frac{1.53\%}{E^{1/4}} \oplus 1.18\% \tag{2.3}$$

for the 3x3 sum, and

$$\frac{\sigma_E}{E} = \frac{0.066\%}{E} \oplus \frac{0.81\%}{E^{1/4}} \oplus 1.34\% \tag{2.4}$$

for the 5x5 sum. E is expressed in units of GeV.

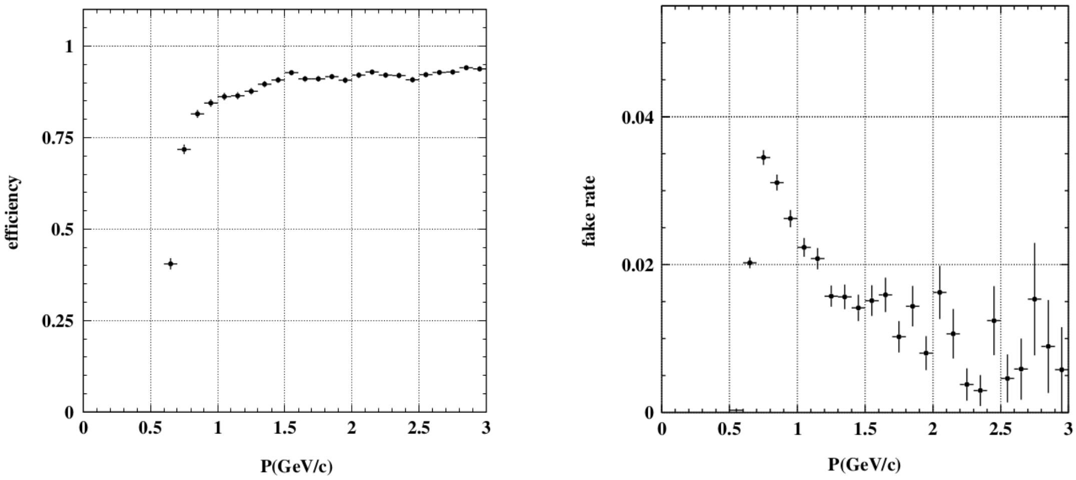

(a) (b)

Figure 2.9: The measured muon detection efficiency (a) and fake rate (b) of the KLM detector as a function of momentum.

2.2.6 K-long and muon detector

The KLM detector is designed in order to detect K_L's and muons with a high efficiency and purity. It is made of alternating layers of RPCs and iron plates, arranged in a barrel region and two endcap regions.

A K_L interacting with an iron nucleus produces a shower of charged particles, which can be detected by the sensitive part of the KLM. On the contrary, muons do not interact strongly with matter, thus they travel a longer distance and their direction is weakly deflected. This allows to discriminate between muons and hadrons based on the penetrated range and transverse scattering.

A single RPC consists of two parallel plate electrodes separated by a gas filled thin gap. The typical gap voltage is of 8 kV, therefore the detector operated in the streamer mode. In this configuration, an ionizing particle passing through the gas starts a streamer that induces a discharge on the plates. The plates were made of glass because of its high resistivity ($> 10^{10}\Omega\ cm$), that limits the amplitude of the spark, thus avoiding the overloading of the readout electronics.

The discharge of the plates induces a signal on external strips, that measure the spatial and temporal coordinates of the ionization. In the KLM detector two RPCs were sandwitched between orthogonal pickup strips.

The muon detection efficiency as a function of momentum is shown in Fig. 2.9a.

In track reconstruction, charged pions and kaons may be misidentified as muons. The relative frequency of these occurrences is defined as fake rate. In order to measure the fake rate, Belle used a sample of $K_S \to \pi^+\pi^-$ events collected in e^+e^- collisions. The measured fake rate versus momentum is shown in Fig. 2.9b. It can be seen that for muons with $p > 2\ GeV$ the detection efficiency is higher than 90% and the fake rate lower than 2%.

2.2.7 Trigger system

The e^+e^- collisions can occur when bunches of electrons and positrons cross each other. However, most of the time no interaction takes place, or the final state is not of interest (for example in Bhabha events). In addition, the high beam current necessary for the high luminosity leads to high beam background rates ($\sim 100\ Hz$), that must be kept within the tolerance rate of the data acquisition system (max. $500\ Hz$). Thus, the events have to be triggered and filtered. The trigger conditions must lead to high efficiency for interesting physics events while limiting the background.

The Belle trigger system is composed by a hardware and a software part. The former is referred to as the Level 1 trigger and is made of the sub-detector trigger systems communicating with a central system called Global Decision Logic (GDL). The GDL combines the information coming from sub-detector triggers and characterizes the event type. There are two classes of sub-detector trigger systems: track triggers, which discriminate tracks originating in the IP from background tracks, and energy triggers, which are based on the energy deposit. The key element of the track trigger is the CDC, whose output signal gives information on track count. The energy trigger is instead based on the ECL. The minimum unit constituting a trigger cell is composed by 4x4 adjacent crystals. The operation scheme of the Level 1 trigger is sketched in fig. 2.10. The latency of the Level 1 trigger, that is the delay with respect to the event occurrence, is fixed to 2.2 μs.

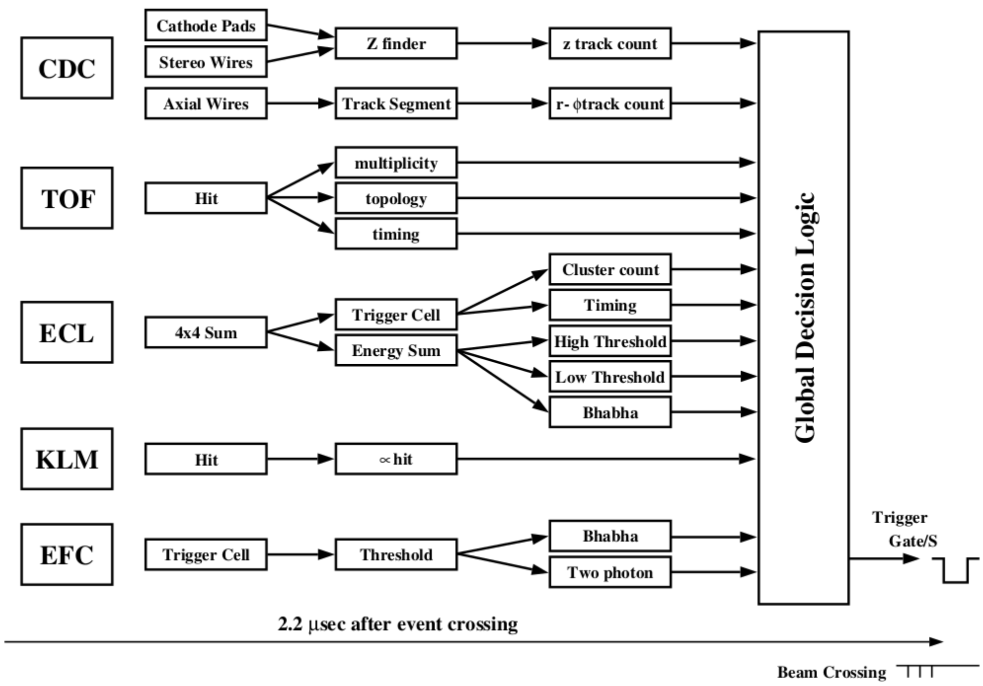

Figure 2.10: The Level-1 trigger system for the Belle detector.

2.3 Data production

The event data is transformed into an offline format by using a software trigger (Level 3 trigger) employing a fast tracking program, which reduces the beam background [58]. This is implemented by using an online computer farm consisting in a set of six VME crates, which contain processors used for the event filtering and the data storage. The throughput of the combined crates is 15 MB/s, corresponding to a maximum of 500 Hz for the trigger rate and of 30 kB for the event size.

The data is transferred from the computing farm to a tape library with sequential access. The size is readily reduced by running reconstruction algorithms on raw data, resulting in the production of Data Summary Tables (DSTs) which aim to contain information regarding only physics events. Just before the full event reconstruction, another software trigger (Level 4) is used to further reduce the background, while retaining a high efficiency for interesting events. The background is mostly due to spent electrons and positrons from the beam, which are the $e^{\pm}$ undergoing bremsstrahlung or Coulomb interactions with the nuclei of the residual gas in the pipe, thus deviating from the designed path. The Level 4 selection requires at least 4 GeV of energy deposit in the ECL and at least one one track with $p_T > 300\ MeV/c$ coming from near the IP. Events satisfying these requirements are selected immediately and submitted to the full reconstruction chain without further processing. The efficiency of the Level 4 trigger selection is higher than 98% for all hadronic events.

The DST is the starting point for a physics analysis: the first step is reducing the data size by applying a loose selection that keeps the efficiency high. This process is referred to as skimming. Different skims giving subsamples of the whole data are produced by the collaborators based on the physics events of interest and are then used to conduct analyses by starting with a smaller sample with respect to the full DST. In this analysis no suitable skim is already available at Belle, thus I define the skim selection as described in section 4.4.1.

Chapter 3

Software

Throughout the analysis, I rely on information gathered from Monte Carlo (MC) simulations in order to compare results with expectations and to study the event selection while keeping real data blinded, until the selection requirements are frozen. The event selection follows the event reconstruction. The latter is made possible thanks to the reconstruction algorithms, that combine the information coming from the various sub-detectors to form particle candidates. In order to comply with these complex tasks, I use the software developed by the Belle II collaboration. For the data analysis I use specific software, based on either the C++ or Python languages.

This Chapter focuses on the description of the software used through the thesis work. In section 3.1 I give a basic description of the CERN ROOT software, which is ubiquitous in any particle physics analysis. Section 3.2 describes the `basf2` software, being it the main tool used for the decay reconstruction and event selection. Section 3.3 contains the description of the software used for MC simulations. The reconstruction process is explained in detail in section 3.4. The offline data analysis is performed mainly using Jupyter notebooks and is described in section 3.5.

3.1 ROOT

ROOT is the standard software used by experimental particle physicists, being designed to efficiently store and analyze big data. It is an open source C++ object-oriented framework developed by the dedicated team at CERN, containing about 3000 classes. These can be extended by the user based on specific needs.

One of the main purposes of ROOT is to store large amounts of data. Once the dictionary of a specific class has been built, ROOT can store any object in binary files via its I/O interface. Thanks to the CLING interpreter, ROOT knows where object's data members are allocated in memory, what their size is, and how to store them.

Usually the data are written and read by using TTree objects (trees), which are optimized for I/O speed and memory usage. Trees are made of branches, defined by the TBranch class, which can contain objects, individual data members, arrays of objects, or simply C++ types. Different branches can be used to store independent objects, e.g. physics variables obtained in the event reconstruction. ROOT trees can be analyzed in different ways, by using the GUI for simple tasks or by employing C++ macros. In addition, dedicated python libraries can be used, as explained in section 3.5.

3.2 `basf2`

Even though the analyzed data belong to the Belle experiment, the analysis of the Data Summary Tables is performed with the Belle II Analysis Software Framework, abbreviated with `basf2`. This is the software used by the Belle II collaboration in all aspects of the data processing chain. Belle and Belle II data formats differ in some aspects. Since Belle's DSTs have a different structure with respect to those of Belle II, a data conversion has to be run prior to perform the reconstruction, in order to match the `basf2` data format. A special module called B2BII (Belle to Belle II) has been developed by the Belle II collaboration for this purpose [59]. After the conversion, the algorithms developed for the analysis of Belle II data can be exploited. These are defined in the source code of `basf2` modules.

The smallest building block of `basf2` is called module. A module corresponds to a piece of C++ code which is functional to a single purpose, e.g. reconstruct a decay process or save variables to an output ROOT file. The underlying code of each module is written and maintained by all collaborators.

Modules are arranged linearly in a chain called path, the specific arrangement depending on the user's objectives. One or more paths are created in order to process the data and save the results in an output ROOT file for further analysis (offline analysis). The whole script containing the data processing is referred to as steering file. The outline of a generic steering file is illustrated in figure 3.1.

A storage called DataStore contains mutable objects, or arrays of them, which can be exchanged from one module to another. Each module has read and write access to the data storage. A very important kind of stored data consists in the detector conditions at any run of the experiment: the conditions data lies in a storage called DBStore, which can be loaded from a central database server. This is essential for all physics analyses since most of the kinematic variables depend on the accelerator and detector conditions.

A package is a logical collection of code: a typical package has several modules and python scripts which configure paths in order to perform complex tasks. As an example, the `kinfit` package, containing modules that perform different kind of kinematic fits, is used in the analysis.

The `basf2` software has an interface with `python3`, so that the steering script can be entirely written in this language. Various modules can be arranged in a very simple way using python functions called wrappers, which are defined by the collaboration or by the user. The modules and packages used in the analysis are outlined in section 3.4.

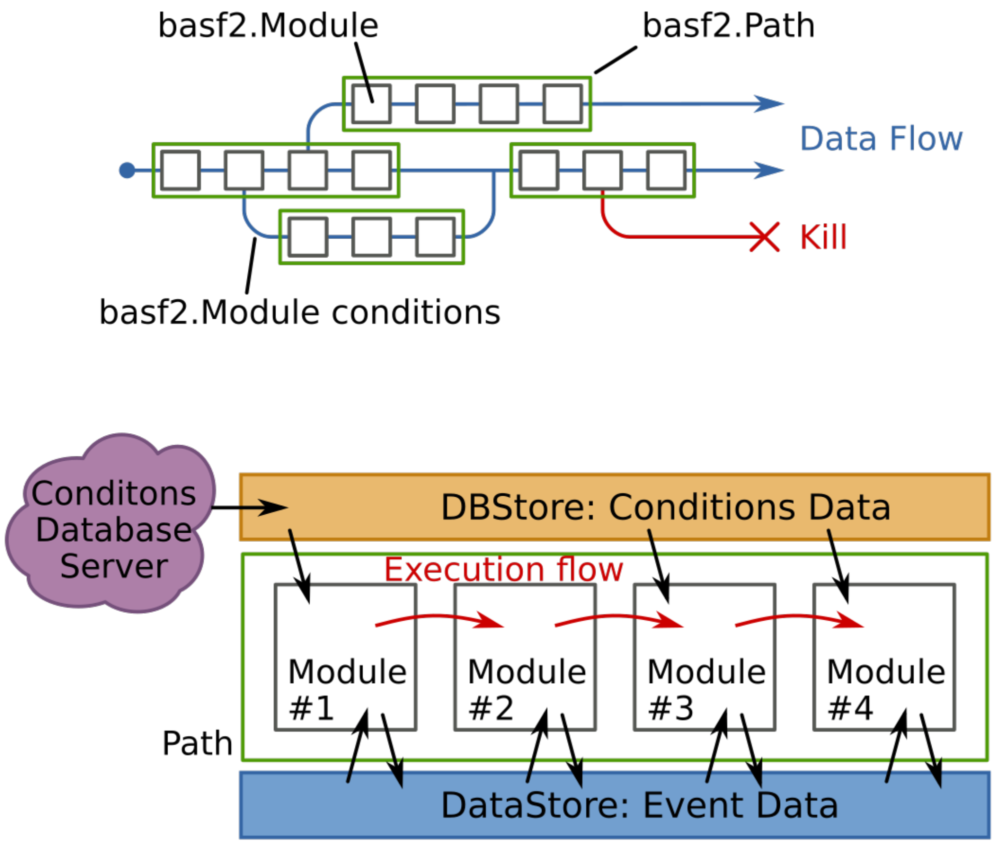

Figure 3.1: Schematics of the workflow of a `basf2` steering file.

3.3 MC simulation

A full MC simulation can be divided in two major steps: the event generation, which concerns the production and decays of specific particles with definite properties, and the full simulation of the passage of particles in the detector materials. The former is accomplished with the `EvtGen` software [60]. `EvtGen` is an event generator suitable for heavy flavor physics . It is interfaced to other generators as `JetSet` [61] and `PHOTOS` [62]. The `Jetset` generator is used to handle the direct production of $u\overline{u}$, $d\overline{d}$, $s\overline{s}$, $c\overline{c}$ pairs from e^+e^- collisions. The `PHOTOS` routine simulates processes involving radiative corrections to QED.

A fundamental input to `EvtGen` are the useful particle properties. A list of particles, along with their properties such as mass, spin, charge and PDG code, is contained in a special file called `evt.pdl`, which is parsed at runtime for generation.

The decays of an unstable particle are regulated by the proper physics models which follow from the underlying interactions driving such decays. For example, the decay of a vector particle into a charged lepton pair proceeds through the `VLL` model, which stands for "Vector to Lepton Lepton". Each decay model is implemented as a C++ class and can be defined to handle a specific decay mode or many different decays. The simplest model is the `PHSP` model, which stands for "Phase Space" and can handle a generic n-body decay by calculating its phase space and averaging all spins. A more specific model, which I use extensively in the analysis, is the `HELAMP` model. This model handles two-body decays and allows to simulate the appropriate angular distributions which follow from the ratios between the helicity amplitudes. Section 4.1.1 is dedicated to this subject.

The decaying particle and the model corresponding to a specific decay is defined by the user in a file called decay table. Here the involved particles must be named as in the `evt.pdl` file and each decay mode must be preceded by the corresponding branching fraction (BF) and succeded by the model parameters. All the decay tables related to our analysis are shown in appendix A.

The generated particles are propagated through the detector material using `GEANT-3` [63]. The `GEANT` program has been developed at CERN starting from 1978 as a tool to describe complex detector systems and simulate their interactions with ionizing particles. The materials are specified by their physical features such as atomic and mass number, density and radiation length: these parameters affect the radiation-matter interactions.

Plenty of interactions are simulated. For example, the simulation of the energy loss for a muon traversing a medium is the result of ionization, bremsstrahlung, direct e^+e^- production and nuclear interactions. Other examples of simulated processes are pair production by photons approaching nuclei, and delta ray production by electrons and muons. All these processes are simulated using MC methods, once the probability distribution function corresponding to a specific process has been coded into the program and the material/particle properties are used as parameters.

3.4 Reconstruction

The reconstruction consists in several steps. The starting point is the creation of one or more paths used to arrange the needed modules. Next, the input DST has to be loaded to read the data, containing information from detector sources. This is accomplished by the corresponding RootInput module. The FillParticleList module uses the information coming from the detector to create lists of stable particles, that are then combined to form candidates for the unstable particles. The ParticleCombiner module makes these combinations in order to reconstruct the decay processes. The latter are described through input decay strings as for the LHCb software [64]. The selection can be performed by using the appropriate cut string, which can manipulate both candidates and events.

If the steering script runs on MC it is usual to perform the MC matching, that consists in setting relations between the reconstructed and generated particles, returning the true PDG code of reconstructed particles, in addition to an error flag which gives information on the errors in the reconstruction or in the matching itself. Indeed, the MC matching is performed using algorithms that can fail sometimes. For example, in the matching of reconstructed photons, the dedicated algorithm analyzes the energy deposition of particles generated in the ECL electromagnetic shower and associates a weight to each one. The highest weighted candidate could be a secondary electron created in the shower, leading to a matching error because of the different PDG code with respect to the photon.

After the final state particles have been combined to form unstable particle candidates, the interesting information can be written out to a ROOT file in the form of TTrees, which are commonly called ntuples. The written information can be a physics variable, such as the invariant mass of a multi-particle system, or information at the event level such as the number of detected photons, or the experiment and run number.

The unstable particles can be reconstructed starting from charged tracks detected in the CDC and SVD, and from photons detected as ECL clusters. Here I describe how the tracking and particle identification are implemented in the software, since this information is used extensively throughout the analysis.

3.4.1 Tracking

The tracking of charged particles is performed with the CDC and SVD detectors. Tracks are parameterized as helices, which are defined by five parameters and a pivotal reference point $\mathbf{x_0} = (x_0, y_0, z_0)$. The coordinate system is defined by the xyz axes. The definition is as follows:

- z axis, taken to be anti-parallel to the LER momentum vector.
- y axis, pointing to the vertically upward direction.
- x axis, in the horizontal direction so that the system is right-handed.

It is crucial to measure the time of occurrence of the event. To this purpose, the leading edge of the charge-to-time converter providing the TOF trigger signal is used to give a common stop to all the other sub-detectors. This determines

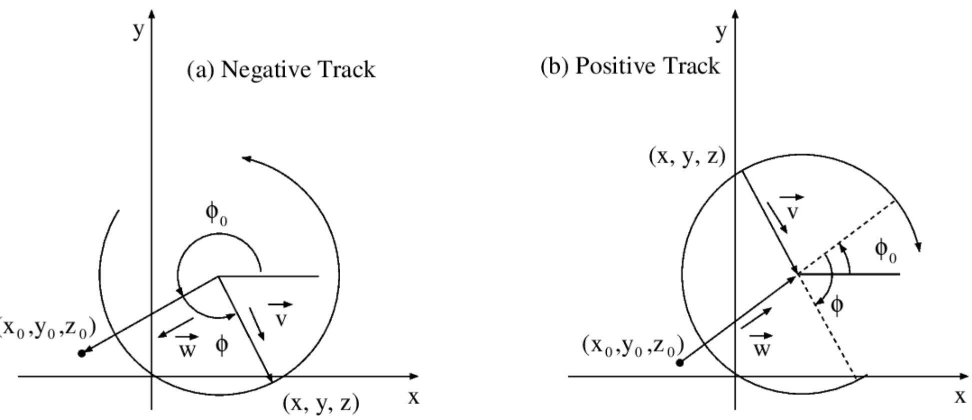

Figure 3.2: Schematic representation of the track parameters. The vectors are defined by $\vec{x} = \vec{x}_0 + (dr + r)\vec{w} - r\vec{v}$, where $\vec{w} = (cos\phi_0, sin\phi_0)$ and $\vec{v} = (cos(\phi_0 + \phi), sin(\phi_0 + \phi))$

the event time, which is the fundamental input for calculating the position of the CDC hits with respect to the anode wires collecting the signal.

The track fitting is performed by using the Kalman filtering method. This corresponds to an iterative least square fit. The use of the Kalman filter allows to apply corrections to effects due to the non uniformity of the magnetic field and to multiple scattering. The pivotal point of each track segment is transformed at every step in order to simplify calculations when applying the corrections.

The helix parameters found by the fit are:

- dz is the longitudinal (along the beam axis, z) component of the point of closest approach (POCA) of the track with respect to z.
- dr is the distance of the POCA from the beam axis in the plane $r - \phi$, which is orthogonal to z.
- κ is the inverse of the tranverse momentum p_T. Its sign represents the charge of the particle.
- ϕ_0 is the angle of the transverse momentum in the $r - \phi$ plane with respect to the x axis.
- $tan\lambda$ is the slope of the track.

They are sketched in figure 3.2 in the case of positive or negative charge.

The p_T resolution is studied using di-muon events. After combining the information given by the CDC and SVD detectors, the resolution is given by [65]

$$\sigma(p_T)/p_T = (1.64 \pm 0.04)\% \tag{3.1}$$

3.4.2 Particle identification

The particle identification (PID) at Belle is based on likelihood ratios. As described in section 2.2, the information mainly comes from the CDC, TOF and

ACC subdetectors. The separation between two particles α and β is provided by

$$\frac{\mathcal{L}(\alpha)}{\mathcal{L}(\alpha)+\mathcal{L}(\beta)} = \frac{\mathcal{L}_{\alpha}^{CDC}\mathcal{L}_{\alpha}^{TOF}\mathcal{L}_{\alpha}^{ACC}}{\mathcal{L}_{\alpha}^{CDC}\mathcal{L}_{\alpha}^{TOF}\mathcal{L}_{\alpha}^{ACC}+\mathcal{L}_{\beta}^{CDC}\mathcal{L}_{\beta}^{TOF}\mathcal{L}_{\beta}^{ACC}} \tag{3.2}$$

where $\mathcal{L}$ corresponds to the likelihood function determined by the respective particle hypothesis.

For the electron identification also the ECL information is used. Specifically, the discrimination between electrons and hadrons is based on the matching between the track extrapolated to the ECL and the position of the ECL cluster, on the energy over momentum ratio (E/p), where E is measured by the ECL and p by the CDC, and on the transverse shower shape in the ECL. The discriminants allow to calculate the electron (e) and non-electron ($\bar{e}$) likelihood functions based on probability density functions (PDFs).

For the identification of muons, hits in the KLM are compared to the track extrapolated from the CDC and SVD detectors. Two quantities are used to test the hypothesis that the observed particle is a muon rather than a hadron. The first quantity is the difference between the measured and expected range of the track, denoted with ΔR. The measured range is determined by the outermost KLM layer with an associated hit, while the expected range is given by the outermost layer crossed by an extrapolated track. The other quantity is the transverse deviation of the hits with respect to the extrapolated crossing points, normalized to the number of hits, and labeled with χ_r^2. The PDF $p(\Delta R, \chi_r^2)$ used to build the likelihood is defined assuming the two variables are uncorrelated, so that the joint PDF is given by the product of two single variable PDFs.

The mathematical definition of the PID variables for the separation of electron or muons from hadrons (e_{ID} and μ_{ID} respectively) are defined in section 4.2.4.

3.5 Offline data analysis

The saved data can be analyzed directly with ROOT via the GUI or by writing C++ macros. However, in recent years various python I/O libraries have been developed in order to read the ROOT data format and stream it to libraries used for high level analysis. The uproot library [66] is a Python implementation of ROOT I/O, independent on ROOT itself, that allows to cast data contained in ROOT files to different formats such as those provided by the python libraries numpy and pandas.

Once the data has been converted to a python readable format, it can be conveniently analyzed using Jupyter notebooks [67]. The Jupyter Notebook is an interactive, web-based environment which extends the console-based approach, allowing to create documents which contain both python code and explanatory markdown text. The code, organized in cells, can be executed from a web browser and the result are attached to each code cell.

Chapter 4

Analysis

4.1 Setup

In this analysis I search for the hindered magnetic dipole transitions between spin-singlet state and spin triplet states $h_b(2P) \to \gamma\chi_{bJ}(1P)$.

The production of $b\bar{b}$ spin-singlets is generally rare in e^+e^- collisions because it requires the spin flip of a heavy quark in a hadronic or radiative transition. Nevertheless, $h_b(2P)$ is produced via the $\Upsilon(10860) \to h_b(2P)\pi^+\pi^-$ transition with a surprisingly large rate [42]. The $h_b(2P) \to \chi_{bJ}(1P)\gamma$ transitions are the target of the search and are modeled as described in section 4.2.2. Moreover, the $\chi_{bJ}(1P)$ have large radiative decay to the $\Upsilon(1S)$ which can subsequently decay in a μ pair. The radiative decays $\chi_{bJ}(1P) \to \gamma\Upsilon(1S)$ are thus chosen to tag the final state of the M1 transition, so that there are two photons in the cascade.

The signal is searched by reconstructing the complete decay chain $\Upsilon(10860) \to h_b(2P)\pi^+\pi^- \to \gamma\chi_{bJ}(1P)\pi^+\pi^- \to \gamma\gamma\Upsilon(1S)\pi^+\pi^- \to \gamma\gamma\mu^+\mu^-\pi^+\pi^-$. The $h_b(2P)$ production is assumed to proceed exclusively through the intermediate $Z_b(')$ resonances as sketched in figure 4.1, where the decay chain is shown. From the sketch it can be seen that the full chain is a cascade of two body decays. The presence of hard leptons, pions and photons with no missing energy allows us to significantly reduce the contributions from $e^+e^- \to q\bar{q}$, $e^+e^- \to l^+l^-$ and the other low-multiplicity processes leading to an almost background-free analysis. As control sample I use the decay $\Upsilon(3S) \to \gamma\chi_{bJ}(2P) \to \gamma\gamma\Upsilon(2S) \to \gamma\gamma\pi^+\pi^-\Upsilon(1S) \to \gamma\gamma\pi^+\pi^-\mu^+\mu^-$ reconstructed in the $\Upsilon(3S)$ data sample. This choice of the control channel is motivated by the fact that the final state contains the same particles as for the signal, and the kinematics are very similar. The PDG values for the branching fractions involved in the signal cascade are reported in table 4.1. The predicted BFs for the hindered M1 transitions are reported in table 1.1.

Table 4.1: Branching fractions reported by PDG for the processes involved in the signal cascade decays.

Process	**BF**
$\Upsilon(5S) \to h_b(2P)\pi^+\pi^-$	$5.7^{+1.7}_{-2.1} \times 10^{-3}$
$\chi_{b2}(1P) \to \Upsilon(1S)\gamma$	18.0 ± 1.0
$\chi_{b1}(1P) \to \Upsilon(1S)\gamma$	35.2 ± 2.0
$\chi_{b0}(1P) \to \Upsilon(1S)\gamma$	1.94 ± 0.27
$\Upsilon(1S) \to \mu^+\mu^-$	2.48 ± 0.05

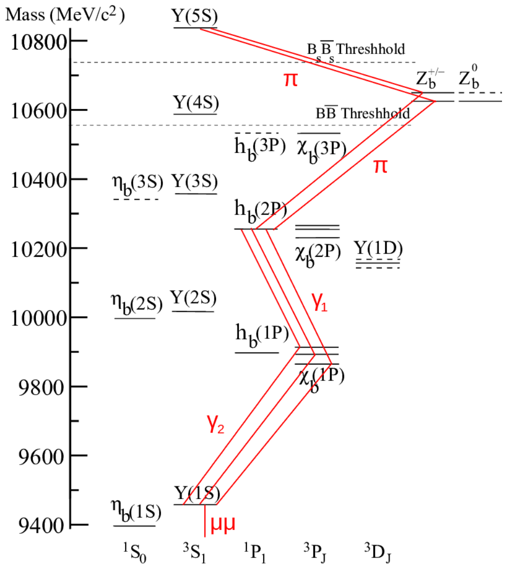

Figure 4.1: Diagrams of the signal decay chain targeted by this analysis.

4.1.1 Helicity amplitudes

The analysis begins with the generation of MC samples for the signal transitions. Consequently I have to consider which model to use in the generation in order to best represent the dynamics. All the particles involved in the signal processes have definite spin, angular momentum and parity quantum numbers. This property influences the angular distributions for the final state particles. In order to simulate the correct angular distribution, that affects the signal efficiency due to the detector acceptance, the HELAMP model is used, which is fed with the ratios between the transition amplitudes expressed in the helicity basis. This section contains a brief description of the helicity amplitude formalism and explains how the amplitudes are calculated in this case.

The helicity of a particle with spin $\vec{s}$ and momentum $\vec{p}$ is defined as the projection of the spin along the direction of motion:

$$\lambda = \frac{\vec{s} \cdot \vec{p}}{|\vec{p}||\vec{s}|}. \tag{4.1}$$

It may also be defined as the component of the total angular momentum $\vec{J}$ along the direction of motion. Note that λ is invariant under rotations, allowing to construct states with definite J and J_z in which the involved particles also have definite helicity. Considering a two-body decay $A \to B + C$, in the rest frame of A the daughters are emitted back-to-back with relative momentum p. Denoting with θ and ϕ the polar angles giving the direction of p in a fixed coordinate system xyz, the two particle state is found as

$$|p\theta\phi\lambda_B\lambda_C\rangle = R(\phi, \theta, -\phi)\,|p\lambda_B\lambda_C\rangle \tag{4.2}$$

where $R(\phi, \theta, -\phi)$ represents an Euler rotation and can be written in terms of separate rotations around the fixed coordinate system [68]

$$R(\alpha, \beta, \gamma) = R_z(\alpha) R_y(\beta) R_z(\gamma). \tag{4.3}$$

The matrix element of this operator between two angular momentum states $|Jm\rangle$ and $|Jm'\rangle$ is given by the D functions:

$$D^J_{m,m'}(\alpha, \beta, \gamma) = \langle Jm| R(\alpha, \beta, \gamma) |Jm'\rangle \tag{4.4}$$

which are related to the Wigner d-function by the equation

$$R(\alpha, \beta, \gamma) = e^{-im\alpha} d^J_{m,m'}(\beta) e^{-im'\gamma}. \tag{4.5}$$

Now I want to express the two particle state by using the J and M quantum numbers, where M is the component of $\vec{J}$ along the z-axis, in addition to the helicity values. The relation with $|p\theta\phi\lambda_B\lambda_C\rangle$ is given by [69]

$$|pJM\lambda_B\lambda_C\rangle = \sqrt{\frac{2J+1}{4\pi}} \int_{d\Omega} D^{*J}_{M,\lambda_B-\lambda_C}(\phi, \theta, -\phi) |p\theta\phi\lambda_B\lambda_C\rangle \tag{4.6}$$

where the integral is over the whole solid angle. Assuming that the particle A is in the initial state $|JM\rangle$, and that the transition is represented by the operator U, which is only assumed to be invariant under rotation, the transition amplitude for the final state $|p\theta\phi\lambda_B\lambda_C\rangle$ is

$$M = \langle p\theta\phi\lambda_B\lambda_C| U |JM\rangle . \tag{4.7}$$

Using the completeness of the $|pJM\lambda_B\lambda_C\rangle$ basis and eq. (4.6) one finds

$$M = \sqrt{\frac{2J+1}{4\pi}} D^{*J}_{M,\lambda_B-\lambda_C}(\phi, \theta, -\phi) H_{\lambda_B\lambda_C} \tag{4.8}$$

where

$$H_{\lambda_B\lambda_C} = \langle pJM\lambda_B\lambda_C| U |JM\rangle \tag{4.9}$$

are referred to as helicity amplitudes. These don't depend on the decay angles, which are the arguments of the D functions in eq. (4.8). When dealing with sequential two body decays, one can construct the coordinate systems in which the decay angles are expressed by applying subsequent Euler rotations with angles relative to the direction of the mother's momentum, and use eq. (4.8) recursively to calculate helicity amplitudes. Equation (4.8) can also be used to derive the angular distributions for the decay products. Note that the signal decay chain is a cascade of sequential two body decays, thus the helicity formalism is the best way to treat angular distributions in this case.

The amplitudes $H_{\lambda_B\lambda_C}$ can be calculated by projecting the invariant amplitudes on all the possible helicity eigenstates, which also are angular momentum eigenstates by construction.

As mentioned in section 4.1, the di-pion transition $\Upsilon(10860) \to h_b(2P)\pi^+\pi^-$ proceeds through the $Z_b(')$ intermediate resonances, so that the decay can be written as $\Upsilon(10860) \to Z_b(')^{\pm}\pi^{\mp} \to h_b(2P)\pi^+\pi^-$. Taking the $Z_b^{\pm}(10610) \to h_b(2P)\pi^{\pm}$ transition as example, and assuming this proceeds through pure P-wave coupling, the corresponding invariant amplitude is [70]

$$M = \epsilon_{\alpha\beta\gamma\delta}\, p^{\alpha}(h_b)p^{\beta}(\pi)\varepsilon^{*\gamma}(Z_b)\varepsilon^{\delta}(h_b) \tag{4.10}$$

where $\varepsilon^{\mu}(X)$ is the polarization four-vector of the particle X. In this case, the possible helicity configurations are ($\lambda_{Z_b} = 1$, $\lambda_{\pi} = 0$), ($\lambda_{Z_b} = 0$, $\lambda_{\pi} = 0$), and ($\lambda_{Z_b} = -1$, $\lambda_{\pi} = 0$). By replacing the polarization vectors with the helicity (and angular momentum) eigenstates, one can calculate the ratios $H_{+10} : H_{00} : H_{-10}$ and use them as parameters for the HELAMP model, thus simulating the correct angular distributions in the MC sample.

4.2 Data samples

All the selection criteria are optimized using MC simulation. In addition, control samples in the data are defined to cross check the selection efficiency and estimate the related systematic uncertainties. The signal region will not be explored until approval from the Belle review committee. This section contains the description of all the analyzed data and MC.

4.2.1 Data

The main experimental data sample consists of the 121.4 fb^{-1} collected on resonance at the $\Upsilon(10860)$ in experiments 43, 53, 67, 69 and 71. In addition, I use the $\Upsilon(3S)$ sample collected in experiment 49, consisting of 2.9 fb^{-1} on-resonance and 0.3 fb^{-1} off-resonance data for validation purposes. I estimate the number of produced $\Upsilon(3S)$ resonances by reconstructing $\Upsilon(3S) \to \pi^+\pi^-\Upsilon(1S) \to \pi^+\pi^-\mu^+\mu^-$ as reported in appendix A.2.

4.2.2 Signal MC

All the signal and control channel MC data are simulated using the `run_dependent_mc` package [71] provided by K. Chilikin, which allows to use the generators available in the Belle II software for generating Belle MC. Being run-dependent, the simulation includes the accelerator and detector conditions at each run of the experiment, giving the most realistic kinematics. The generation is accomplished with EvtGen [60] and the full simulation with GEANT-3 [63]. The EvtGen decay tables used for generation are reported in appendix A. The amplitude analysis of $\Upsilon(10860) \to h_b(2P)\pi^+\pi^-$ transitions reports the occurrence of peaking structures that are identified as the $Z_b(10610)^{\pm}$ and $Z_b(10650)^{\pm}$ bottomonium-like states [47]. Following the results of the analysis, which finds a non-resonant contribution compatible with zero, the $\Upsilon(10860) \to h_b(2P)\pi^+\pi^-$ transition is simulated assuming it proceeds exclusively through the production of the intermediate $Z_b^{(')}$ resonances. The $\Upsilon(10860) \to Z_b^{(')\pm}\pi^{\mp}$, $Z_b^{(')\pm} \to h_b(2P)\pi^{\mp}$, and $h_b(2P) \to \gamma\chi_{bJ}(1P)$ are simulated using the HELAMP model. The helicity amplitudes are calculated from the invariant amplitudes [39, 70] by projecting them on the possible helicity configurations as explained in section 4.1.1. Each amplitude is expressed by two numbers representing the real and the imaginary parts. The $\Upsilon(2S) \to \Upsilon(1S)\pi^+\pi^-$ is simulated using the VVPIPI model which correctly reproduces the di-pion invariant mass distribution. Radiative corrections are simulated for all the processes using the PHOTOS routine.

4.2.3 Generic MC

For the simulation of generic background channels I use the centrally-produced generic MC samples. They consist of various processes, which I group in classes for clarity:

- **Hadronic**. This group contains the `uds`, `charm`, `bsbs` and `nonbsbs`, samples, referring to the production of light hadrons, charmed hadrons, $B_s\overline{B}_s$ and $B\overline{B}$ pairs respectively. The `nonbsbs` sample contains also the $\Upsilon(10860) \to B\overline{B}\pi$ transitions, as well as di-pion and di-kaon transitions to lower $\Upsilon(nS)$ levels.

- **QED**. This group contains the 2-leptons, 4-leptons and 2-photon processes corresponding to the MC samples `eeee`, `eemm`, `mumu`, `tautau`, `eeuu`, `eess`, `eecc`.

As already mentioned, I use the Belle's data collected at the $\Upsilon(3S)$ resonance to study the control channel. At this energy region, the simulated hadronic transitions consist of the `uds` and `charm` samples, while the QED samples contain the same event types mentioned for the $\Upsilon(10860)$ dataset. At both energies the number of simulated events corresponds to six times the data for hadronic event types, and ten times the data for the other types. Some transitions that could constitute a source of background are missing from the Belle's inclusive MC. I simulate them separately and add them to the generic samples. First of all, events from $\Upsilon(10860) \to \Upsilon(2S)\eta$, with $\eta \to \gamma\gamma$ and $\Upsilon(2S) \to \Upsilon(1S)\pi^+\pi^-$, are a source of background. Another possible background is due to the transitions $\Upsilon(10860) \to \chi_{b1,2}(1P)\pi^+\pi^-\pi^0$ which can proceed directly or through the intermediate ω resonance. The branching fraction for these processes were measured by Belle [72, 73], and are reported on the PDG listings in the case of $\Upsilon(10860) \to \chi_{b1,2}(1P)\pi^+\pi^-\pi^0$ transitions. The number of generated events corresponds to six times the luminosity as for the already existing hadronic samples.

4.2.4 Definition of variables

The event selection is cut based, meaning that the values of chosen variables are restricted to lie in definite regions. In this section I give the definition of the observables used for the selection.

- Kinematics
  The recoil mass of a system X coming from a $A \to B + X$ transition is the invariant mass of the B system. If the B particle does not interact with the detector, typically because the mean lifetime is too short, its mass can be

measured by using the four-momenta of A and X. Exploiting relativistic kinematics, the variable is defined as $M_{recoil}(X) = \sqrt{(p_A - p_X)^2} = M_B$, where p denotes the four-momentum in the center of mass reference frame.

- PID

  Based on the considerations described in section 3.4.2, the electron likelihood ratio is defined as

$$e_{ID} = \frac{\Pi_{i=1}^{n}\mathcal{L}_e(i)}{\Pi_{i=1}^{n}\mathcal{L}_e(i) + \Pi_{i=1}^{n}\mathcal{L}_{\bar{e}}(i)} \tag{4.11}$$

  where i runs over all the discrimination variables.

  The muon likelihood μ_{ID} is built as described in section 3.4.2, and is defined as

$$\mu_{ID} = \frac{\mathcal{L}_\mu}{\mathcal{L}_\mu + \mathcal{L}_\pi + \mathcal{L}_K}. \tag{4.12}$$

4.3 Event topology and signal region definition

In this section I report the features of correctly reconstructed signal events, obtained after running the reconstruction on signal MC with basic quality cuts. In order to get the distributions of kinematical variables in signal events, the MC truth is used to identify the tracks and the photons.

The intent is to give information about the event topology to better understand the description of the selection criteria. I weight the simulated events by assuming that $\mathcal{B}[h_b(2P) \to \chi_{b2}(1P)\gamma] = 5\%$, that the ratios between the three channels are as predicted by the coupled-channel theory [39] and by taking the PDG values for $\mathcal{B}[\Upsilon(10860) \to h_b(2P)\pi^+\pi^-]$, $\mathcal{B}[\chi_{bJ}(1P) \to \gamma\Upsilon(1S)]$ and $\mathcal{B}[\Upsilon(1S) \to \mu^+\mu^-]$, which are reported in table 4.1. The integrated luminosity is also taken into account.

The quality cuts are reported as follows. I apply a cut on the minimum photon energy in order to reduce the background coming from the beam and from Final State Radiation (FSR). I select charged tracks coming from the interaction region because they are produced by short-lived and heavy resonances. For pions, I ask the transverse momentum p_T to be higher than 50 MeV/c in order to exclude curlers. Muons are expected to carry a high momentum since they are produced in the annihilation of the $\Upsilon(1S)$ resonance. Consequently, I select muons with $p > 2\ GeV/c$. Summarizing, the following cuts are applied:

- Photons:
  $E(\gamma) > 100\ MeV$

- Tracks:
  $dr < 1\ cm$
  $|dz| < 3\ cm$
  $p(\mu^\pm) > 2\ GeV/c$
  $p_T(\pi^\pm) > 50\ MeV/c$.

Due to the choice of the decay chain, there are two photons in the cascade. The photon radiated by $h_b(2P)$ is labeled as γ_1, while that radiated by $\chi_{bJ}(1P)$ is labeled as γ_2. The photon energy distributions, measured in both the laboratory and the center-of-mass reference frame, are shown in figures 4.2a and 4.2b. Due to the Lorentz boost, the distributions are overlapping in the laboratory frame. On the contrary, in the center of mass frame they are well separated.

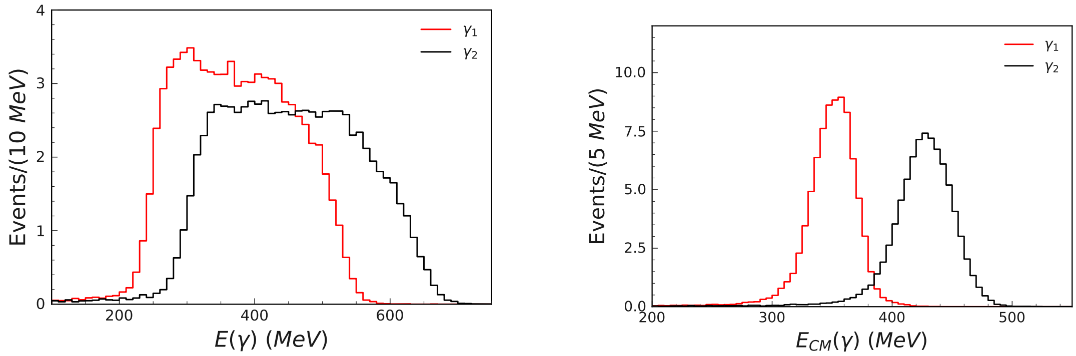

(a) (b)

Figure 4.2: Gamma energy distributions in the laboratory (a) and in the center-of-mass (b) reference frames for signal events.

The pion total momentum p and transverse momentum p_T distributions are shown in fig. 4.3a – 4.3b. The peaked distribution of $p_T(\pi)$ is due to the production of the $Z_b^{(\prime)}$ intermediate resonances. As expected, pions have low momentum.

The di-pion recoil mass distribution $M_{recoil}(\pi^+\pi^-)$, shown in fig. 4.4, is strongly peaking around $M(h_b(2P)) = 10.26\ GeV$. The distribution is narrow, with the standard deviation being $\sigma = 6.7\ MeV$, but exhibits non-gaussian tails. The reason for the presence of the tails is the momentum resolution of pions, that is worsened because they have low momentum. The $M_{recoil}(\pi^+\pi^-)$ variable is used to define the signal and sideband regions, as explained in section 4.4.2.

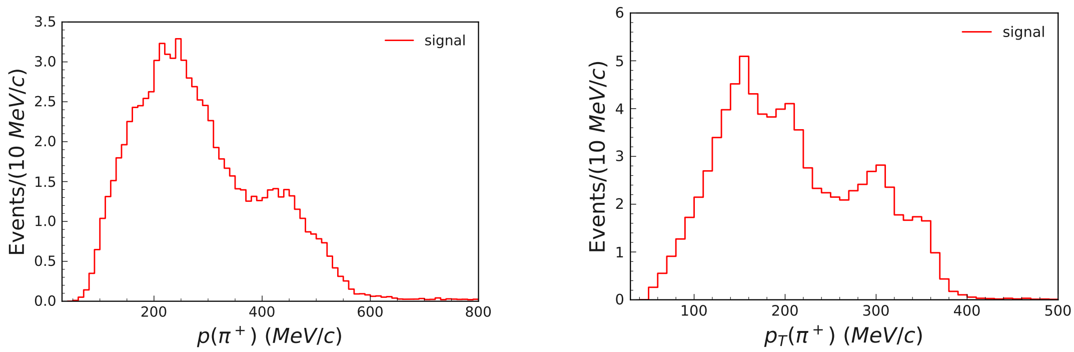

(a) (b)

Figure 4.3: Distribution of the pion momentum (a) and transverse momentum (b) for signal events. The distributions for pions of opposite charge are identical.

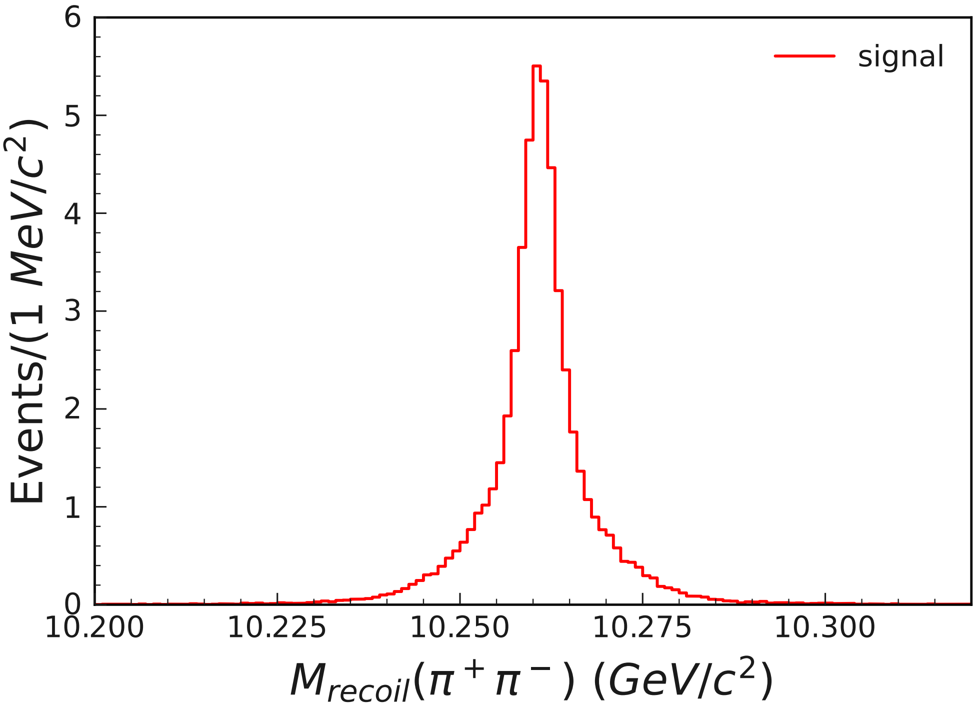

Figure 4.4: Di-pion recoil mass distribution for signal events.

Muons instead have high momentum. The di-muon invariant mass $M(\mu\mu)$ peaks around $M(\Upsilon(1S))$ as expected. The two distributions are shown in figs. 4.5a–4.5b.

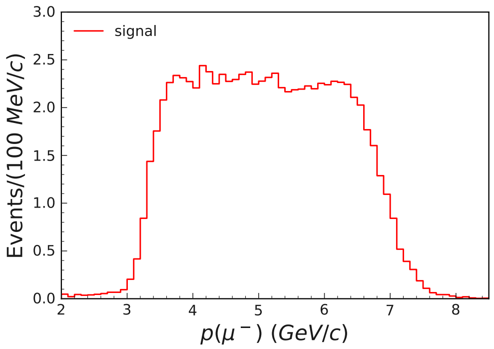

(a)

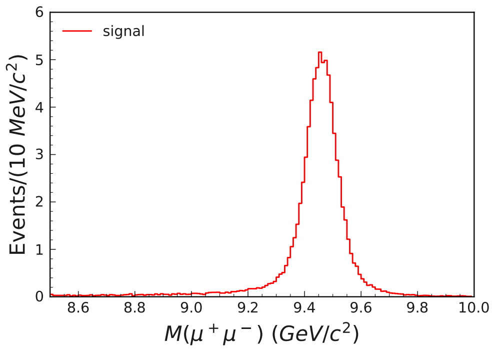

(b)

Figure 4.5: Distribution of muon's momentum (a) and di-muon invariant mass (b) for signal events.

The difference $M(\mu\mu\gamma\gamma) - M(\mu\mu)$ is used as the fit variable for determining the signal yield. The variable corresponds to the difference $M(h_b(2P)) - M(\Upsilon(1S))$ for signal events. I use this variable because it gives information on the $h_b(2P)$ yield based on the final state particles coming from the $h_b(2P) \to \gamma\chi_{bJ}(1P) \to \gamma\gamma\Upsilon(1S) \to \gamma\gamma\mu^+\mu^-$ cascades. Subtracting the di-muon invariant mass from $M(\mu\mu\gamma\gamma)$ makes the variable uncorrelated with $M(\mu\mu)$. The distribution of the fit variable is shown in fig. 4.6a. While this variable is not affected by the $\chi_{bJ}(1P)$ channel, it is possible to see the contribution of the three channels in the distribution of the $M(\mu\mu\gamma_2) - M(\mu\mu)$ variable, shown in fig. 4.6b. Note that the contribution of the $h_b(2P) \to \chi_{b0}(1P)\gamma$ channel is negligible.

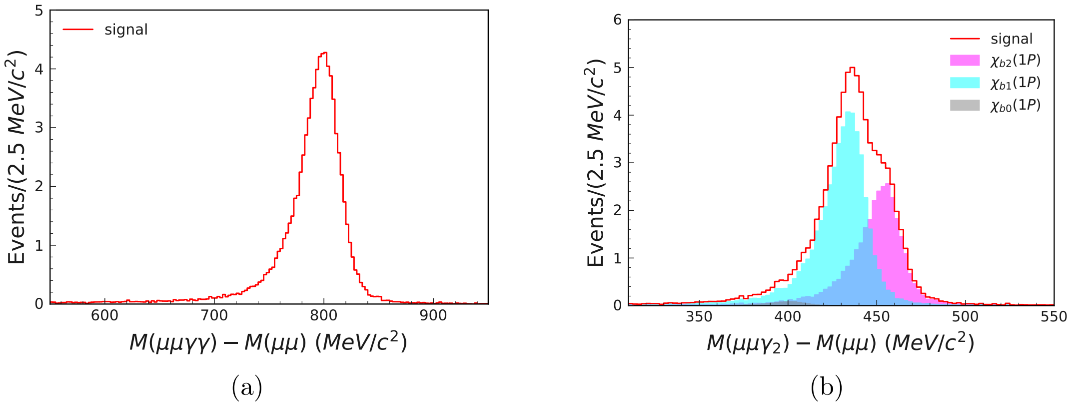

Figure 4.6: Distribution of the fit variable (a) and the variable showing the contributions from the different channels (b).

Without further cuts on the photons, the reconstruction algorithm double counts each signal event. To solve this problem it is necessary to distinguish the two photons. Based on the separation between the distributions of $E_{CM}(\gamma)$, I exploit the variable $\Delta E_{CM}(\gamma) = E_{CM}(\gamma_2) - E_{CM}(\gamma_1)$ in order to do this. The distributions of $E_{CM}(\gamma_{1,2})$ are partially overlapping, so that $E_{CM}(\gamma_1) > E_{CM}(\gamma_2)$ 20% of the times. However, the reconstruction double counts each signal event, and the fit variable is not affected when selecting the wrong combination, as can be seen in fig. 4.7.

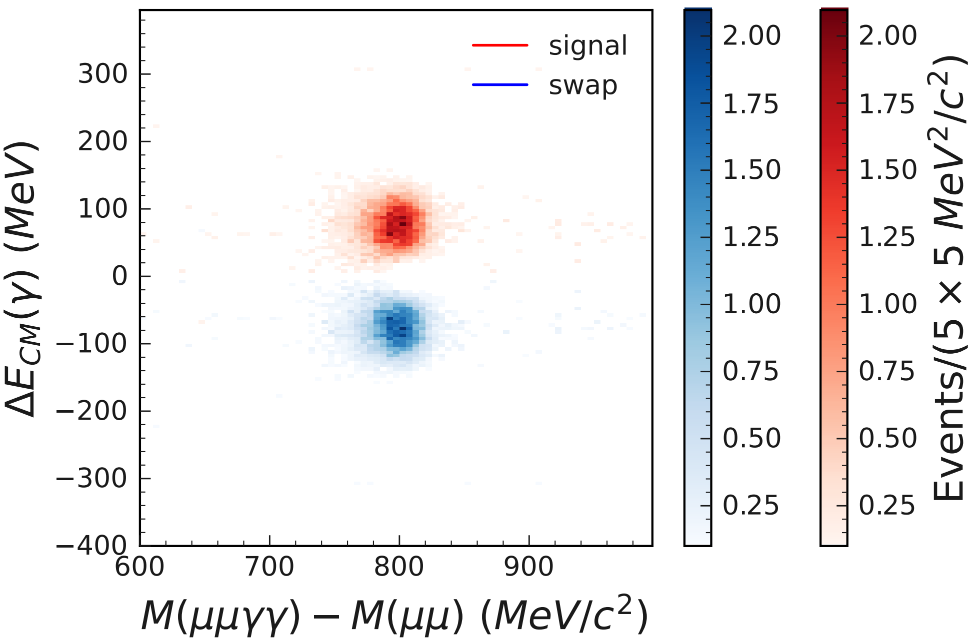

Figure 4.7: Two-dimensional histogram showing the correlation between the fit variable and $\Delta E_{CM}(\gamma)$ for true and swap γ combinations in signal events.

4.4 Event selection

Since the data samples are very large, it is necessary to reduce the amount of data before further studies, in order to speed up the analysis. First I define a rough selection aimed to select a subsample of data and MC (skim). On top of the skimming selection I then define further cuts to suppress the residual backgrounds. The skim selection is not optimized for signal significance but it's designed to retain the events of interest with high efficiency. The further selection criteria, on the other hand, are chosen to maximize the figure of merit $FoM = \frac{\sqrt{S}}{\sqrt{S+B}}$, where S and B are the signal and background fraction surviving the selection.

4.4.1 Skimming and background identification

The data reduction is obtained after applying a loose event selection to all the available data at $\Upsilon(10860)$. The skimmed data is stored into mDST (mini-DST) files for further analysis. Any further analysis on MC and data samples will thus be performed with these summary tables as input in order to save memory and CPU time.

The skim cuts are listed as follows:

- Tracks:
  $17° < \theta < 150°$, corresponding to the CDC acceptance
  More than 20 hits in the CDC
  $dr < 1\ cm$
  $|dz| < 3\ cm$

- Photons:
  $E(\gamma) > 60\ MeV$

- Muons:
  $3\ GeV/c < p(\mu^{\pm}) < 10\ GeV/c$
  $9.0\ GeV/c^2 < M(\mu^+\mu^-) < 9.8\ GeV/c^2$

- Pions:
  $p_T(\pi^{\pm}) > 50\ MeV/c$
  $p(\pi^{\pm}) < 2\ GeV/c$

- Event level:
  I ask for exactly one candidate for each of the four tracks emitted in the decay chain, that is $n(\pi^+) = n(\pi^-) = n(\mu^+) = n(\mu^-) = 1$

The cut on photon energy is kept very loose so that the skimmed samples also include events with other transitions, where radiated photons may be softer compared to those of the signal channels. These can be used for validation purposes. I perform a first analysis of the skimmed sample, by looking at the PDG codes of the detected particles and of their (grand)mothers after MC matching, in order to identify the most important background sources. In the analysis, candidates from generic MC are weighted according to the integrated luminosity, while those from signal MC are weighted as described earlier in section 4.3.

The most relevant background in the skimmed sample comes from the $e^+e^- \to \mu^+\mu^-(\gamma)$ process. In this case, reconstructed $\pi^{\pm}$ are actually $e^{\pm}$ produced by photons that interact with the detector material giving rise to pair production (converted photons). The photon candidates come from beam background and/or from $e^{\pm}$ bremsstrahlung. The beam background consists of $e^{\pm}$ scattered by the residual gas contained in the beam pipe (beam-gas scattering), or $e^{\pm}$ deviated The main features of this background are that particles reconstructed as pions have a high e_{ID} likelihood and a low opening angle in the lab reference frame, while photons are generally soft and the di-muon invariant mass is not peaking. The process $e^+e^- \to \pi^+\pi^-\mu^+\mu^-(\gamma)$ gives the second most important background, although it is easily reduced by cutting on the photon energy.

The main hadronic background consists of $\Upsilon(10860) \to \Upsilon(2S)\pi^0\pi^0$ and $\Upsilon(10860) \to \Upsilon(2S)\eta$ transitions because of the subsequent 2γ decays of π^0 and η, in combination with the di-pion transitions $\Upsilon(2S) \to \Upsilon(1S)\pi^+\pi^-$. The topology of these event types is similar to that of the signal channel, but in the case of $\pi^0\pi^0$ transitions two extra photons are not reconstructed. Their possible combinations, however, determine the creation of many candidates since the number of photons in the event is not limited by the selection. The $\Upsilon(10860) \to \chi_{b1,2}\pi^+\pi^-\pi^0$ transitions give a smooth background in the $M_{recoil}(\pi^+\pi^-)$ spectrum, contrarily to the other hadronic event types.

The distributions of several variables after the skim selection are shown in fig. 4.8a-4.8f.

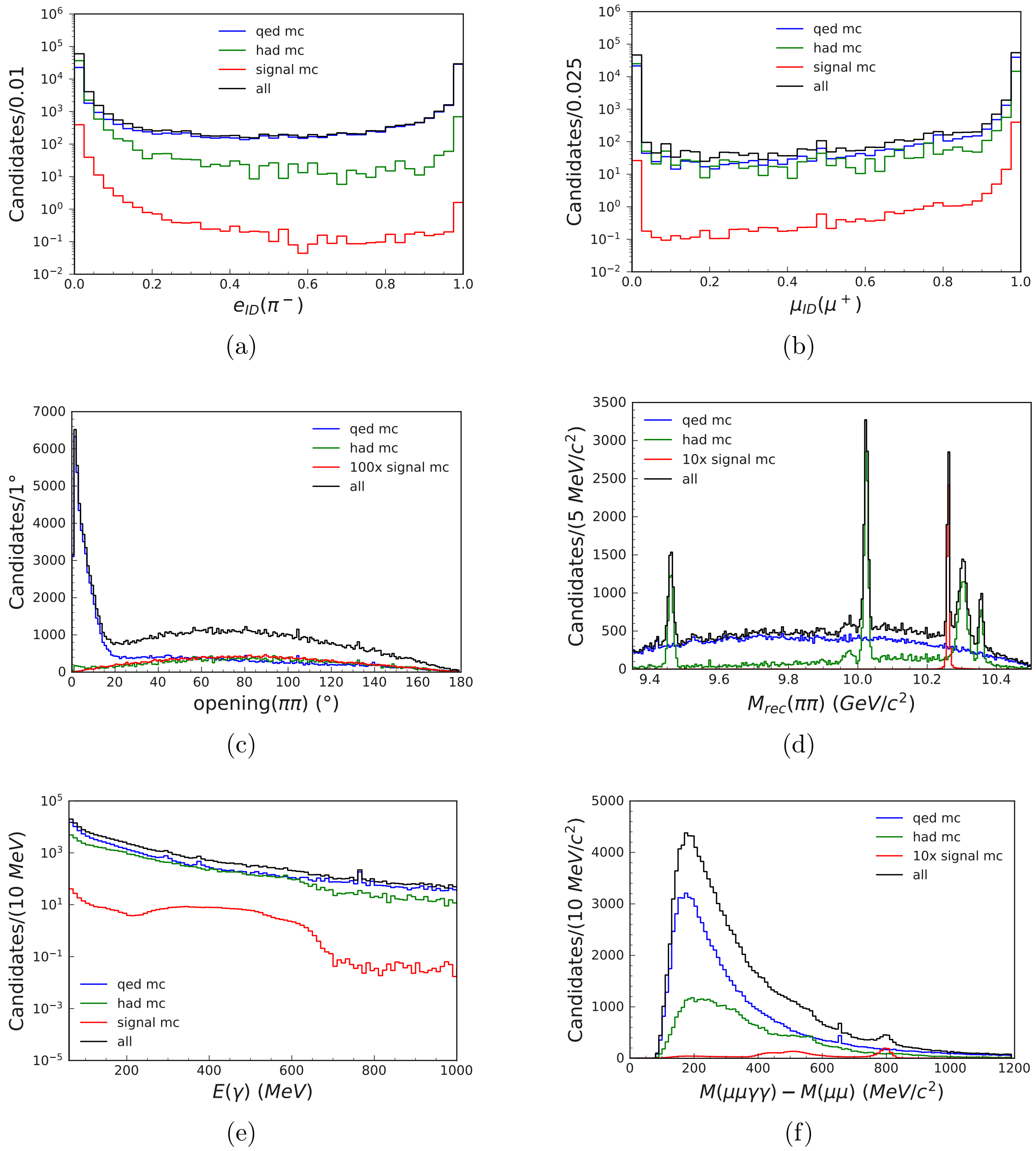

Figure 4.8: Distributions of variables of interest after skim cuts.

4.4.2 Further selections

After the identification of the most relevant background sources, cuts are applied subsequently for a tighter selection. The cuts are listed as follows.

- Well identified $e^{\pm}$ are removed by asking $e_{ID}(\pi^{\pm}) < 0.4$ in order to reduce QED background. The cut point is not otpimized but chosen according to the guidelines provided by the Belle leptonID group. This cut allows us to remove most of the photon conversions which could be misidentified as π candidates. The cut is shown in figure 4.9a.
- Following the same guidelines, I select the muons from the high momentum tracks having $\mu_{ID}(\mu^{\pm}) > 0.8$. The cut is shown in figure 4.9b.

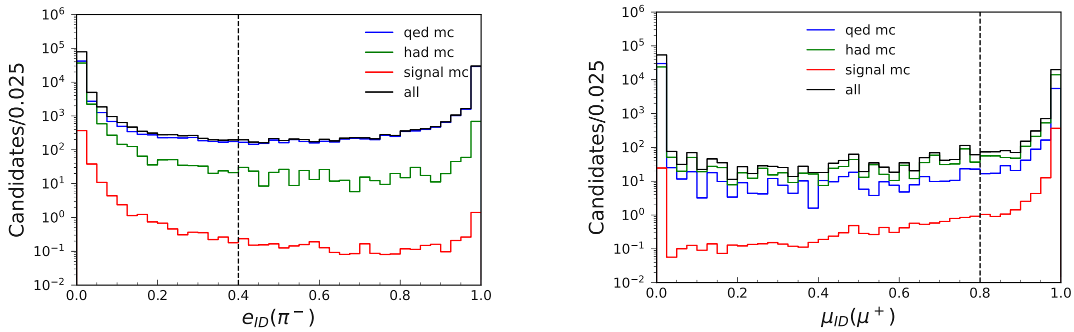

(a) (b)

Figure 4.9: Cut on PID variables: $e_{ID}(\pi)$ (a) and $\mu_{ID}(\mu)$ (b).

- For photons, I ask $E(\gamma) > 264\ MeV$ in order to reduce beam and FSR backgrounds. The cut is optimized as described above. The optimization procedure is performed with step 1 MeV and shown in fig. 4.10b. A further reduction of background photons is obtained by asking $200\ MeV < E_{CM}(\gamma) < 600\ MeV$. This cut is not optimized because the $E_{CM}(\gamma)$ variable is correlated with the fit variable and the optimization would concentrate all the residual background in the same region containing the signal distribution. This cut is shown in figure 4.11.

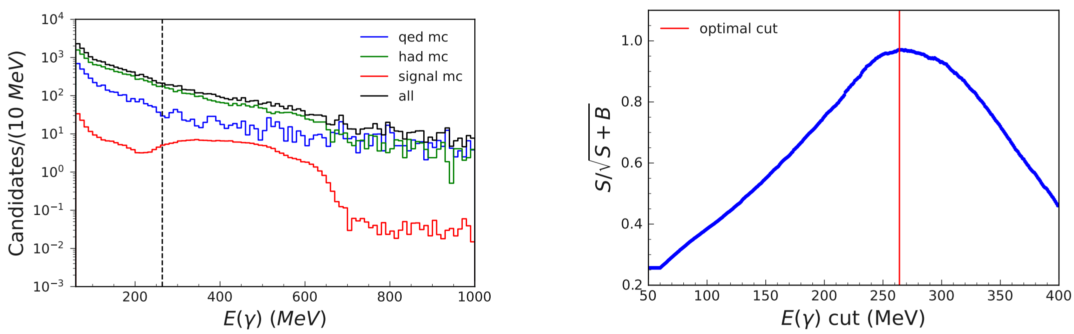

(a) (b)

Figure 4.10: Cut on photon energy (a) and the corresponding FoM optimization (b).

- I reduce the residual background from electrons and positrons misidentified as pions by asking the opening angle bewteen the pions to be greater than 11.1° in the laboratory frame. This cut is optimized as described above with step 0.1°. A plot illustrating the cut and the relative optimization procedure is shown in fig. 4.12.

- I apply a simple π^0 veto: events with one or more candidates satisfying $|M(\gamma\gamma) - m(\pi^0)| < 20\ MeV$, where $m(\pi^0)$ is the nominal π^0 mass, are discarded. This veto is also optimized by the same method described above with step 1 MeV/c^2. Figure 4.13 shows the selection in the $M(\gamma\gamma)$ distribution and the corresponding FoM optimization.

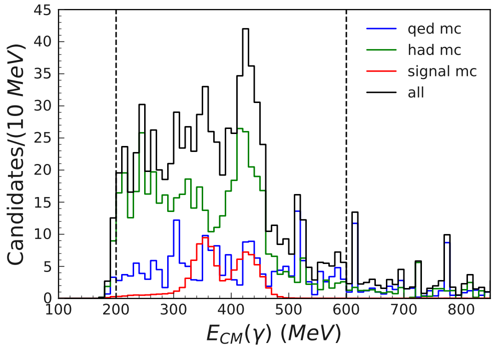

Figure 4.11: Cut con $E_{CM}(\gamma)$

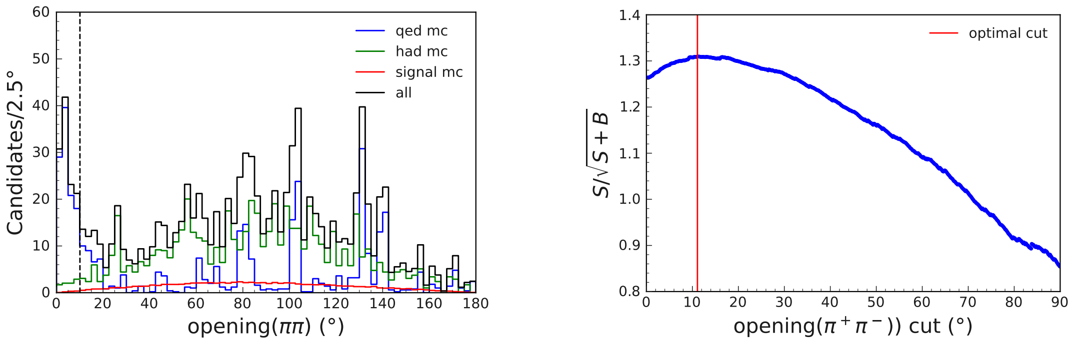

(a) (b)

Figure 4.12: Cut on opening($\pi^+\pi^-$) (a) and the corresponding FoM optimization (b).

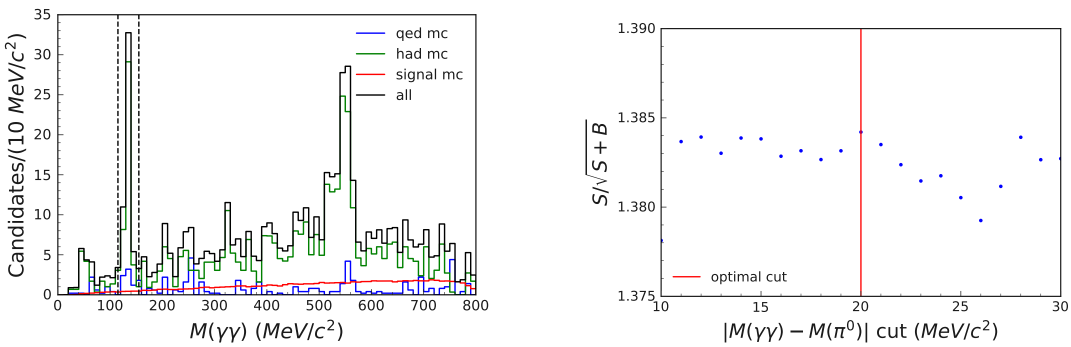

(a) (b)

Figure 4.13: π^0 veto. Events with one or more candidates whose $M(\gamma\gamma)$ lies inside the region delimited by dashed lines are discarded.

- After the selections mentioned above I still observe events with more than one candidate in the MC samples.

  I reduce the number of candidates by asking $E_{CM}(\gamma_2) > E_{CM}(\gamma_1)$. This allows to select the candidate with the correct labels for the photons. Due to the double counting in reconstruction, symmetrical with respect to γ_1 and γ_2, this cut has 100% efficiency by construction, as can be seen in figure

4.14.

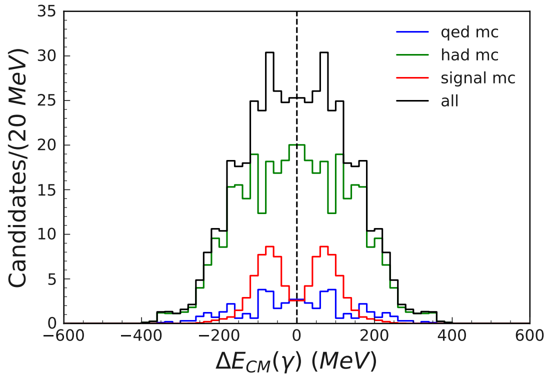

Figure 4.14: Cut on $\Delta E_{CM}(\gamma)$.

- I apply a four-constraints (4C) kinematic fit, constraining the total four-momentum of final state particles to the beams four-momentum, without updating the measured daughter kinematic variables with the fitted values. When more than one candidate is found, the candidate with the highest fit p-value is chosen. The principles of kinematic fitting are described in appendix A.3. The library used for the fit is OrcaKinFit, which is based on the MarlinKinfit library [74] used in the ILC project. The numerical optimization is performed with the Newton method. Moreover, I cut on the kinematic fit p-value (p-value $> 10^{-6}$) to reject bad quality fits.

The fit variable after these cuts is shown in fig. 4.15a. It can be seen that the hadronic background peaks close to the signal. Fortunately, the $M_{recoil}(\pi^+\pi^-)$ variable can be exploited to both reduce this background and define the signal and sideband regions. Its distribution is shown in fig. 4.15b.

The remaining hadronic background is due to $\Upsilon(2S) \to \Upsilon(1S)\pi^+\pi^-$ transitions, where $\Upsilon(2S)$ is produced via $\Upsilon(10860) \to \Upsilon(2S)\eta$ and $\Upsilon(10860) \to \Upsilon(2S)\pi^0\pi^0$ transitions.

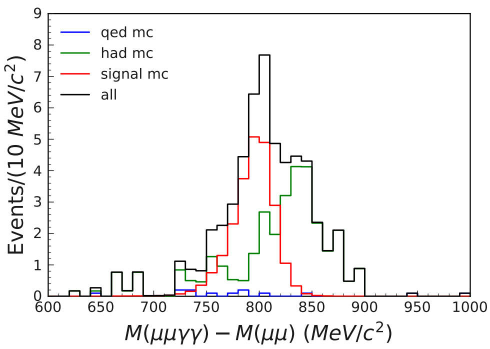

(a)

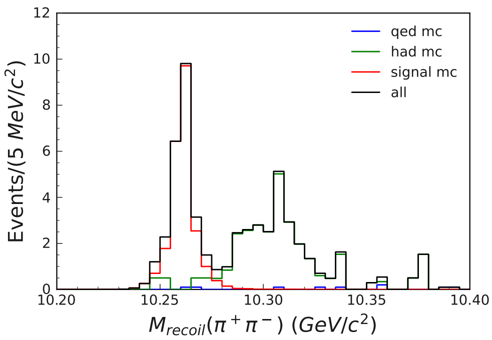

(b)

Figure 4.15: Distribution of the fit variable (a) and of the $M_{recoil}(\pi^+\pi^-)$ variable (b) after the selection described in section 4.4.2.

The selection efficiency is estimated in the next section, which also contains the definition of the signal and sideband regions.

4.4.3 Definition of the signal and sideband regions and efficiency estimation

I define the signal region as the $10.240\ GeV/c^2 < M_{recoil}(\pi^+\pi^-) < 10.275\ GeV/c^2$ interval, corresponding to $(-3\sigma, +2\sigma)$ for signal events. The choice of 2σ for the right side of the interval is done in order to exclude the $\Upsilon(2S) \to \Upsilon(1S)\pi^+\pi^-$ background from the signal region while slightly reducing the efficiency. In addition, three sideband regions are defined:

- SB 0: $10.000\ GeV/c^2 < M_{recoil}(\pi^+\pi^-) < 10.130\ GeV/c^2$
- SB 1: $10.190\ GeV/c^2 < M_{recoil}(\pi^+\pi^-) < 10.240\ GeV/c^2$
- SB 2: $10.275\ GeV/c^2 < M_{recoil}(\pi^+\pi^-) < 10.500\ GeV/c^2$

The region $10.13\ GeV/c^2 < M_{recoil}(\pi^+\pi^-) < 10.19\ GeV/c^2$ is blinded, as for the signal region, because of the ongoing search for the $\Upsilon(10860) \to \Upsilon_J(1D)\pi^+\pi^- \to \gamma\chi_{bJ}(1P)\pi^+\pi^- \to \gamma\gamma\Upsilon(1S)\pi^+\pi^-$ cascades. A graphical illustration of the regions is shown in figure 4.16. In the figure, the signal region is the interval delimited by red dashed lines. Sidebands are denoted by the corresponding text, while the blue dashed lines denote the other blinded region.

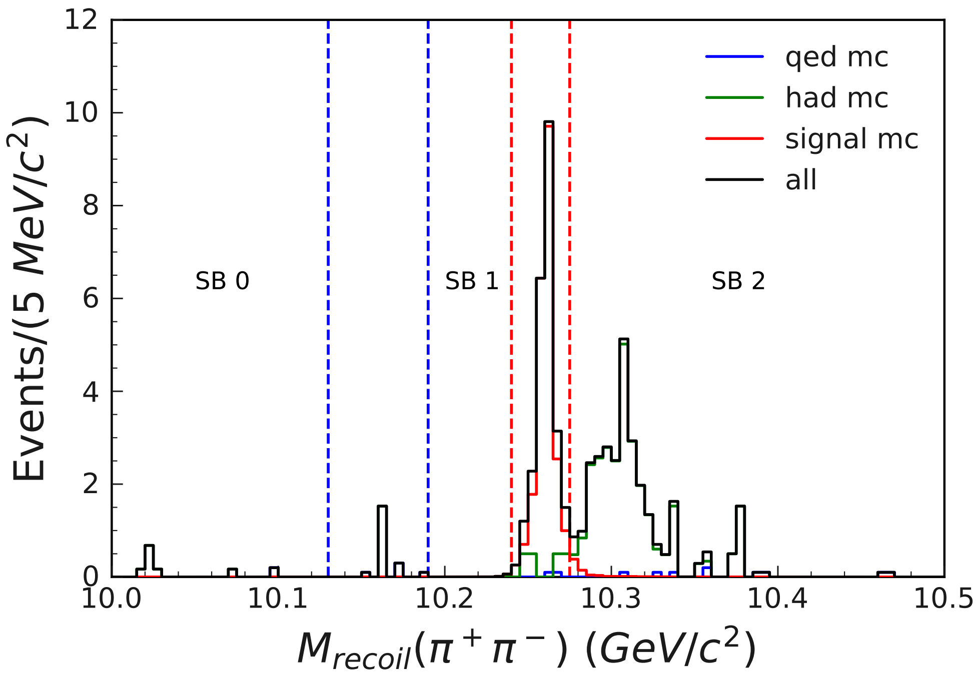

Figure 4.16: Distribution of the di-pion recoil mass variable for MC, showing signal and sideband regions.

The distribution of the fit variable for events lying in the signal region is shown in fig. 4.17. The sidebands are exploited for validation purposes as described in section 4.5.2.

The selection efficiency, defined as the ratio between the signal events surviving the selection and the number of generated events, are determined from MC matching for each channel and reported in table 4.2.

Table 4.2: Selection efficiencies of each investigated channel after the signal region cut. The uncertainty is determined assuming a binomial distribution.

Channel	Selection efficiency (%)
$h_b(2P) \to \chi_{b2}(1P)\gamma$	11.6 ± 0.1
$h_b(2P) \to \chi_{b1}(1P)\gamma$	12.0 ± 0.1
$h_b(2P) \to \chi_{b0}(1P)\gamma$	13.2 ± 0.1

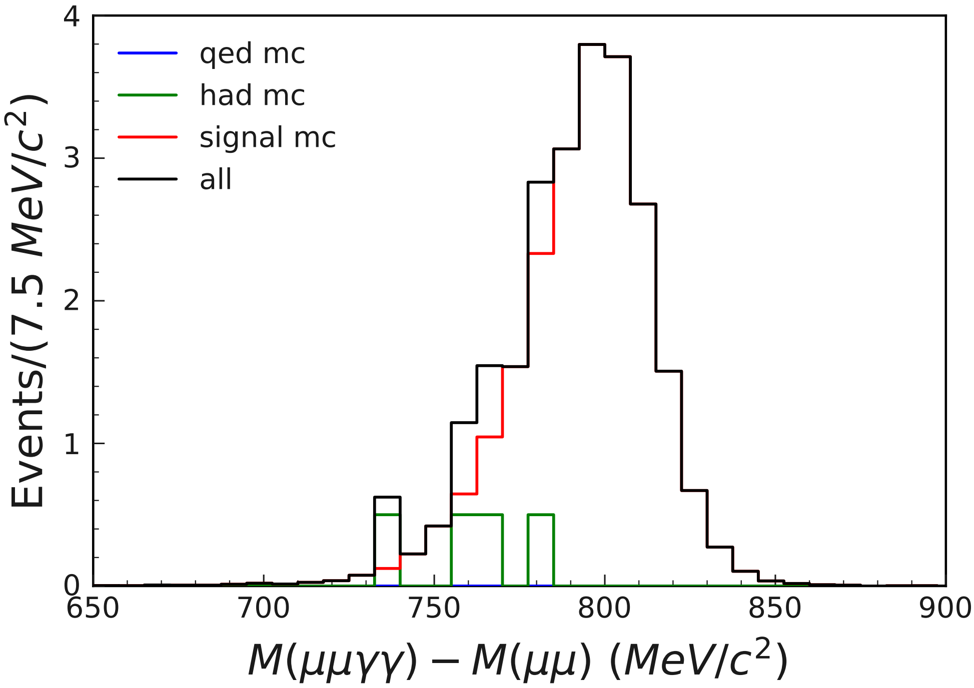

Figure 4.17: Distribution of the fit variable for events in the signal region.

4.5 Validation

I choose processes with a similar topology and known cross sections in order to validate the event selection and cross-check the efficiency estimation at a different energy region. A first validation is thus done on the $\Upsilon(3S)$ dataset, introduced in section 4.2.1. The procedure is described in section 4.5.1.

To perform a second validation I exploit the $M_{recoil}(\pi^+\pi^-)$ sidebands at the $\Upsilon(10860)$ energy region, defined in section 4.4.3. This validation procedure is described in section 4.5.2.

4.5.1 Control channel

I use the cascades

$$\Upsilon(3S) \to \gamma\chi_{bJ}(2P) \to \gamma\gamma\Upsilon(2S) \to \gamma\gamma\pi^+\pi^-\Upsilon(1S) \to \gamma\gamma\pi^+\pi^-\mu^+\mu^- \quad (4.13)$$

as control channels at the $\Upsilon(3S)$ energy region. A diagram of the cascade decays is shown in fig. 4.18. Concerning the event topology, the main difference with

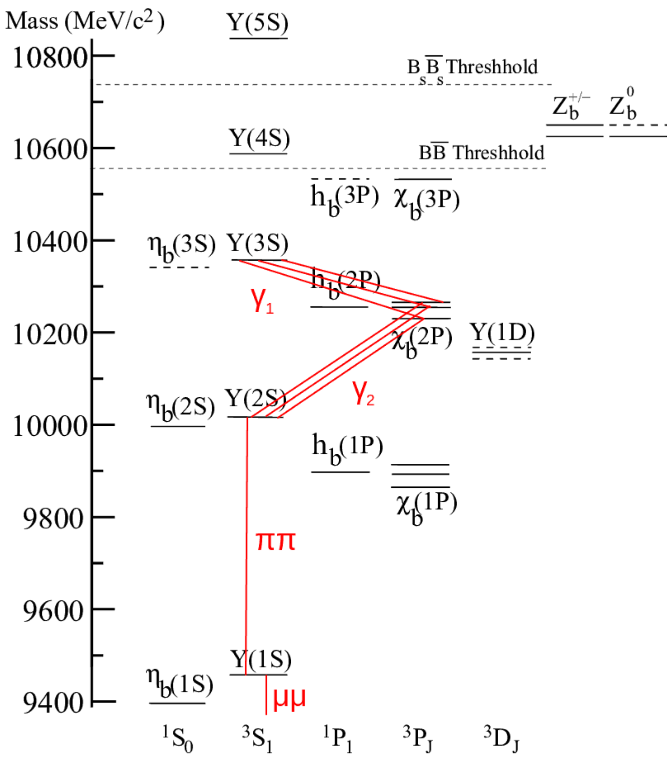

Figure 4.18: Diagrams of the control decay chain used to cross check the reconstruction efficiency measured on the MC sample.

respect to the signal channels is that radiated photons are softer, but their energy is of the same order of magnitude ($\sim 100\ MeV$). The di-pion transition $\Upsilon(2S) \to \pi^+\pi^-\Upsilon(1S)$ ensures that pions have low momentum as for the signal cascade.

Table 4.3: Branching fractions reported by PDG for the processes involved in the control channel.

Process	**BF (%)**
$\Upsilon(3S) \to \chi_{b2}(2P)\gamma$	13.1 ± 1.6
$\Upsilon(3S) \to \chi_{b1}(2P)\gamma$	12.6 ± 1.2
$\Upsilon(3S) \to \chi_{b0}(2P)\gamma$	5.9 ± 0.6
$\chi_{b2}(2P) \to \Upsilon(2S)\gamma$	8.9 ± 1.2
$\chi_{b1}(2P) \to \Upsilon(2S)\gamma$	18.1 ± 1.9
$\chi_{b0}(2P) \to \Upsilon(2S)\gamma$	1.28 ± 0.30
$\Upsilon(2S) \to \Upsilon(1S)\pi^+\pi^-$	17.85 ± 0.26

The branching fractions of the processes involved in the cascade are taken from PDG and reported in table 4.3. They are used to weight MC events and the respective errors are propagated as contributions to the uncertainties on counts obtained after the event selection. Based on the measured number of produced $\Upsilon(3S)$, reported in appendix A.2, on the reported BFs, and expecting the selection efficiencies to be of order 10% as for signal MC, the expected number of events is around 250.

The tools used for the simulation of these processes are the same used for signal MC. I report the EvtGen tables used for the generation in appendix A.

Event selection

The event selection for the control processes (4.13) is very similar to that used for the signal channels. Here are listed the different cuts only, the others being unchanged.

- Photons:
  $E(\gamma) > 60\ MeV$
  $80 < E_{CM}(\gamma_1) < 150\ MeV$
  $160 < E_{CM}(\gamma_2) < 280\ MeV$
- Di-pion:
  $9.770 < M_{recoil}(\pi\pi) < 9.810\ GeV/c^2$

Again, a 4C kinematic fit is performed in order to select the best candidate based on the fit p-value and to further cut off the background. The cut on $M_{recoil}(\pi^+\pi^-)$ excludes the $\Upsilon(3S) \to \Upsilon(1S)\pi^+\pi^-$ transitions and mimics the cut applied to $\Upsilon(10860)$ data when defining the signal region. In the control channel the di-pion recoil mass is centered on a value that does not correspond to any existing particle because the $\Upsilon(2S)$ is boosted with respect to the produced $\Upsilon(3S)$.

The selection efficiencies determined from MC matching are reported in table 4.4 for each channel.

Table 4.4: Selection efficiency for the three control channels.

Channel	**Selection efficiency (%)**
$\Upsilon(3S) \to \gamma\chi_{b2}(2P)$	13.1 ± 0.1
$\Upsilon(3S) \to \gamma\chi_{b1}(2P)$	14.0 ± 0.1
$\Upsilon(3S) \to \gamma\chi_{b0}(2P)$	13.7 ± 0.1

Systematic uncertainties

I evaluate the systematic uncertainty relative to the event selection evaluating the ratio between the integrals of the data and MC distributions (N_{data} and N_{MC} respectively) for the variable $M(\mu\mu\pi\pi\gamma_2) - M(\mu\mu)$, whose distribution is shown in fig. 4.19. The accordance between the two distributions is represented by using the pull variable, which in the case of data/MC comparison is defined as

$$pull_i = \frac{N_{i,data} - N_{i,MC}}{\sqrt{\sigma^2_{i,data} + \sigma^2_{i,MC}}} \tag{4.14}$$

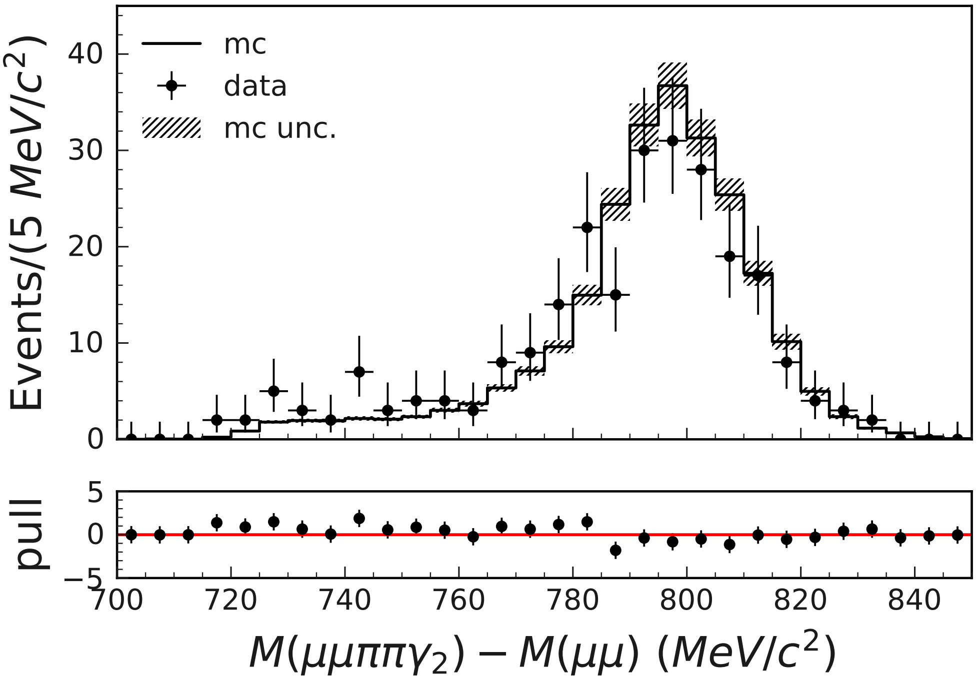

Figure 4.19: Data/MC comparison for the $M(\mu\mu\pi\pi\gamma_2)$ variable for selected events at the $\Upsilon(3S)$ control region.

for the i-th bin, where $\sigma_{i,data}$ ($\sigma_{i,MC}$) are the uncertainties of the data (MC) counts and $N_{i,data}$ ($N_{i,MC}$) the corresponding counts. With this definition, the pull corresponds to the difference between data and MC counts, weighted by the propagated uncertainty. The uncertainties on bin counts correspond to the Poisson 68% confidence intervals and are thus asymmetric, hence if $N_{i,data} > N_{i,MC}$ the upper (lower) uncertainty on MC (data) bin counts is taken and vice-versa.

The uncertainty on the N_{data}/N_{MC} ratio represents the relative systematic uncertainty on the selection efficiency. Again, the Poisson 68% confidence intervals are used to compute the uncertainty for counted events. The results are:

- $N_{data} = 245^{+17}_{-16}$
- $N_{MC} = 244 \pm 5$
- $N_{data}/N_{MC} = 1.00^{+0.09}_{-0.07}$

From this ratio I estimate an overall $+9\%-7\%$ uncertainty on the efficiency estimation after the event selection, with no corrections to be applied. The data/MC comparison is also shown for other variables, specifically for the variables used in the event selection, in figure 4.20.

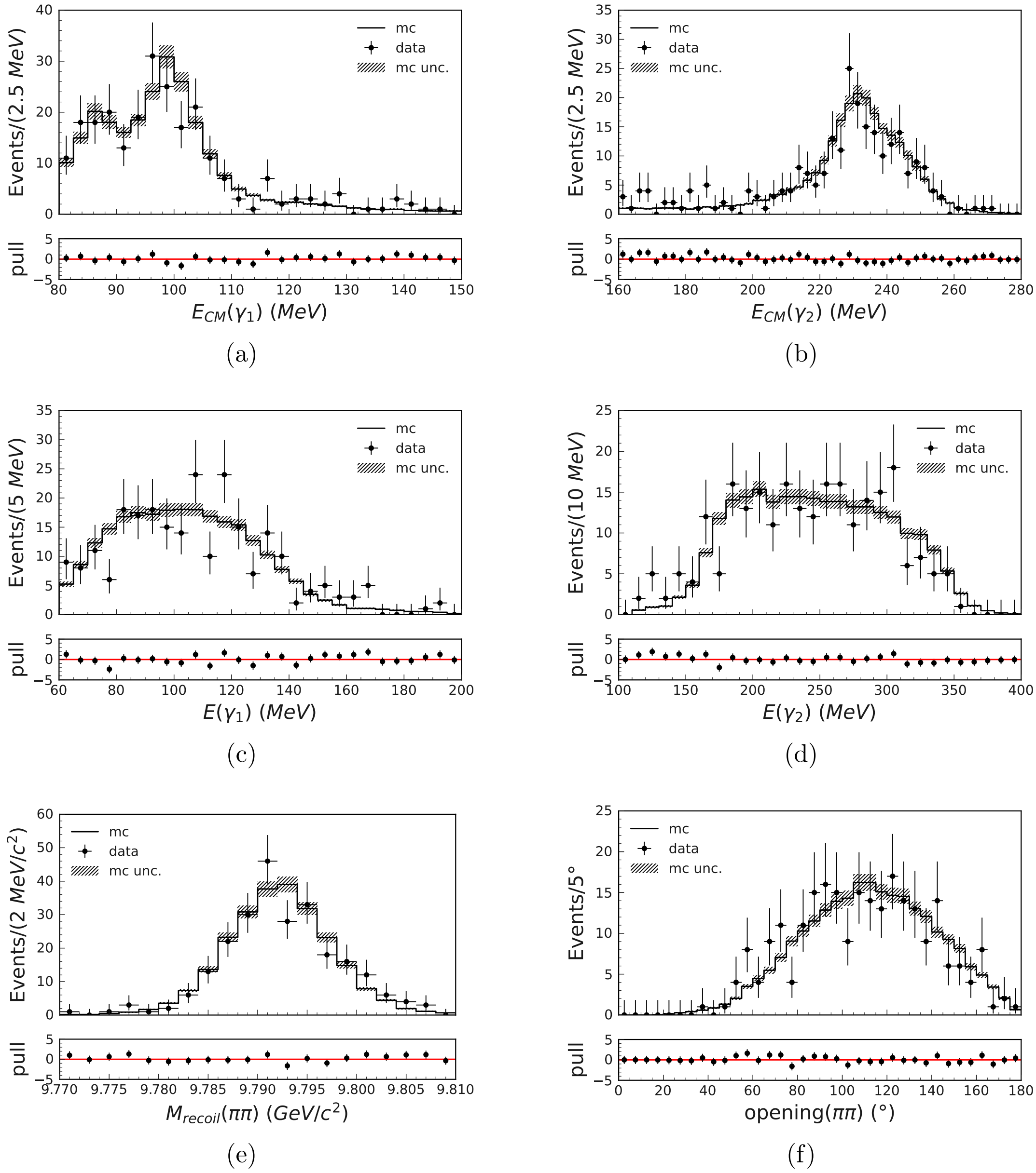

(a) (b) (c) (d) (e) (f)

Figure 4.20: Distribution of the variables used for the event selection for the $\Upsilon(3S)$ control channel.

4.5.2 Sideband regions

At the $\Upsilon(10860)$ energy region, I measure the number of events from data and MC in the sideband regions of the $M_{recoil}(\pi^+\pi^-)$ variable. This is done in order to estimate the systematic uncertainty related to background counts. Indeed, the background estimation for a Poisson random variable is fundamental in order to get the expected upper limits, or in general the confidence intervals for the signal branching fractions.

I report the measured number of events on MC (N_{MC}) and real data (N_{data}) in table 4.5, alongside with their ratio for each sideband. The measurements are found to be compatible within the uncertainties in each region. Using the results from the combined sidebands, I find that MC correctly describes the background within a $^{+27\%}_{-22\%}$ uncertainty. This value corresponds to the systematic uncertainty on background counts.

Table 4.5: Comparison between counted events on MC and data under the corresponding selection.

Sideband	N_{MC}	N_{data}	N_{data}/N_{MC}
SB 0	$1.70^{+0.85}_{-0.55}$	3^{+3}_{-2}	$1.76^{+1.92}_{-1.11}$
SB 1	$0.0^{+1.8}_{-0.0}$	0^{+2}_{-0}	–
SB 2	$25.1^{+3.7}_{-2.6}$	24^{+6}_{-5}	$0.96^{+0.27}_{-0.22}$
SB 0 + SB 2	$26.8^{+3.7}_{-2.7}$	27^{+6}_{-5}	$1.01^{+0.27}_{-0.22}$

The full distribution of the $M_{recoil}(\pi^+\pi^-)$ variable is plotted in fig. 4.21, which shows the data/MC comparison for events lying outside the blinded regions. For each histogram bin, the difference between data and MC counts is comprised in the 2σ interval as can be seen by the pull plot.

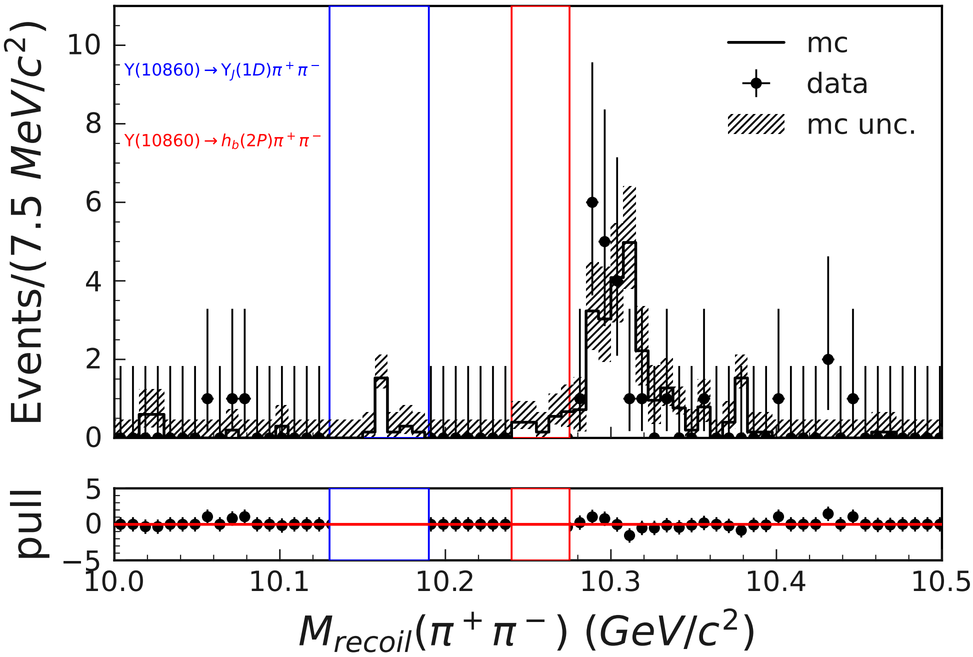

Figure 4.21: Data/MC comparison for background in sidebands of the di-pion recoil mass distribution. The two blinded regions are indicated by the corresponding box.

The MC and data events taken from sidebands SB0 and SB1 are superimposed to the true signal events, which belong to the signal region. The obtained distributions are shown in fig. 4.22a. It can be seen that the background is almost absent, due to both the analysis setup and the optimized selection.

In fig. 4.22b is shown the superposition of signal events and background events lying in the SB 2 sideband. Here, it can be noted that the SB 2 events bring to peaking background in the fit variable, as expected from the MC simulation.

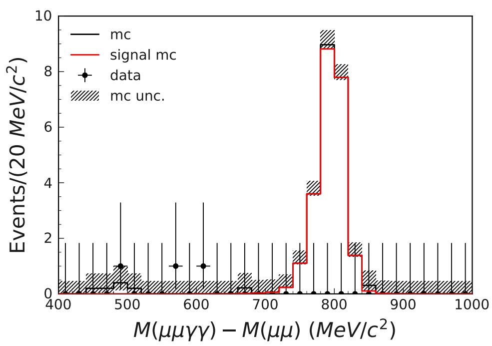

(a)

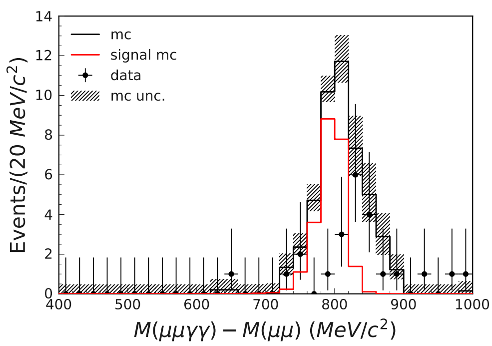

(b)

Figure 4.22: Distribution of the fit variable for signal MC events and data plus generic MC from sidebands SB0 and SB1 (a), compared with the same distribution in sideband SB2.

4.5.3 Summary of the systematic uncertainties

Other than the uncertainties related to event selection and background counts, several sources contribute to the systematics in the estimation of the upper limits for the branching fractions. One source is the measured integrated luminosity, whose uncertainty is entirely systematic and corresponds to 1.4% [75]. At the Belle experiment the luminosity is measured by reconstructing the $e^+e^- \to e^+e^-(\gamma)$ and $e^+e^- \to \gamma\gamma$ processes and measuring the corresponding visible cross section. The uncertainty arises from the variability of the collider parameters (beam energy, IP position) in different runs, the ECL trigger inefficiency, the selection criteria and residual background processes such as $e^+e^- \to \tau\tau$ [76].

The uncertainty on track finding efficiency for low momentum pions is measured from data/MC comparison for D^* decays and corresponds to 1.0% per single track [77].

For high momentum tracks the systematic uncertainty is 0.35% [78]. It is estimated by reconstructing $D^* \to \pi_{slow} D^0$, $D^0 \to \pi^+\pi^- K^0_S$, $K^0_S \to \pi^+\pi^-$ where one of the pions from K^0_S is ignored. Here, the track finding efficiency is identified with the rate of finding the unreconstructed track. This is obtained by imposing kinematic constraints on the masses of reconstructed D^*, D^0 and K^0_S. The overall systematic error due to track finding efficiency is 2.7% as a result of error propagation for two low-momentum and two high-momentum tracks.

The error propagation is done assuming that the tracks are correlated, so the uncertainties of each track are summed. The same criterion is applied to the two photons.

The error on photon detection efficiency is 2.0% [79], bringing to 4.0% for our case. Here, the systematic error is estimated by reconstructing radiative Bhabha events and evaluating the ratio between the number of detected and expected photons. The use of the radiative Bhabha process is motivated by the fact that the accuracy of the theoretical prediction for the cross section is very high, being it a QED process.

The uncertainty related to the use of lepton identification (LID) variables is 0.3% for each track [80]. This is estimated by data/MC comparison for reconstructed $J/\psi \to ll$, with $l = \mu^\pm$ and $l = e^\pm$. The overall uncertainty on LID is 0.6% for four tracks.

All the sources of systematic uncertainties are summarized in table 4.6 with their values. It can be seen that the dominant source of systematic uncertainty comes from the estimation of background counts, because of the low number of events surviving the selection.

4.6 Upper limit sensitivity

I use the Feldman-Cousins approach [81] to determine the average upper limit $u_{0.9}$ on the number of signal events, with 90% confidence level. In order to do so, I count the MC background events lying in the signal region after the whole selection and take into account the uncertainties estimated by data/MC comparison. The number of background events expected from MC is $n_{bkg} = 1.9$, which corresponds to $u_{0.9} = 3.86$ for a Poisson random variable. The residual background in the

Table 4.6: Summary of the systematic uncertainties.

Source	Relative uncertainty (%)
Selection efficiency	$^{+9}_{-7}$
Luminosity	1.4
Tracking	2.7
LID	1.2
Photon detection	4.0
Background counts	$^{+27}_{-22}$
Total	$^{\mathbf{+29}}_{\mathbf{-24}}$

signal region comes from $\Upsilon(10860) \to \chi_{b1,2}(1P)\pi^+\pi^-\pi^0$, $\chi_{bJ}(1P) \to \Upsilon(1S)\gamma$ and $\Upsilon(10860) \to \eta\Upsilon(2S)$, $\Upsilon(2S) \to \Upsilon(1S)\pi^+\pi^-$, $\eta \to \gamma\gamma$ transitions.

Assuming that [39]

$$\Gamma[h_b(2P) \to \chi_{b2}(1P)\gamma] : \Gamma[h_b(2P) \to \chi_{b1}(1P)\gamma] : \Gamma[h_b(2P) \to \chi_{b0}(1P)\gamma] = 25 : 20 : 7 \tag{4.15}$$

and including the systematic uncertainty, the expected upper limits for no observed signal are as follows:

- $\mathcal{B}[h_b(2P) \to \chi_{b2}(1P)\gamma] < 1.3 \times 10^{-3}$
- $\mathcal{B}[h_b(2P) \to \chi_{b1}(1P)\gamma] < 1.0 \times 10^{-3}$
- $\mathcal{B}[h_b(2P) \to \chi_{b0}(1P)\gamma] < 3.7 \times 10^{-4}$.

For each channel, the expected upper limit on the BF falls halfway between the RQM [22] and coupled-channel model [39] predictions. The reported upper limits correspond to the average upper limit that would be obtained after repeating the experiment many times, that is the experiment sensitivity. It is calculated by averaging the limits of the confidence intervals, with weights given by Poisson probability mass functions that correspond to different values of the background mean.

Chapter 5

Conclusion

Throughout this thesis I analyzed the data produced by the Belle experiment via e^+e^- collisions at center of mass energy $\sqrt{s} = 10.860\ GeV$. The search for the hindered M1 transitions $h_b(2P) \to \gamma\chi_{bJ}(1P)$ is based on the fully exclusive cascade $\Upsilon(10860) \to h_b(2P)\pi^+\pi^- \to \gamma\chi_{bJ}(1P)\pi^+\pi^- \to \gamma\gamma\Upsilon(1S)\pi^+\pi^- \to \gamma\gamma\mu^+\mu^-\pi^+\pi^-$. This choice implies that there is no missing energy in the event and the physics background is suppressed. Moreover, the signature of the cascade is very clear in different variables, such as the recoil mass of the monochromatic di-pion system ($M_{recoil}(\pi^+\pi^-)$) and the chosen fit variable $M(\mu\mu\gamma\gamma)-M(\mu\mu)$, which peak on the $h_b(2P)$ mass and on the mass difference $M(h_b(2P)) - M(\Upsilon(1S))$, respectively.

I studied the event selection on MC data after the generation of the signal MC and the collection of all the generic MC samples produced by Belle. The latter did not contain the $\Upsilon(10860) \to \eta\Upsilon(2S)$ and the $\Upsilon(10860) \to \pi^+\pi^-\pi^0\chi_{bJ}(1P)$ processes, which I simulated and added to the generic MC.

The physics processes leading to background that survive the selection have been identified thanks to the already produced MC and from data/MC comparison in the case of missing samples. Due to the fact that the event topology suffers the presence of peaking background, I have performed a blind analysis by hiding the real data lying in the $M_{recoil}(\pi^+\pi^-)$ region corresponding to $(-3\sigma, +2\sigma)$ with respect to the mean of the signal MC distribution. The unblinding of the signal region (box) is consequent to the interaction with a referee committee of the Belle experiment. After the box opening I will be able to infer the observed upper limit for the branching fractions: for now I obtained preliminary result based on MC simulations and the relative validation.

The selection efficiencies are estimated from MC matching and reported in table 4.2. The efficiency estimation has been cross-checked by using the control channel $\Upsilon(3S) \to \gamma\chi_{bJ}(2P) \to \gamma\gamma\Upsilon(2S) \to \gamma\gamma\pi^+\pi^-\Upsilon(1S) \to \gamma\gamma\pi^+\pi^-\mu^+\mu^-$, which is also used to estimate the systematic uncertainties consequent to the event selection. Finally, the selection has been validated on $M_{recoil}(\pi^+\pi^-)$ sideband regions by comparison of MC with real $\Upsilon(10860)$ data, also used to estimate the error on the background counts. The overall systematic uncertainty has been estimated as $syst. =^{+29\%}_{-24\%}$. The main contribution to the uncertainty comes from the estimation of the background counts because of the low number of events surviving the selection.

Preliminary results on the upper limits for the branching fractions of the $h_b(2P) \to \chi_{bJ}(1P)\gamma$ transitions have been obtained. The results on the upper limits are taken from the experimental sensitivity, as defined by the Feldman-Cousins method [81], and are of order $10^{-4} - 10^{-3}$. This is halfway between the predictions of the RQM [22] and coupled-channel [39] models: this means that the analysis I performed is able to discriminate between the two models.

Appendix A

Decay tables

Listing A.1: EvtGen decay table used for the generation of signal MC.

```
# Y(5S) -> Zb pi
# 1- -> 1+ 0-
# (L, S) = (0, 1)
Decay Upsilon(5S)
0.25 Zb(10650)+ pi-    HELAMP  1. 0.    1. 0.    1. 0.;
0.25 Zb(10650)- pi+    HELAMP  1. 0.    1. 0.    1. 0.;
0.25 Zb(10610)+ pi-    HELAMP  1. 0.    1. 0.    1. 0.;
0.25 Zb(10610)- pi+    HELAMP  1. 0.    1. 0.    1. 0.;
Enddecay

# Zb -> h_b pi
# 1+ -> 1+ 0-
# P-wave
# (L, S) = (1, 1)
Decay Zb(10650)+
1.00 h_b(2P) pi+       HELAMP  1. 0.    0. 0.    -1. 0.;
Enddecay
CDecay Zb(10650)-

# Zb partner
Decay Zb(10610)+
1.00 h_b(2P) pi+       HELAMP  1. 0.    0. 0.    -1. 0.;
Enddecay
CDecay Zb(10610)-

# h_b(2P) radiative decays
# Projections of invariant amplitudes taken from Guo2016
Decay h_b(2P)
0.25 gamma chi_b2      HELAMP  1.4142136 0.    1. 0.
   0. 0.    0. 0.    -1. 0.    -1.4142136 0.;
0.20 gamma chi_b1      HELAMP  1. 0.    1. 0.    1. 0.
      1. 0.;
0.07 gamma chi_b0      HELAMP  1. 0.    -1. 0.;
Enddecay
```

```
Decay chi_b2
1.000 gamma Upsilon    HELAMP  1. 0. 1.7320508 0.
   2.4494897 0. 2.4494897 0. 1.7320508 0. 1. 0.;
Enddecay

# V -> gamma V
Decay chi_b1
1.000 gamma Upsilon    HELAMP  1. 0. 1. 0. -1. 0. -1. 0.;
Enddecay

# S -> gamma V
# HELAMP: best values from BBR 2014,
# using B(Y2S->gamma chib)
Decay chi_b0
1.000 gamma Upsilon    HELAMP  1. 0. 1. 0.;
Enddecay

# Y(1S) -> mu+ mu-
Decay Upsilon
1.000 mu+ mu-  VLL;
Enddecay

End
```

Listing A.2: EvtGen decay table used for the generation of the control channels.

```
Decay Upsilon(3S)
0.131 gamma chi_b2(2P)     HELAMP 2.4494897 0. 1.7320508
   0. 1. 0.  1. 0. 1.7320508 0. 2.4494897 0.;
0.126 gamma chi_b1(2P)     HELAMP 1. 0. 1. 0. -1. 0. -1.
   0.;
0.059 gamma chi_b0(2P)     HELAMP 1. 0. 1. 0.;
Enddecay

Decay chi_b2(2P)
1.00000000 gamma Upsilon(2S)    HELAMP 1. 0. 1.7320508 0.
    2.4494897 0.     2.4494897 0. 1.7320508 0. 1. 0.;
Enddecay

Decay chi_b1(2P)
1.00000000 gamma Upsilon(2S)    HELAMP 1. 0. 1. 0. -1. 0.
    -1. 0.;
Enddecay

Decay chi_b0(2P)
1.00000000 gamma Upsilon(2S)    HELAMP 1. 0. 1. 0.;
Enddecay

Decay Upsilon(2S)
1.00000000 Upsilon pi+ pi-      VVPIPI;
Enddecay

Decay Upsilon
1.00000000 mu+ mu-              VLL;
Enddecay

End
```

A.1 FoM optimization

This section contains the plots of the FoM optimization for each optimized selection.

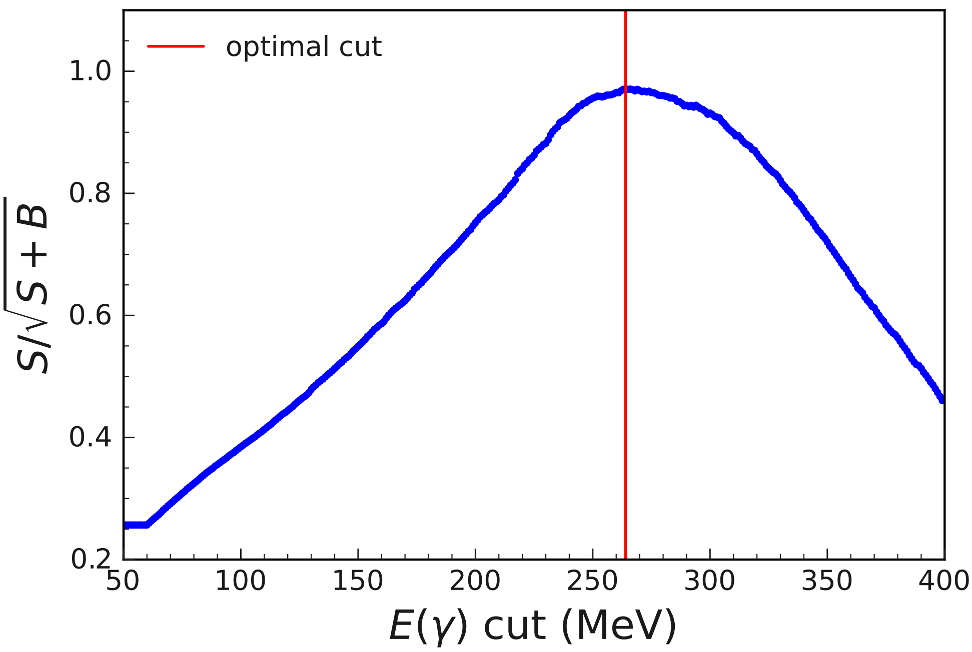

Figure A.1: Optimization of the cut on the photon energy in the laboratory reference frame.

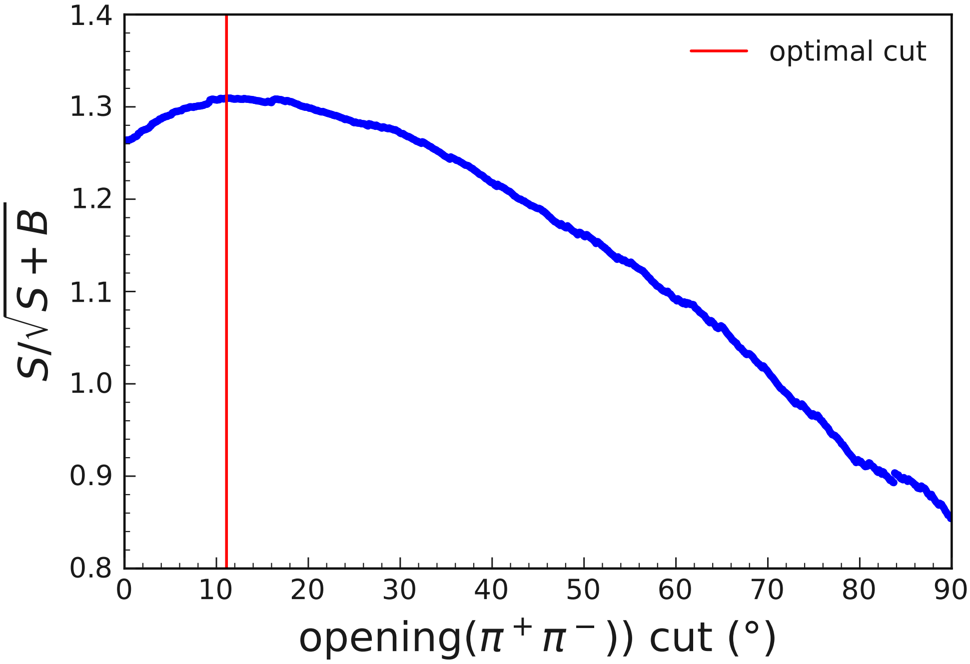

Figure A.2: Optimization of the cut on the di-pion opening angle in the laboratory reference frame.

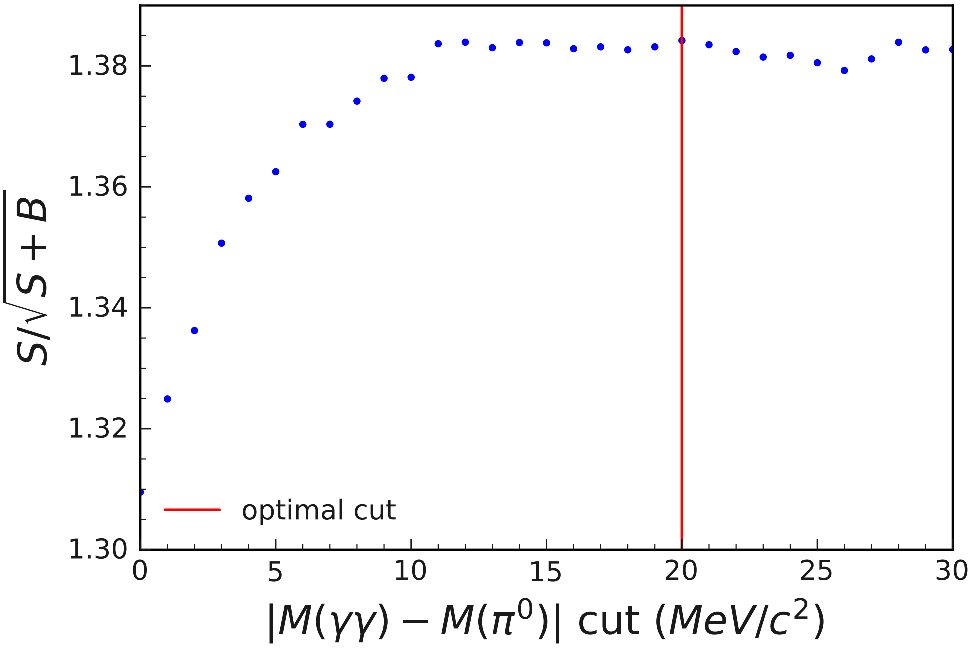

Figure A.3: Optimization of the π^0 veto.

A.2 Determination of the number of $\Upsilon(3S)$

To measure the number of $e^+e^- \to \Upsilon(3S)$ reactions produced in experiment 49, I reconstruct

$$\Upsilon(3S) \to \pi^+\pi^-\Upsilon(1S) \to \pi^+\pi^-\mu^+\mu^- \tag{A.1}$$

on data and MC. The event selection corresponds to that described in section 4.4.1, except that here no photon is reconstructed. Additional requirements are $10.15 < M(\mu\mu\pi\pi) < 10.5\ GeV/c^2$, $e_{ID} < 0.4$ for pions and $\mu_{ID} > 0.8$ for muons. I use $M(\mu\mu\pi\pi) - M(\mu\mu)$ as the fit variable in order to determine the signal yield. The number of $\Upsilon(3S)$ resonances produced in e^+e^- annihilations is computed as

$$N^{prod}_{\Upsilon(3S)} = \frac{N^{fit}_{\Upsilon(3S)}}{\epsilon_{\mu\mu\pi\pi}\mathcal{B}}, \tag{A.2}$$

where $N^{fit}_{\Upsilon(3S)}$ is the yield determined from the fit, $\epsilon_{\mu\mu\pi\pi}$ is the reconstruction efficiency, and $\mathcal{B}$ is the product branching ratio for the process A.1. The efficiency is estimated from MC, resulting in $\epsilon_{\mu\mu\pi\pi} = 40.7 \pm 0.2\%$. The product branching ratio is [10]

$$\mathcal{B} = \mathcal{B}[\Upsilon(3S) \to \pi^+\pi^-\Upsilon(1S)] \times \mathcal{B}[\Upsilon(1S) \to \mu^+\mu^-] = (1.08 \pm 0.03) \times 10^{-3}. \tag{A.3}$$

I fit the distribution with a Double-sided Crystal Ball (DSCB) function plus linear background, using an extended binned maximum likelihood cost function. The fit yields $N^{fit}_{\Upsilon(3S)} = 4985 \pm 82$. It is shown in fig. A.4. Here, the pull is defined similarly to eq. 4.14, but the difference is the residual between the fit value at bin center and bin counts, normalized by its uncertainty.

The systematics are due to uncertainties on tracking efficiency (1.5%), particle identification (0.6%) and the product branching fraction reported in (A.3). Considering the statistical error as due to the efficiency estimation, which assumes a binomial distribution, and the extended fit result, we have

$$N^{prod}_{\Upsilon(3S)} = (11.4 \pm 0.2 \pm 0.4) \times 10^6 \tag{A.4}$$

where the first error is statistical and the second systematic. This value is used to normalize the number of events generated for the processes (4.13).

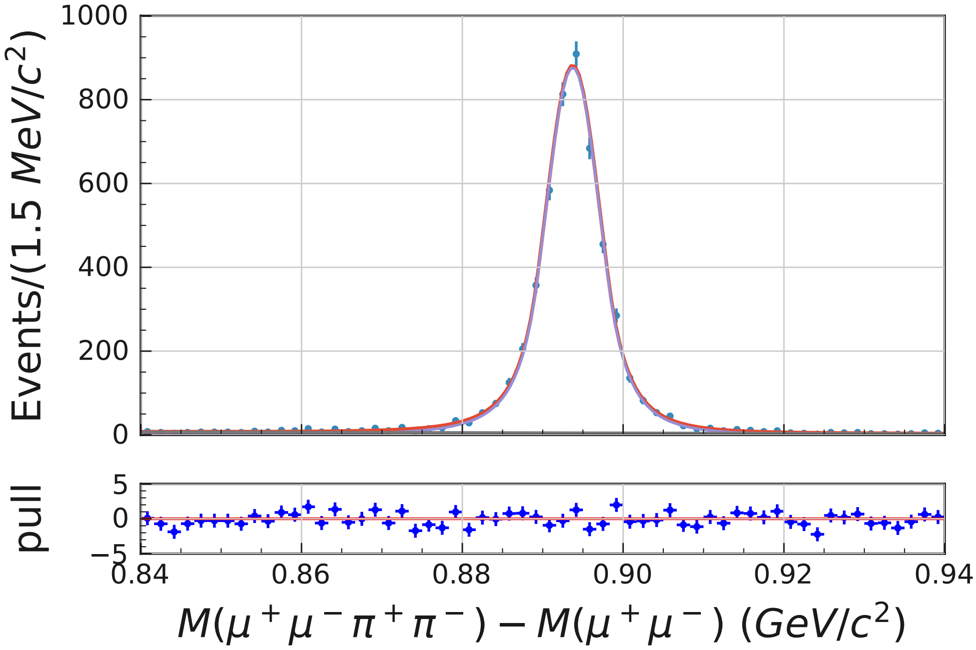

Figure A.4: Fit to the $M(\mu\mu\pi\pi) - M(\mu\mu)$ distribution for reconstructed $\Upsilon(3S) \to \pi^+\pi^-\Upsilon(1S) \to \pi^+\pi^-\mu^+\mu^-$ events.

A.3 Kinematic fitting

The kinematic fit is an optimization procedure that finds the best estimate for a set of parameters with the application of constraints, which serve to supply physical information. The goal is to improve the knowledge on the measured kinematic quantities while defining a test statistic useful for the event selection. A typical constraint is the conservation of the four-momentum, while the parameters can be any kinematic variable, such as the components of momentum vectors.

Consider a set of n measured values α_m with covariance matrix V. Denoting with α_0 the array of best values, the imposition of a set of constraints η is represented by k equations $f_i(\alpha_0, \eta) = 0$. The optimization with constraints is accomplished by using the method of Lagrange multipliers: the quantity being minimized is defined as

$$\chi^2 = (\alpha_m - \alpha_0)^T V^{-1}(\alpha_m - \alpha_0) + 2\lambda f(\alpha_0, \eta) \tag{A.5}$$

where λ is the array of Lagrange multipliers. From eq. (A.5) it can be seen that the covariance matrix is used to weight the differences between the measured parameters and their best estimates. Thanks to the Lagrange multiplier method, the minimization of a function of n variable with k constraints is transformed to the minimization of a function of $n + k$ variables. The minimization procedure is initialized by linearizing the constraint function f around a convenient value α_p. The optimum value of the χ^2 can be used as a test statistics in order to evaluate the goodness of the fit. In addition, the p-value can be used for the same purpose. The p-value is defined as the probability to observe a χ^2 equal or higher to that obtained after the minimization.

Bibliography

[1] S. W. Herb et al. "Observation of a Dimuon Resonance at 9.5 GeV in 400-GeV Proton-Nucleus Collisions". In: *Phys. Rev. Lett.* 39 (5 1977), pp. 252–255. DOI: 10.1103/PhysRevLett.39.252. URL: https://link.aps.org/doi/10.1103/PhysRevLett.39.252.

[2] Walter R. Innes et al. "Observation of Structure in the Υ Region". In: *Phys. Rev. Lett.* 39 (1977). [Erratum: Phys.Rev.Lett. 39, 1640 (1977)], pp. 1240–1242. DOI: 10.1103/PhysRevLett.39.1240.

[3] H. Albrecht et al. "Physics with ARGUS". In: *Phys. Rept.* 276 (1996), pp. 223–405. DOI: 10.1016/S0370-1573(96)00008-7.

[4] T. Skwarnicki. "Bottomonium studies via Upsilon(3S) decays. First observation of Upsilon(1D) states". In: *31st International Conference on High Energy Physics*. July 2002, pp. 698–702.

[5] Joerg Marks. "Bottomonium Results from BABAR and BELLE". In: *44th Rencontres de Moriond on QCD and High Energy Interactions*. June 2009, pp. 111–114. arXiv: 0906.0725 [hep-ex].

[6] M. Artuso et al. "Photon transitions in Upsilon(2S) and Upsilon(3S) decays". In: *Phys. Rev. Lett.* 94 (2005), p. 032001. DOI: 10.1103/PhysRevLett.94.032001. arXiv: hep-ex/0411068.

[7] Bernard Aubert et al. "Observation of Upsilon(4S) decays to pi+ pi- Upsilon(1S) and pi+ pi- Upsilon(2S)". In: *Phys. Rev. Lett.* 96 (2006), p. 232001. DOI: 10.1103/PhysRevLett.96.232001. arXiv: hep-ex/0604031.

[8] U. Tamponi et al. "First observation of the hadronic transition $\Upsilon(4S) \to \eta h_b(1P)$ and new measurement of the $h_b(1P)$ and $\eta_b(1S)$ parameters". In: *Phys. Rev. Lett.* 115.14 (2015), p. 142001. DOI: 10.1103/PhysRevLett.115.142001. arXiv: 1506.08914 [hep-ex].

[9] Bernard Aubert et al. "Observation of the bottomonium ground state in the decay $\upsilon_{3S} \to \gamma eta_b$". In: *Phys. Rev. Lett.* 101 (2008). [Erratum: Phys.Rev.Lett. 102, 029901 (2009)], p. 071801. DOI: 10.1103/PhysRevLett.101.071801. arXiv: 0807.1086 [hep-ex].

[10] P. A. Zyla et al. "Review of Particle Physics". In: *PTEP* 2020.8 (2020), p. 083C01. DOI: 10.1093/ptep/ptaa104.

[11] B. Povh et al. *Particles and nuclei: An Introduction to the physical concepts*. Graduate Texts in Physics. Springer, 1995. ISBN: 978-3-662-46320-8, 978-3-662-46321-5. DOI: 10.1007/3-540-36684-9.

[12] R. Keith Ellis, W. James Stirling, and B. R. Webber. *QCD and collider physics*. Vol. 8. Cambridge University Press, Feb. 2011. ISBN: 978-0-511-82328-2, 978-0-521-54589-1. DOI: 10.1017/CBO9780511628788.

[13] E. Leader and E. Predazzi. *An Introduction to gauge theories and modern particle physics. Vol. 2: CP violation, QCD and hard processes*. Vol. 4. Cambridge University Press, Mar. 1996. ISBN: 978-0-521-49951-4, 978-1-139-24099-4.

[14] Chris Quigg. *Gauge Theories of the Strong, Weak, and Electromagnetic Interactions: Second Edition*. USA: Princeton University Press, Sept. 2013. ISBN: 978-0-691-13548-9, 978-1-4008-4822-5.

[15] Matthias Neubert. "Renormalization Theory and Effective Field Theories". In: (Jan. 2019). Ed. by Sacha Davidson et al. DOI: 10.1093/oso/9780198855743.003.0001. arXiv: 1901.06573 [hep-ph].

[16] David J. Gross and Frank Wilczek. "Ultraviolet Behavior of Non-Abelian Gauge Theories". In: *Phys. Rev. Lett.* 30 (26 1973), pp. 1343–1346. DOI: 10.1103/PhysRevLett.30.1343. URL: https://link.aps.org/doi/10.1103/PhysRevLett.30.1343.

[17] E. Eichten et al. "The Spectrum of Charmonium". In: *Phys. Rev. Lett.* 34 (1975). [Erratum: Phys.Rev.Lett. 36, 1276 (1976)], pp. 369–372. DOI: 10.1103/PhysRevLett.34.369.

[18] E. Eichten et al. "The Interplay of Confinement and Decay in the Spectrum of Charmonium". In: *Phys. Rev. Lett.* 36 (1976), p. 500. DOI: 10.1103/PhysRevLett.36.500.

[19] E. Eichten et al. "Charmonium: Comparison with Experiment". In: *Phys. Rev. D* 21 (1980), p. 203. DOI: 10.1103/PhysRevD.21.203.

[20] E. Eichten et al. "Spectrum of Charmed Quark-Antiquark Bound States". In: *Phys. Rev. Lett.* 34 (6 1975), pp. 369–372. DOI: 10.1103/PhysRevLett.34.369. URL: https://link.aps.org/doi/10.1103/PhysRevLett.34.369.

[21] Jiri Mutu et al. "Meson spectra governed by the Fermi-Breit potential". In: *Chin. Phys. C* 33 (2009), pp. 170–176. DOI: 10.1088/1674-1137/33/3/002.

[22] S. Godfrey and Nathan Isgur. "Mesons in a Relativized Quark Model with Chromodynamics". In: *Phys. Rev. D* 32 (1985), pp. 189–231. DOI: 10.1103/PhysRevD.32.189.

[23] Stephen Godfrey and Kenneth Moats. "Bottomonium Mesons and Strategies for their Observation". In: *Phys. Rev. D* 92.5 (2015), p. 054034. DOI: 10.1103/PhysRevD.92.054034. arXiv: 1507.00024 [hep-ph].

[24] N. Brambilla et al. "Heavy quarkonium physics". In: (Dec. 2004). DOI: 10.5170/CERN-2005-005. arXiv: hep-ph/0412158.

[25] N. Brambilla et al. "Heavy Quarkonium: Progress, Puzzles, and Opportunities". In: *Eur. Phys. J. C* 71 (2011), p. 1534. DOI: 10.1140/epjc/s10052-010-1534-9. arXiv: 1010.5827 [hep-ph].

[26] Geoffrey T. Bodwin, Eric Braaten, and G. Peter Lepage. "Rigorous QCD analysis of inclusive annihilation and production of heavy quarkonium". In: *Phys. Rev. D* 51 (1995). [Erratum: Phys.Rev.D 55, 5853 (1997)], pp. 1125–1171. DOI: 10.1103/PhysRevD.55.5853. arXiv: hep-ph/9407339.

[27] A. Gray et al. "The Upsilon spectrum and m(b) from full lattice QCD". In: *Phys. Rev. D* 72 (2005), p. 094507. DOI: 10.1103/PhysRevD.72.094507. arXiv: hep-lat/0507013.

[28] Stefan Meinel. "The Bottomonium spectrum from lattice QCD with 2+1 flavors of domain wall fermions". In: *Phys. Rev. D* 79 (2009), p. 094501. DOI: 10.1103/PhysRevD.79.094501. arXiv: 0903.3224 [hep-lat].

[29] Antonio Vairo. "The Heavy quark potential in pNRQCD". In: *Nucl. Phys. B Proc. Suppl.* 86 (2000). Ed. by Stephan Narison, pp. 521–524. DOI: 10.1016/S0920-5632(00)00615-0. arXiv: hep-ph/9909440.

[30] Nora Brambilla, Yu Jia, and Antonio Vairo. "Model-independent study of magnetic dipole transitions in quarkonium". In: *Phys. Rev. D* 73 (5 2006), p. 054005. DOI: 10.1103/PhysRevD.73.054005. URL: https://link.aps.org/doi/10.1103/PhysRevD.73.054005.

[31] Yoshiaki Koma and Miho Koma. "Spin-dependent potentials from lattice QCD". In: *Nucl. Phys. B* 769 (2007), pp. 79–107. DOI: 10.1016/j.nuclphysb.2007.01.033. arXiv: hep-lat/0609078.

[32] Jia-Feng Liu and Gui-Jun Ding. "Bottomonium Spectrum with Coupled-Channel Effects". In: *Eur. Phys. J. C* 72 (2012), p. 1981. DOI: 10.1140/epjc/s10052-012-1981-6. arXiv: 1105.0855 [hep-ph].

[33] Paul Geiger and Eric S. Swanson. "Distinguishing among strong decay models". In: *Phys. Rev. D* 50 (1994), pp. 6855–6862. DOI: 10.1103/PhysRevD.50.6855. arXiv: hep-ph/9405238.

[34] Rajan Gupta. "Introduction to lattice QCD: Course". In: *Les Houches Summer School in Theoretical Physics, Session 68: Probing the Standard Model of Particle Interactions*. July 1997, pp. 83–219. arXiv: hep-lat/9807028.

[35] Christian P. Robert and George Casella. "Monte Carlo Statistical Methods". In: *Springer Texts in Statistics*. 2004.

[36] R. Mizuk et al. "Evidence for the $\eta_b(2S)$ and observation of $h_b(1P) \to \eta_b(1S)\gamma$ and $h_b(2P) \to \eta_b(1S)\gamma$". In: *Phys. Rev. Lett.* 109 (2012), p. 232002. DOI: 10.1103/PhysRevLett.109.232002. arXiv: 1205.6351 [hep-ex].

[37] Nora Brambilla, Piotr Pietrulewicz, and Antonio Vairo. "Model-independent Study of Electric Dipole Transitions in Quarkonium". In: *Phys. Rev. D* 85 (2012), p. 094005. DOI: 10.1103/PhysRevD.85.094005. arXiv: 1203.3020 [hep-ph].

[38] Estia Eichten et al. "Quarkonia and their transitions". In: *Rev. Mod. Phys.* 80 (2008), pp. 1161–1193. DOI: 10.1103/RevModPhys.80.1161. arXiv: hep-ph/0701208.

[39] Feng-Kun Guo, Ulf-G. Meißner, and Zhi Yang. "Hindered magnetic dipole transitions between P -wave bottomonia and coupled-channel effects". In: *Physics Letters B* 760 (2016), pp. 417–421.

[40] P. Colangelo, F. De Fazio, and T. N. Pham. "Nonfactorizable contributions in B decays to charmonium: The Case of B- —> K- h(c)". In: *Phys. Rev. D* 69 (2004), p. 054023. DOI: 10.1103/PhysRevD.69.054023. arXiv: hep-ph/0310084.

[41] K. F. Chen et al. “Observation of anomalous Upsilon(1S) pi+ pi- and Upsilon(2S) pi+ pi- production near the Upsilon(5S) resonance”. In: *Phys. Rev. Lett.* 100 (2008), p. 112001. DOI: 10.1103/PhysRevLett.100.112001. arXiv: 0710.2577 [hep-ex].

[42] I. Adachi et al. “First observation of the P-wave spin-singlet bottomonium states $h_b(1P)$ and $h_b(2P)$”. In: *Phys. Rev. Lett.* 108 (2012), p. 032001. DOI: 10.1103/PhysRevLett.108.032001. arXiv: 1103.3419 [hep-ex].

[43] Bernard Aubert et al. “Study of hadronic transitions between Upsilon states and observation of Upsilon(4S) —> eta Upsilon(1S) decay”. In: *Phys. Rev. D* 78 (2008), p. 112002. DOI: 10.1103/PhysRevD.78.112002. arXiv: 0807.2014 [hep-ex].

[44] J. P. Lees et al. “Study of $\Upsilon(3S,2S)->\eta\Upsilon(1S)$ and $\Upsilon(3S,2S)->\pi^+\pi^-\Upsilon(1S)$ hadronic trasitions”. In: *Phys. Rev. D* 84 (2011), p. 092003. DOI: 10.1103/PhysRevD.84.092003. arXiv: 1108.5874 [hep-ex].

[45] E. Guido et al. “Study of η and dipion transitions in $\Upsilon(4S)$ decays to lower bottomonia”. In: *Phys. Rev. D* 96.5 (2017), p. 052005. DOI: 10.1103/PhysRevD.96.052005. arXiv: 1707.04973 [hep-ex].

[46] Yu-Ping Kuang. “QCD multipole expansion and hadronic transitions in heavy quarkonium systems”. In: *Front. Phys. China* 1 (2006), pp. 19–37. DOI: 10.1007/s11467-005-0012-6. arXiv: hep-ph/0601044.

[47] A. Bondar et al. “Observation of two charged bottomonium-like resonances in Y(5S) decays”. In: *Phys. Rev. Lett.* 108 (2012), p. 122001. DOI: 10.1103/PhysRevLett.108.122001. arXiv: 1110.2251 [hep-ex].

[48] A. Garmash et al. “Amplitude analysis of $e^+e^- \to \Upsilon(nS)\pi^+\pi^-$ at $\sqrt{s} =$ 10.865~GeV”. In: *Phys. Rev. D* 91.7 (2015), p. 072003. DOI: 10.1103/PhysRevD.91.072003. arXiv: 1403.0992 [hep-ex].

[49] Tao Guo et al. “The Possible candidates of tetraquark : $Z_b(10610)$ and $Z_b(10650)$”. In: (June 2011). arXiv: 1106.2284 [hep-ph].

[50] Yubing Dong et al. “Decays of Zb(+) and Zb’(+) as Hadronic Molecules”. In: *J. Phys. G* 40 (2013), p. 015002. DOI: 10.1088/0954-3899/40/1/015002. arXiv: 1203.1894 [hep-ph].

[51] A. Garmash et al. “Observation of Zb(10610) and Zb(10650) Decaying to B Mesons”. In: *Phys. Rev. Lett.* 116.21 (2016), p. 212001. DOI: 10.1103/PhysRevLett.116.212001. arXiv: 1512.07419 [hep-ex].

[52] Cheng-Jian Xiao and Dian-Yong Chen. “Analysis of the hidden bottom decays of Zb(10610) and Zb(10650) via final state interaction”. In: *Phys. Rev. D* 96.1 (2017), p. 014035. DOI: 10.1103/PhysRevD.96.014035.

[53] A. J. Bevan et al. “The Physics of the B Factories”. In: *Eur. Phys. J. C* 74 (2014), p. 3026. DOI: 10.1140/epjc/s10052-014-3026-9. arXiv: 1406.6311 [hep-ex].

[54] A. Abashian et al. “The Belle Detector”. In: *Nucl. Instrum. Meth. A* 479 (2002), pp. 117–232. DOI: 10.1016/S0168-9002(01)02013-7.

[55] R. Abe et al. "BELLE/SVD2 status and performance". In: *Nuclear Instruments and Methods in Physics Research Section A: Accelerators, Spectrometers, Detectors and Associated Equipment* 535.1 (2004). Proceedings of the 10th International Vienna Conference on Instrumentation, pp. 379–383. ISSN: 0168-9002. DOI: `https://doi.org/10.1016/j.nima.2004.07.156`. URL: `https://www.sciencedirect.com/science/article/pii/S0168900204016924`.

[56] Glenn F. Knoll. *Radiation Detection and Measurement, 3rd ed.* 3rd edition. New York: John Wiley and Sons, 2000. ISBN: 978-0-471-07338-3, 978-0-471-07338-3.

[57] Claus Grupen and Boris Schwartz. *Particle detectors*. Cambridge, UK: Cambridge Univ. Pr., 2008.

[58] . [s.n.] Chicago, IL: [s.n.], 1998. URL: `https://cds.cern.ch/record/352671`.

[59] Moritz Gelb et al. "B2BII: Data Conversion from Belle to Belle II". In: *Comput. Softw. Big Sci.* 2.1 (2018), p. 9. DOI: `10.1007/s41781-018-0016-x`. arXiv: `1810.00019 [hep-ex]`.

[60] Anders Ryd et al. "EvtGen: A Monte Carlo Generator for B-Physics". In: (May 2005).

[61] Torbjorn Sjostrand. "PYTHIA 5.7 and JETSET 7.4: Physics and manual". In: (Feb. 1994). arXiv: `hep-ph/9508391`.

[62] Z. Was, P. Golonka, and G. Nanava. "PHOTOS Monte Carlo for precision simulation of QED in decays: History and properties of the project". In: *PoS* ACAT (2007), p. 071. DOI: `10.22323/1.050.0071`. arXiv: `0707.3044 [hep-ph]`.

[63] René Brun et al. "GEANT Detector Description and Simulation Tool". In: (Oct. 1994). DOI: `10.17181/CERN.MUHF.DMJ1`.

[64] C. Bozzi and S. Roiser. "The LHCb software and computing upgrade for Run 3: opportunities and challenges". In: *J. Phys. Conf. Ser.* 898.11 (2017). Ed. by Richard Mount and Craig Tull, p. 112002. DOI: `10.1088/1742-6596/898/11/112002`.

[65] Belle Tracking Group. *Charged Particle Tracking in Belle, Belle Note 327.* 2000.

[66] Jim Pivarski et al. *scikit-hep/uproot: 3.12.0.* Version 3.12.0. July 2020. DOI: `10.5281/zenodo.3952728`. URL: `https://doi.org/10.5281/zenodo.3952728`.

[67] Thomas Kluyver et al. "Jupyter Notebooks – a publishing format for reproducible computational workflows". In: *Positioning and Power in Academic Publishing: Players, Agents and Agendas*. Ed. by F. Loizides and B. Schmidt. IOS Press. 2016, pp. 87 –90.

[68] Jun John Sakurai and Jim Napolitano. *Modern Quantum Mechanics*. Quantum physics, quantum information and quantum computation. Cambridge University Press, Oct. 2020. ISBN: 978-0-8053-8291-4, 978-1-108-52742-2, 978-1-108-58728-0. DOI: `10.1017/9781108587280`.

[69] M. Jacob and G. C. Wick. "On the General Theory of Collisions for Particles with Spin". In: *Annals Phys.* 7 (1959), pp. 404–428. DOI: `10.1016/0003-4916(59)90051-X`.

[70] Fabian Goerke et al. "$Z_b(10610)$ and $Z_b'(10650)$ decays in a covariant quark model". In: *Phys. Rev. D* 96.5 (2017), p. 054028. DOI: `10.1103/PhysRevD.96.054028`. arXiv: `1707.00539 [hep-ph]`.

[71] Kirill Chilikin. *run_dependent_mc*. `https://stash.desy.de/users/chilikin/repos/run_dependent_mc/`. 2021.

[72] P. Krokovny. *Observation of $\Upsilon(10860) \to \Upsilon(1S, 2S)\eta$ decays, Belle Note 1230*. 2017.

[73] J. H. Yin et al. "Observation of $e^+e^- \to \pi^+\pi^-\pi^0\chi_{b1,2}(1P)$ and search for $e^+e^- \to \phi\chi_{b1,2}(1P)$ at $\sqrt{s}$ = 10.96—11.05 GeV". In: *Phys. Rev. D* 98.9 (2018), p. 091102. DOI: `10.1103/PhysRevD.98.091102`. arXiv: `1806.06203 [hep-ex]`.

[74] Beatrice List and Jocelyne List. "MarlinKinfit: An Object–Oriented Kinematic Fitting Package". In: 2009.

[75] Jolanta Brodzicka et al. "Physics Achievements from the Belle Experiment". In: *PTEP* 2012 (2012), p. 04D001. DOI: `10.1093/ptep/pts072`. arXiv: `1212.5342 [hep-ex]`.

[76] V. Zilich. *Offline luminosity measurements from the Belle detector, Belle Note 453*. 2001.

[77] Wolfgang Dungel. *Systematic investigation of the reconstruction efficiency of low momentum $\pi^\pm$ and π^0, Belle Note 1176*. 2011.

[78] B. Bhuyan. *High p_T Tracking Efficiency Using Partially Reconstructed D^* Decays, Belle Note 1165*. 2010.

[79] H. W. Kim et al. *Photon Detection Efficiency Using Radiative Bhabha Sample, Belle Note 499*. 2002.

[80] S. Choudhury et al. *LID systematic using $J/\psi \to ll$ sample, Belle Note 1553*. 2010.

[81] Gary J. Feldman and Robert D. Cousins. "Unified approach to the classical statistical analysis of small signals". In: *Phys. Rev. D* 57 (7 1998), pp. 3873–3889. DOI: `10.1103/PhysRevD.57.3873`. URL: `https://link.aps.org/doi/10.1103/PhysRevD.57.3873`.